The Near Infrared Luminosity Function of the Norma Cluster

R.E. Skelton

Department of Astronomy
University of Cape Town
South Africa

A dissertation submitted in partial fulfillment of the requirements for the degree M.Sc. in the Department of Astronomy, as part of the National Astrophysics and Space Science Programme
UNIVERSITY OF CAPE TOWN

February 2007

Abstract

In this thesis, a near infrared K_s-band photometric catalogue of galaxies in the Norma cluster is presented. The survey of the cluster covers an area of $\sim 0.8 h_{70}^{-2}$ Mpc^2, and is estimated to be complete to a magnitude of $M_{K_s} \lesssim -19$ mag; this extends into the dwarf regime, 6 magnitudes below $M^*_{K_s}$. The catalogue contains 390 objects, 235 of which are classified as likely or definite galaxies and 155 as candidate galaxies. The K_s-band luminosity function (LF) is constructed from the photometric sample, using a smaller spectroscopic survey to estimate the number of member galaxies at each magnitude. A Schechter function provides a reasonable fit to the data, with a characteristic magnitude of $M^*_{K_s} = -25.36 \pm 0.74$ mag and faint-end slope of $\alpha = -1.25 \pm 0.10$. There is a distinct dip in the LF at $M_{K_s} \sim -22$ mag. The shape of the LF is similar to those found in previous determinations of the cluster LF, in both optical and near infrared. The Schechter parameters obtained by flagging the dip point agree well with those of recent field LFs. This suggests that both the shape of the bright end and the faint end slope are relatively insensitive to environment.

Acknowledgements

I would like to express my sincere gratitude to my supervisors for this work, Professor Renèe Kraan-Korteweg and Dr Patrick Woudt. You have both been very supportive and helpful throughout and I really appreciate the time and effort you put into your suggestions and feedback. I have learnt so much from you. It was always a pleasure to work in and be a part of the Astronomy department at UCT because of the warmth of the people involved. I would especially like to thank Paul, my wonderful office-mate, for being willing to help whenever he could and being available for discussion, sharing of problems and ideas, and of course, getting my computer sorted out. I am very grateful to both him and Ewald, my technological gurus. I'd also like to thank Michelle and Bonita for their wisdom and guidance, having been here before, and their friendship. Then, to my family, my sisters and parents, who've supported me in every possible way throughout my life and been my solid foundation: thank you! Last but not least, I'd like to thank François, whose faith in me is unerring. You have kept me going, shared your strength and made me smile whenever it has been tough and I feel blessed to have you alongside me.

This work has been funded through the National Astrophysics and Space Science Programme (NASSP) and a National Research Foundation (NRF) Prestigious and Equity Master's scholarship.

This publication makes use of data products from the Two Micron All Sky Survey, which is a joint project of the University of Massachusetts and the Infrared Processing and Analysis Center/California Institute of Technology, funded by the National Aeronautics and Space Administration and the National Science Foundation.

Contents

List of Figures

Chapter 1

Introduction

This thesis examines the Norma cluster in the near infrared wavelength range. The Norma cluster is the nearest ($v = 4844$ km s^{-1}) rich, massive cluster of galaxies (Kraan-Korteweg et al. 1996; Woudt 1998), with properties comparable to the Coma cluster (Mazure et al. 1998). Despite its proximity and richness, it has remained relatively unexplored in comparison to its well known counterpart. The importance of the Norma cluster was only realized in the late 1990s (Kraan-Korteweg et al. 1996; Böhringer et al. 1996) because it is hidden behind a veil of dust and stars in the southern Milky Way.

A broad band of the sky is obscured in this way; at optical wavelengths, galaxies across about 20% of the extragalactic sky are hidden from view, though major inroads have been made to fill in this gap over the last few years (see for e.g. Kraan-Korteweg & Lahav 2000). The extinction due to dust in our Galaxy makes extragalactic objects fainter and smaller at low Galactic latitudes (Cameron 1990), with almost complete extinction on the Galactic equator: in the B-band, for example, extinction on the equator can be as high as 70 magnitudes, according to the Galactic reddening maps of Schlegel, Finkbeiner & Davis (1998). The increased density of stars presents an additional challenge to astronomers interested in uncovering the galaxies beyond. The difficulties involved in finding galaxies here and analysing their intrinsic properties earned the region the nickname "Zone of Avoidance" (ZOA).

Observations in the near infrared (NIR) wavelength range are useful for penetrating the ZOA, because the extinction due to Galactic dust is up to an order of magnitude smaller in the NIR than in the optical. The NIR has a number of other advantages. Star-forming regions are bright at optical wavelengths, making optical observations particularly sensitive to galaxies where star formation is taking place. In contrast, the NIR is much less affected by short bursts of star formation and therefore it is a better indicator of galaxy mass. The NIR is also sensitive to emission from massive, early-type galaxies, which are completely missed in the far infrared or HI radio surveys, for example. The NIR consequently provides a better indication than the optical of the mass content of clusters.

In this thesis, deep K_s-band images of the central 0.8 Mpc^2 of the Norma cluster are used to investigate the nature of the cluster. In particular, the K_s-band luminosity function (LF hereafter) for the cluster is determined. The LF is a probability distribution, describing the relative numbers of galaxies of different magnitudes within a particular environment. The LF is a fundamental tool for observational cosmology and the study of galaxy formation and evolution (Binggeli, Sandage & Tammann 1988). The Coma cluster has been used as the archetypal rich zero-redshift cluster in a number of LF studies, dating back to the 1980s (see for e.g. Thompson & Gregory 1980; Andreon, Cuillandre & Pelló 2000). The Norma cluster now provides an ideal opportunity to test and complement existing knowledge on local clusters, due to the recent development of techniques to deal with ZOA data (e.g. automated star-subtraction with routines such as KILLALL; Buta & McCall 1999) and infrared array detectors that can image large areas in the NIR. The NIR K_s-band LF determined for the Norma cluster in this thesis will be used as a comparitive tool to examine changes in cluster composition – both locally and with increasing redshift – and thus explore galaxy evolution in dense environments.

1.1 The Norma Cluster

The Norma cluster (ACO 3627; Abell, Corwin & Olowin 1989) is situated at (l, b, v) = (325°, -7°, 4844 km s^{-1}), where l is Galactic longitude, b is Galactic latitude and v is heliocentric velocity. It is classified as an irregular cluster of Bautz-Morgan Type I, with richness of Type 1 in the Abell catalogue. Rich clusters of Type 1 in the Abell catalogue are those with more than 50 galaxies within 2 magnitudes of the 3rd brightest galaxy in the area defined by the Abell radius. The Abell radius is defined as $R_A = \frac{1.'7}{z}$, where z is the redshift of the cluster.

An Aside on Redshifts: Lines in a spectrum shift away from the wavelength observed at rest in a laboratory, due to the motion of the observed object towards or away from the observer. In an expanding universe, galaxies move apart (Hubble 1929), resulting in a shift of their spectral features towards longer wavelengths. This phenomenon is known as redshift. The redshift of an object is given by

$$z = \frac{\lambda_o - \lambda_r}{\lambda_r} = \frac{\Delta\lambda}{\lambda_r}$$

where λ_r is the rest wavelength and λ_o is the observed wavelength. For small redshifts, z can be approximated by $\frac{v}{c}$ where v is the line-of-sight recession velocity in the heliocentric reference frame and c is the speed of light (299 792 km s^{-1}).

Woudt (1998) measured the redshifts of 219 galaxies within the Norma cluster. The velocity centroid of the main cluster was found to be 4844 ± 63 km s^{-1}, with a dispersion of 848 km s^{-1}. This velocity corresponds to a redshift of $z = 0.01615$. The Abell radius

corresponds to an angular distance of 1.75° at this redshift. Using the Hubble Law (Hubble 1929), $v = H_0 d$ with a Hubble constant[1] of 70 km s^{-1}Mpc^{-1}, the distance to the Norma cluster[2] is $69h_{70}^{-1}$ Mpc, placing it in distance group 1 in the Abell catalogue. At this distance, the Abell radius corresponds to a physical size of 2 h_{70}^{-1} Mpc. When the Abell catalogue was compiled, 59 galaxies satisfying the criteria given above had been identified within R_A. It was classed as richness type 1.

A deep optical search for galaxies within the southern ZOA was carried out using photographic plates from the SRC IIIaJ sky survey (Kraan-Korteweg 2000; Woudt 1998; Woudt & Kraan-Korteweg 2001). Six hundred and three galaxies with a major diameter larger than 0.′2 were found within the Abell radius of the Norma cluster. Velocities were obtained for 266 of these during a follow-up redshift survey which used the Parkes Telescope, the South African Astronomical Observatory (SAAO) 1.9-m telescope (Woudt, Kraan-Korteweg & Fairall 1999) and the European Southern Observatory (ESO) multi-object spectrograph (MEFOS) (Woudt et al. 2004). Of these, 219 were confirmed as cluster members (Woudt 1998). The velocity distribution of the cluster is approximately Gaussian. The distribution indicates that the Norma cluster has voids in front and behind it in redshift space and is imbedded in a larger 'Great Wall'-like structure (Kraan-Korteweg et al. 1994), known as the Norma Wall. This large-scale structure is strikingly similar to the Great Wall in which the Coma cluster is situated (Kraan-Korteweg et al. 2005; Radburn-Smith et al. 2006).

The dynamical mass of the cluster can be estimated from the velocity dispersion (Woudt 1998), using the virial theorem in the formalism of Sarazin (1986). The mass within a radius R is given by

$$M(< R) = \frac{9\sigma^2 R_c}{G}(\ln(x + (1+x^2)^{1/2}) - x(1+x^2)^{-1/2}) \qquad (1.1)$$

where σ is the velocity dispersion, R_c is the core radius (King 1962), $x = \frac{R}{R_c}$ and G is the gravitational constant (4.30 $\times 10^{-9}$ Mpc (km s^{-1})^2 $M_\odot^{-1}$). The core radius is the radius at which the density drops to half the central density. The Norma cluster has a central density of 800 galaxies per square degree; the core radius is then 10.′4 (Kraan-Korteweg et al. 1996) corresponding to $\sim 0.2h_{70}^{-1}$ Mpc at the distance of the Norma cluster. Using Equation 1.1, the mass within the Abell radius (2 h_{70}^{-1} Mpc) is found to be $1.3\times10^{15}h_{70}^{-1}M_\odot$, where $M_\odot$ is solar masses.

An independent assessment of the mass of the Norma cluster was determined from X-ray

[1]A Hubble constant of $H_0 = 70$ km s^{-1}Mpc^{-1} is used throughout this thesis. The uncertainty in this quantity is represented by the dimensionless parameter h_{70}, related to the usual definition of the Hubble parameter h by $h \equiv \frac{H_0}{100 \mathrm{kms}^{-1}\mathrm{Mpc}^{-1}} = 0.7h_{70}$.

[2]Note that in the Great Attractor (GA) region, distance determined from redshifts alone may not be the true distance, due to the peculiar motions of galaxies towards the GA. The Norma cluster is situated near the bottom of the potential well of the GA (Woudt 1998), thus we expect it to be at rest with respect to the GA, however this assumption should be confirmed by independent distance measurements.

observations. Rich clusters are strong emitters in X-ray, because of the high temperature of the intracluster gas ($\sim 10^8$ K). X-ray observations with the Röntgen Satellite (ROSAT) Position Sensitive Proportional Counter (PSPC) confirmed that the Norma cluster is a rich massive cluster, though it was not detected in previous X-ray surveys due to confusion with a nearby X-ray binary (Böhringer et al. 1996). The Norma cluster is the 6th brightest galaxy cluster in the ROSAT All Sky Survey, with a luminosity of 2.2×10^{44} ergs^{-1}. The mass of the cluster determined from X-ray observations is $0.6 - 3.1 \times 10^{15} h_{70}^{-1}$ M$_\odot$ (Böhringer et al. 1996), which agrees well with the dynamical mass estimate by Woudt (1998), described above.

There are a number of similarities between the Norma cluster and the Coma cluster. Woudt (1998) compared the clusters by simulating an increase in dust and decrease in redshift on Coma cluster data. Many of the properties of the two clusters were found to be comparable. Both clusters contain 2 central cD galaxies and have similar mass and richness. As mentioned above, each of the clusters is found within a 'Great Wall'-like structure. The NIR properties of the two clusters have yet to be compared, however. This is one of the goals of this thesis: the NIR LF of the Norma cluster will be compared to that of Coma in Section 3.2.3.

Further new data on the Norma cluster is currently being analysed. In addition to the NIR data described in Chapter 2, pointed K_s-band observations of elliptical galaxies in the Abell radius of the cluster were made using SOFI on the New Technology Telescope (NTT). The cluster has also been observed in the R_C-band, using the Wide Field Imager (WFI) on the ESO/MPG 2.2-m telescope. These data are being used for an optical and NIR Fundamental Plane analysis, to obtain an independent distance estimate for the cluster (Woudt et al. 2005).

1.2 Astronomy in the Zone of Avoidance

Historical Overview

Zone of Avoidance (ZOA) astronomy has become an important field of research within extragalactic astronomy, particularly over the last two decades. During this time, much progress has been made towards uncovering galaxies in the ZOA. Kraan-Korteweg & Lahav (2000) provide a recent overview of astronomy in the ZOA from its beginnings in the late 19th century to the end of the 20th century.

The ZOA was initially termed the "Zone of Few Nebulae". It was noticed by Proctor (1878) after considering the distribution of objects in Sir John Herschel's 1864 "General Catalogue of Nebulae". Structure in the distribution of nebulae was already noticed in Herschel's time, though it was not realised that a large fraction of the nebulae are external Galactic systems similar to our own. The distribution of nebulae from the updated "New General Catalogue" (NGC) (Dreyer 1888, 1895) made the existence of the "Zone of Few

Nebulae" more obvious, as shown by Charlier (1922), who mapped the NGC distribution. The nature of nebulae was still being debated until the 1920s, when Harlow Shapley and Heber Curtis held their famous "Great Debate".

No connection was made between the Milky Way and the region where few galaxies were observed, as the interstellar absorption within our galaxy was severely underestimated. In an early model of the Milky Way, Kapteyn's Universe (see for e.g. Paul 1986), Galactic distances were also underestimated because dust was not taken into account. When a more realistic model of the Milky Way was developed, including significant amounts of dust, the link became clear. The first definition of the Zone of Avoidance was given by Shapley (1961), as the region within "the isopleth of five galaxies per square degree from the Lick and Harvard surveys". In comparison, the mean density of galaxies found by Shane & Wirtanen (1967) was 54 galaxies per square degree in unobscured regions of the sky.

Almost a century after the publication of the NGC, a whole-sky catalogue complete for galaxies with diameters larger than 1.′3 (Hudson & Lynden-Bell 1991) was created. Data from the Uppsala General Catalogue UGC (Nilson 1973), ESO Uppsala Catalogue (Lauberts 1982) and Morphological Catalogue of Galaxies MCG (Vorontsov-Velyaminov & Archipova 1963-74) were combined, taking the differences in isophotal limit into account by adjusting the diameters of the galaxies. The distribution of galaxies in this whole-sky catalogue is shown in Fig. 1.1, an Aitoff equal-area projection in Galactic coordinates (Kraan-Korteweg, 2006, private communication). The optical ZOA extends from approximately -10° to 10° in Galactic latitude, and can be clearly identified along the Galactic equator ($|b| = 0°$) in this map as the region lacking optical galaxy data. The position of the Norma cluster is highlighted in Fig. 1.1.

Figure 1.1: An Aitoff equal-area projection in Galactic coordinates, showing the distribution of galaxies in the whole-sky catalogue formed by combining the Uppsala General Catalogue, ESO Uppsala Catalogue and Morphological Catalogue of Galaxies. The solid line marks the extinction contour of 1 magnitude in the B-band from the DIRBE/IRAS dust map (Schlegel et al. 1998). The contour gives a good indication of the extent of the optical ZOA. The position of the Norma Cluster (A3627) is shown. The area of the circle corresponds to the area within 3 times the Abell radius (Image courtesy of Kraan-Korteweg (private communication) based on the original in Kraan-Korteweg & Lahav 2000)

Large-Scale Structure and Dynamics

In order to understand the three dimensional distribution of galaxies, rather than the projected distribution, distance information is needed. Large CCD arrays and spectrographs with multi-object capabilities have greatly increased the number of known galaxy redshifts since the 1980s (e.g. Fairall 1998; Geller & Huchra 1989). Over- and under-densities were revealed in the distribution of galaxies as maps of the large-scale structure of the Universe became more complete. Galaxies were found to be distributed in filaments and walls, containing large voids with very few galaxies between the Galactic structures (Fairall 1998). Clusters of galaxies form at the intersections of extragalactic filaments, rather than being isolated systems. This came as a surprise to astronomers and cosmologists, who did not expect to find such order in the distribution (e.g. Geller & Huchra 1989; Fairall 1998). This development had huge implications for cosmology and theories on the formation of galaxies and large-scale structures.

In standard Big Bang cosmology, the Universe is assumed to be homogeneous and isotropic on large scales (see for e.g. Peacock 1999). However, any model of the Universe, or simulation of the evolution of the Universe, must support the formation of the observed large-scale structures. Tiny density perturbations in the primordial material created potential wells, attracting matter and creating overdensities thought to be the seeds of the structures we see around us. The Cosmic Microwave Background (CMB), remnant radiation from the Big Bang, was discovered and interpreted in the 1960s (Penzias & Wilson 1965; Dicke et al. 1965). It appeared to be completely smooth until temperature perturbations of the order of 10^{-5} were observed in the 1990s (Smoot et al. 1992), lending support to this idea. The angular size of the CMB perturbations relates to the size of structures today. If the largest structures extend for hundreds of megaparsecs across the Galactic plane, regions that are too far apart, relative to the scale of the CMB perturbations, are causally connected. This would pose a problem for the standard cosmological viewpoint. The distribution of large-scale structures is bisected by the Galactic plane, thus interpolations have to be made to infer how structures on either side are linked together. As more galaxies are uncovered in the ZOA, these interpolations can be confirmed or rejected.

A more complete knowledge of the distribution of galaxies within the ZOA is necessary in order to understand the dynamics of the local Universe. The CMB observations show a large angular scale dipole distribution, suggesting that the Local Group of galaxies is moving with a velocity of approximately 600 km s^{-1} towards (l,b) = (276°, 30°) (Kogut et al. 1993). This motion is supposedly caused by the uneven distribution of matter in the Universe, which creates a gravitational flow field. The motion of our local group is dependent on the all-sky distribution of matter, including the mass hidden within the ZOA. The resulting motion is complicated, influenced strongly by the Virgo cluster (Aaronson, Huchra & Mould 1982), with other contributions from a cluster in the Puppis region

(Kraan-Korteweg & Huchtmeier 1992; Lahav et al. 1993) and a region in the opposite direction to the Galactic centre (Faber & Burstein 1988; Lu & Freudling 1995).

A number of methods can be used to infer the galaxy distribution within the ZOA. Reconstructions of the gravitational potential field across the Galactic plane, such as POTENT (Bertschinger & Dekel 1989; Dekel 1994), use the observed velocities of a large sample of galaxies to infer the underlying density field. The results suggest that there is a large-scale flow towards an overdensity termed the "Great Attractor" (GA) centred at (l,b,v) = (320°, 0°, 4500 km s^{-1}; Kolatt, Dekel & Lahav 1995). The GA is a 40°× 40° region hidden directly behind the Milky Way. There has been much debate about the nature and existence of the GA (e.g. Dressler & Faber 1990; Mathewson, Ford & Buchhorn 1992), because the strongest evidence for such an overdensity comes from theoretical reconstructions of the density field. An alternative view suggests that the motion is caused by an overdensity at higher redshift, known as the Shapley Concentration (Scaramella et al. 1989).

Observations have shown that the galaxy density in this so-called GA region is higher than average, peaking at the Norma cluster (Woudt & Kraan-Korteweg 2000). The Norma cluster, only 9° from the predicted centre of the GA, is thus far the most likely candidate for its centre, although it is not impossible that further clusters remain hidden at lower Galactic latitudes (see for e.g. Woudt & Kraan-Korteweg 2000)

Recent searches for low latitude clusters have included NIR surveys of the X-ray luminous cluster CIZA J1324.7-5736 (Nagayama et al. 2006) and the region around the giant radio-bright elliptical galaxy PKS 1343-601, 10° from the predicted core of the GA (Nagayama et al. 2004; Schröder et al. 2006), as well as a systematic X-ray search for Clusters in the Zone of Avoidance (CIZA; Ebeling, Mullis & Tully 2002). Deep NIR observations suggest that an overdensity of galaxies found around PKS 1343-60 is a group or poor cluster, rather than a rich cluster, since it is poorer than the Norma, Pavo and Centaurus clusters (Nagayama et al. 2004). This conclusion is supported by X-ray observations with the ASCA X-ray telescope, which detected only diffuse emission from PKS 1343-601 rather than the strong X-ray signature of a rich cluster (Tashiro et al. 1998).

Current Status of ZOA Observations

The degree and extent of the Milky Way's obstruction of the extragalactic sky depends on the wavelength of observation. The size of the ZOA thus differs in each wavelength band. A multi-wavelength approach has been successfully employed to uncover galaxies within $|b| \lesssim 10°$, to take advantage of the complementary information available from different bands.

Traditionally, the most extensive studies of the sky have been made with optical telescopes. In the ZOA, however, dust affects optical light to a greater extent than longer wavelength radiation, limiting the effectiveness of optical observations. Deep optical searches

(Woudt 1998; Kraan-Korteweg & Lahav 2000 and references therein) have covered the whole ZOA systematically, reducing the optical ZOA to the region delimited by an extinction in the B-band (A_B) of 3 magnitudes. Galaxies have been found in the optical for extinction levels of $A_B \lesssim 5^{\rm m}$. Optical surveys remain the most effective way of identifying galaxies at intermediate latitudes ($|b| \gtrsim 5°$) where the extinction is moderate ($A_B \lesssim 3^{\rm m}$) (Schröder, Kraan-Korteweg & Mamon 2000).

Radio and far infrared (FIR) wavelengths are unaffected by dust, but provide different views on the Universe. Galaxies containing large amounts of gas can be observed in the radio regime using the 21cm emission from the hyperfine splitting of the ground state in neutral hydrogen (HI). Radio observations have the advantage that distance information is available from the redshifted HI emission line. However, gas-poor galaxies and distant spiral galaxies cannot be observed using radio. The Multibeam (MB) ZOA survey used the 64m Parkes radio dish to systematically explore the southern ZOA ($|b| \lesssim 5°$), uncovering many previously undetected sources in regions where galaxies cannot be observed optically (Henning et al. 2000).

In the FIR, the Infrared Astronomical Satellite (IRAS) mapped the galaxy distribution, surveying 96% of the sky at 12, 25, 60 and 100μm (IRAS Point Source Catalogue, PSC; Joint *IRAS* Science Working Group 1988). Spiral and star-burst galaxies emit strongly at these wavelengths, but ellipticals and dwarf galaxies are not observed. Follow-up redshift surveys allowed for the 3 dimensional mapping of IRAS sources, through which a number of filamentary structures were discovered (The PSCz catalogue; Saunders et al. 2000a). Near the Galactic plane, FIR sources within the Milky Way are difficult to distinguish from external galaxies. Recently, the "Behind The Plane" (BTP) project (Saunders et al. 2000b) used K' images to confirm the nature of IRAS PSC sources in the ZOA. The addition of the BTP galaxies to the PSCz catalogue improves the mapping of large-scale structure across the plane of the galaxy. Overdensities such as the Norma cluster are now clearly visible in that distribution as well.

The slightly longer wavelengths of the NIR (0.75 – 5μm) can penetrate the dusty Milky Way to a greater extent than the optical. The extinction of background light due to dust is reduced by up to a factor of 10 (see Section 1.3). The number counts of detectable galaxies are predicted to decrease more slowly in the NIR than in the optical, with the numbers becoming higher than optical at extinctions of $A_B \gtrsim 2^{\rm m}$, even with shallower surveys (Schröder, Kraan-Korteweg & Mamon 2000), though this depends strongly on the completeness limit and resolution of the survey. The NIR has the advantage of high resolution and sensitivity to both spiral and elliptical galaxies, compared to longer wavelength regimes where instruments have limited resolution and are sensitive to nearby late-type galaxies. There is less contamination from galactic sources compared to the FIR. The NIR ZOA has been substantially reduced with two recent NIR all-sky surveys: the 2 Micron All Sky Survey (2MASS) (Jarrett et al. 2000a; Skrutskie et al. 2006), and the DEep Near

Infrared Southern Sky Survey (DENIS) (Epchtein 1997; Epchtein et al. 1997).

The NIR photometry of the Norma cluster in this thesis will be compared to 2MASS photometry, since the same filters are used in both surveys. 2MASS imaged the whole sky in the J ($\lambda = 1.25$ μm), $H(\lambda = 1.65$ μm) and K_s ($\lambda = 2.17$ μm) passbands between 1997 and 2001. The completeness limits of the survey for extended sources (10σ) are $J = 14.^{\rm m}7$, $H = 13.^{\rm m}9$ and $K_s = 13.^{\rm m}1$, while the spatial resolution is $2''$ (Jarrett et al. 2000a). The 2MASS distribution of extended sources extends well into the optical ZOA: galaxies down to $K_s = 13^{\rm m}$ for $|b| \gtrsim 5°$ and $K_s = 12.^{\rm m}1$ for $|b| \sim 2° - 3°$ can be identified (Jarrett et al. 2000b), though the completeness limits decrease by approximately half a magnitude at low Galactic latitudes (Jarrett 2004). The NIR ZOA seen in the 2MASS all-sky distribution stems largely from stellar crowding and the resulting source confusion. The Galactic centre, with the highest density of stars, is most affected by this. Star crowding can be dealt with by fitting a point spread function to subtract stellar light from crowded fields (see Section 2.3). However, given the low spatial resolution and limited automation of the technique, this is difficult in large automated surveys such as 2MASS, and the completeness of 2MASS is already severely affected in the surroundings of the Norma cluster.

1.3 Galactic Extinction

Dust in the interstellar material scatters and absorbs light from stars within the Galaxy and galaxies beyond. The effect of dust on light from background objects is described by the term "extinction" (Glass 1999). Extinction in the ZOA is particularly severe due to the abundance of dust in the Milky Way. On the Galactic equator extinction in the B-band can be as high as 70 magnitudes, according to the dust maps of Schlegel, Finkbeiner & Davis (1998).

Extinction is wavelength dependent, being most severe at short wavelengths. In the NIR the effect is diminished in comparison to the optical, but not negligible. Both the diameters and magnitudes of extragalactic objects are reduced. Objects affected by extinction are observed as redder than unaffected objects because of the preferential absorption of shorter wavelengths.

Mie Scattering Theory (van der Hulst 1957) is used to describe scattering in the ultraviolet (UV) and optical regimes where the sizes of dust particles are larger or of the same order of magnitude as the wavelength. When the dust particles are generally smaller than wavelength, such as in the FIR regime, Rayleigh Scattering Theory is used to describe the process. The size of dust particles is dependent on environment. Regions of high density are thought to have larger dust grains (Cardelli, Clayton & Mathis 1989). Extinction varies with line-of-sight due to the different densities of regions across the sky. To characterise the shift in colour or change in magnitude due to extinction, as observed

at a given wavelength, a reddening law is used.

An average extinction law in the NIR, optical and UV was derived by Cardelli, Clayton & Mathis (1989). The absolute extinction at a particular wavelength $A(\lambda)$, normalised to the extinction in the visual $A(V)$, is dependent on the parameter R_V. $A(\lambda)$ and $A(V)$ are given in magnitudes. R_V is the ratio of total to selective extinction, given by

$$R_V = \frac{A(V)}{E(B-V)}.$$

R_V is an indicator of environment and its value depends on the line-of-sight. For diffuse interstellar medium, $R_V \simeq 3.1$, though it can be as high as 5 in regions of recent star formation (Glass 1999). The selective extinction $E(B-V)$ is also known as the colour excess. The choice of normalisation of the extinction to $A(V)$ is made for historical consistency and because of the abundance of observational data in that wavelength band (Cardelli, Clayton & Mathis 1989).

For wavelengths longer than 0.9 μm, extinction is only weakly dependent on R_V. The shape of the extinction curve is the same for different lines of sight. The mean extinction law, given by Equation 1.2, where $x = 1/\lambda$, is linear in R_V^{-1} (Cardelli, Clayton & Mathis 1989).

$$\langle A(\lambda)/A(V)\rangle = a(x) + b(x)/R_V \tag{1.2}$$

For $0.3\mu\text{m}^{-1} \leq x \leq 1.1\mu\text{m}^{-1}$ ($0.9\mu\text{m} \leq \lambda \leq 3.3\mu\text{m}$):

$$a(x) = 0.574x^{1.61} \tag{1.3}$$

$$b(x) = -0.527x^{1.61} \tag{1.4}$$

The dust maps of Schlegel, Finkbeiner & Davis (1998) are widely used to determine Galactic extinction. A full-sky 100 μm map was created by combining the results of the Diffuse Infrared Background Experiment (DIRBE) on the COBE satellite with Infrared Astronomy Satellite (IRAS) Sky Survey Atlas (ISSA) data. A map of dust column density was created and calibrated to give Galactic reddening using the relation between $B-V$ colour and the absorption line index Mg_2 of elliptical galaxies. The extinction law of Cardelli, Clayton & Mathis (1989), for example, can then be used to transform the reddening estimate to extinction in a particular wavelength band. Schlegel, Finkbeiner & Davis (1998) warn that at low Galactic latitudes ($|b| \lesssim 5°$) the maps are not calibrated and contaminating sources have not been removed, however this does not greatly affect the region under consideration in this work.

The reddening maps of Burstein & Heiles (1982) (BH), based on the column densities of neutral hydrogen, were used to estimate Galactic extinction for many years prior to the publication of the DIRBE/IRAS infrared maps. In the ZOA, both methods tend to predict values of reddening that are too high (Burstein 2005). In regions of high extinction, the variation in reddening can be large even on small angular scales. The

resolution of the map used to estimate extinction limits the level of accuracy that can be obtained. The reddening value obtained over a particular pixel may be higher than the actual reddening for smaller regions within that line of sight. There is a bias towards observing galaxies in the regions of lowest extinction thus the reddening for these galaxies is over estimated by taking the total pixel value. For the BH maps, this effect becomes significant for $E(B-V) \geq 0.15$ mag. For the DIRBE/IRAS maps, it becomes significant for $E(B-V) \geq 0.25$ mag (Burstein 2003). Various other methods have been explored to estimate extinction at low latitudes (see for e.g. Nagayama et al. 2004, Schröder et al. 2005 and Nagayama et al. 2006). These and other authors (e.g. Dutra et al. 2003, Choloniewski & Valentijn 2003, Arce & Goodman 1999) find that the DIRBE/IRAS dust maps overestimate extinction at low Galactic latitudes by 13 – 33%.

In the central 0.8 Mpc^2 of the Norma cluster, the colour excess varies from 0.19 mag to 0.27 mag, according to the DIRBE/IRAS dust maps (Schlegel, Finkbeiner & Davis 1998). In this range, the DIRBE/IRAS maps are expected to more accurate than the BH maps. The over-estimation of reddening described above begins to be important at the upper end of this range, even for the DIRBE/IRAS maps. Woudt et al. (2005) find a mean colour excess for the Norma cluster of $E(B-V) = 0.22 \pm 0.03$ mag, determined using the near infrared colours of 16 galaxies situated within 1/3 of the Abell radius from the cluster centre. This compares well with the mean value of 0.207 ± 0.003 mag derived from the DIRBE/IRAS maps, a difference of less than 0.01 mag in A_{K_s}. The colour excess derived from the DIRBE/IRAS dust maps will thus be used to correct for Galactic extinction in this thesis (see Section 3.1.2).

1.4 Review of Luminosity Functions

The Luminosity Function (LF) is a quantitative description of the distribution of galaxies with luminosity in a particular environment. The LF is determined in different ways for galaxies within a cluster and for galaxies not belonging to a cluster, known as field galaxies. The LF of galaxies is a useful tool for studies of galaxy formation and evolution and fundamental for observational cosmology (Binggeli, Sandage & Tammann 1988). The LF is used as a weight when determining other properties of a sample of galaxies, such as the colour distribution (Andreon & Pelló 2000) and is used to determine selection effects in flux-limited samples. The local field LF is used to estimate the number of galaxies found at faint magnitudes. Both the local field LF and those of nearby clusters are used for comparison with higher redshift samples to study the evolution of galaxies. A comparison of field and cluster LFs yields information on the formation of clusters and dependence of galaxy properties on environment. Semi-analytic models of hierarchical galaxy formation can be used to predict the LF (see for e.g. Kauffmann et al. 1999, Somerville & Primack 1999, Cole et al. 2001). Comparison of the resulting LFs with those

determined observationally provide useful tests of the models and aid our understanding of galaxy formation. A comprehensive review of LFs, including examples of the use of the LF in cosmology, is given by Binggeli, Sandage & Tammann (1988).

Historical Determinations of the LF

The general LF $\Phi(M)$ is a probability distribution over absolute magnitude (M) (Binggeli, Sandage & Tammann 1988). The form of the optical general LF was first argued to be Gaussian by Hubble in the 1930s (1936a, 1936b, 1936c). Zwicky (1942, 1957, 1964) contradicted this claim by proposing an exponentially rising faint end to account for dwarf galaxies that were not included in Hubble's sample. The differences were resolved by considering the general LF to be composed of type-specific LFs $\Phi_T(M)$, where T represents the morphological type of the galaxies. Holmberg (1958, 1969) was able to probe faint enough magnitude limits to show that the LF of spirals in the field has a maximum, whereafter it decreases towards zero. Studies of the type-dependent LF rely on high enough resolution to distinguish between galaxy types, as well as sufficient depth to probe the faint end of the distribution. Such a study was made by Sandage, Binggeli & Tammann (1985) for the Virgo cluster, Thompson & Gregory (1980) for the Coma cluster and Ferguson & Sandage (1988) for the Fornax cluster. More recently, the type-specific LFs for the Centaurus cluster were determined and compared to those of Fornax and Virgo (Jerjen & Tammann 1997). A similar breakdown of the field LF into types was made using the Revised Shapley-Ames Catalogue (RSA) (Tammann, Sandage & Yahil 1980) and "10-Mpc Sample" (Kraan-Korteweg & Tammann 1979), though small number counts make this less reliable than that of Virgo (see Binggeli, Sandage & Tammann 1988 and references therein for details).

These studies suggest that ellipticals, lenticulars and spirals all have a bell-shaped LF, though the shapes and luminosities are slightly different for each galaxy type, as can be seen in Fig. 1.2. Ellipticals are slanted towards the faint end, dropping off quickly, while the curve for lenticulars slants in the opposite direction and is steeper than the elliptical curve at the bright end in both the field and cluster studies. The similarities of the E, S0 and spiral bright ends led to the notion of a "universal" total LF, independent of type. Dwarf ellipticals (dEs) form a separate class to regular ellipticals. The dE LF rises exponentially towards the faint end, with a steeper increase for clusters compared to the field.

The Schechter Function

The total LF is the sum of the type-dependent LFs. A single analytical function should not be expected to model the total LF sufficiently – according to Binggeli, Sandage & Tammann (1988) this would be like "covering a wealth of details with a thick blanket.

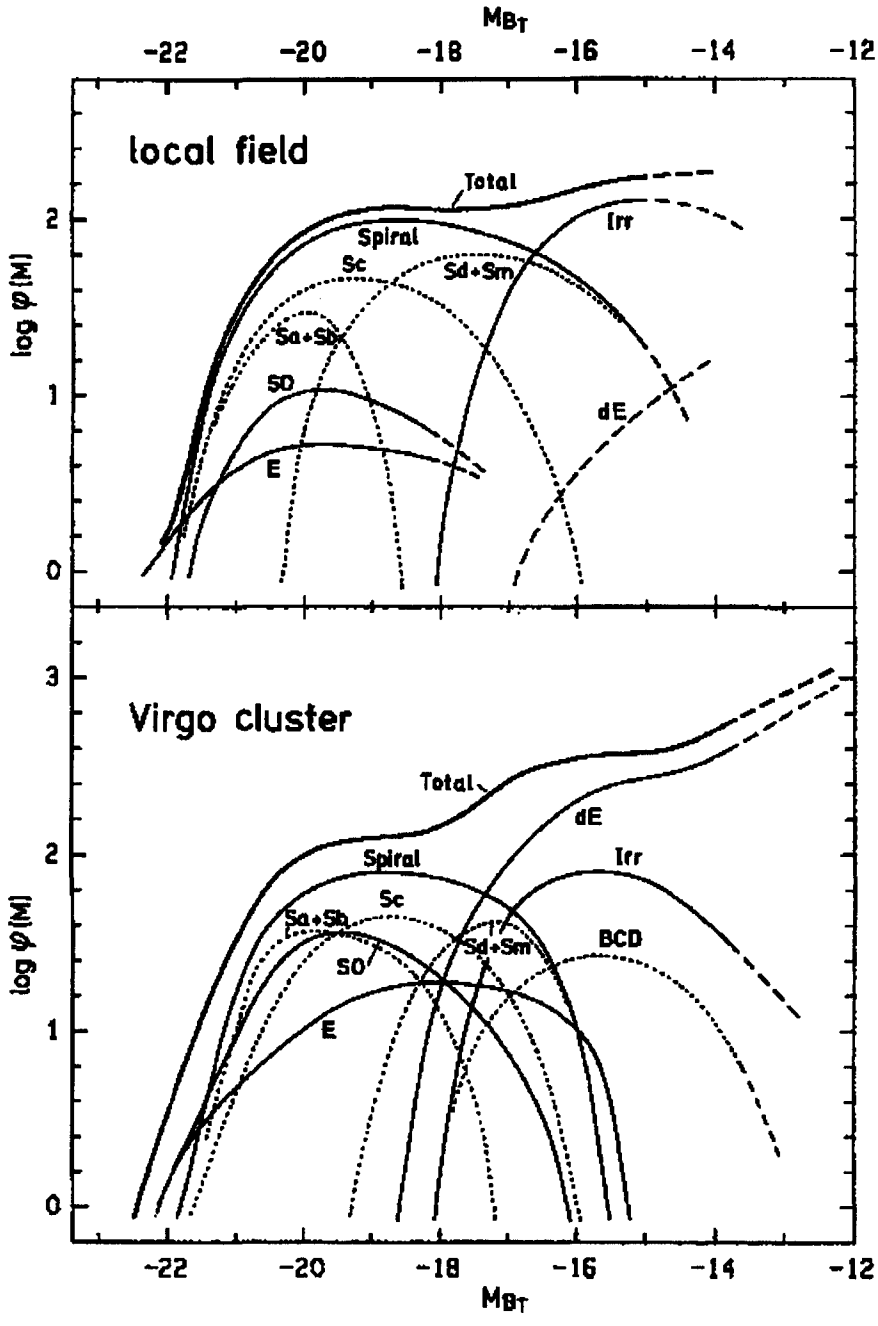

Figure 1.2: The LFs of the field (top) and Virgo cluster (bottom) from Binggeli, Sandage & Tammann (1988). The total LF (heavy line) is decomposed into the LFs of different galaxy types, with the proportion of each type depending on environment.

There are humps and bumps in the total LF according to the underlying type specific LFs." Despite this, a function proposed by Schechter (1976), of the form given by Equation 1.5 or equivalently, Equation 1.6, can often be fitted to the data.

$$\phi(M)dM = \phi^* 10^{0.4(\alpha+1)(M^*-M)} e^{-10^{0.4(M^*-M)}} dM \tag{1.5}$$

$$\phi(L)dL = \frac{\phi^*}{L^*} e^{-L/L^*} (\frac{L}{L^*})^{\alpha} dL \tag{1.6}$$

M^* (or L^*), α and ϕ^* are free parameters representing the characteristic magnitude (the "knee" in the curve), the faint end slope and the normalisation, respectively. The Schechter function is essentially a power-law at the faint end ($L \ll L^*$) and an exponential for $L > L^*$, as can be seen from Equation 1.6.

Determination of the LF in Clusters

In clusters, the determination of the LF is more straightforward than for the field, since all the galaxies are at approximately the same distance; a histogram of galaxy counts with apparent magnitude can thus be shifted by the distance modulus of the cluster to get $\phi(M)$ and M^*. However, the number counts must be corrected for foreground and background galaxies projected into the cluster area. At the faint end, contamination arising from the inability to separate stars and galaxies must be taken into account. Relativistic k-corrections must be applied to the magnitudes of galaxies to take into account changes in wavelength, bandwidth and intensity with redshift. In the NIR, k-corrections are small compared to the optical. At low Galactic latitudes, extinction must also be estimated and the magnitudes adjusted accordingly.

The usual approach for the cluster LF is to divide the magnitude range covered into bins and compute the number of galaxies in each bin, after subtracting the background and foreground counts. The number counts in a control field are used to estimate the number of galaxies not belonging to the cluster, unless membership can be determined from morphology or redshifts. A correction for stellar contamination must also be made, usually based on a statistical estimate of the number of expected misclassified objects. The parameters of the best-fitting Schechter can then be determined by χ^2 minimisation technique. The errors are calculated using Poisson statistics (approximately $\sqrt{n}$). This method can be unreliable when the number counts are low ($\lesssim$ 5 objects per bin). A different approach applies a maximum-likelihood technique to the unbinned data to obtain the Schechter parameters (see for e.g. Oegerle, Hoessel & Ernst 1986 who compared the two methods for the Abell cluster 168). Though binning provides a useful visualisation of the data, it has a number of disadvantages, discussed in depth by Andreon, Punzi & Grado (2005). The subtraction of background galaxy counts may cause the LF to be negative, if the number of counts is low and fluctuations from field to field cause the number of counts in the control field to be higher in a particular bin. If membership information is

known, no statistical background subtraction is necessary and this problem can be avoided. However Poissonian error bars may be large enough to drop below zero, also leading to the unphysical possibility of finding a negative number of galaxies.

The Schechter Parameters

The Schechter function parameters are found to be remarkably similar for the field and cluster environments, despite the differences in density and relative fractions of morphological types. Typical values in the optical are $M^*_{B_T} \sim -21.0$ and $\alpha \sim -1.25$ (Binggeli, Sandage & Tammann 1988). Not all clusters can be modelled by a Schechter function, however. The Virgo cluster, for example, has a LF with a "double wave" structure (Binggeli, Sandage & Tammann 1988) (see Fig. 1.2). Clusters containing cD galaxies seem to have a steeper bright end than those without cD galaxies. Often the brightest galaxy is excluded to obtain a better fit, particularly in cD clusters. Thompson & Gregory (1980) proposed that differences in the values of the Schechter parameters for different clusters can be attributed to the relative numbers of each morphological type. They suggested that the LF of each type remains the same but the summed LF changes depending on the fraction of each galaxy type in the area considered. Jerjen & Tammann (1997) confirmed this by showing that the type-specific LFs in the Centaurus cluster have the same shapes as those in Virgo and Fornax, although the total LFs differ. The Schechter parameters have also been found to vary depending on the region sampled within the cluster, the size of the area and the limiting magnitude (Andreon 2001). These results caution that M^* should not be used as a standard candle to infer distance. However, if the type-specific LFs are indeed universal, they may be useful distance indicators (Jerjen & Tammann 1997).

Near Infrared LFs

The determination of LFs in the near infrared began relatively recently, with the development of wide-field arrays such as the NICMOS (256 × 256) and HAWAII (1024 × 1024) HgCdTe detectors. The wide field of view of these devices makes it possible to survey larger areas in the NIR wavelength range. Previously only deep surveys over small areas were possible, making it difficult to determine a local field LF in the NIR (Huang et al. 1997) or image large enough areas over nearby clusters. The determination of the LF is limited to the bright end for shallow surveys over wide areas. As previously mentioned, the NIR is a reliable estimator of mass, with transitory star-forming events having less influence. Dust within galaxies, the intergalactic medium and the Milky Way foreground also plays a lesser role. An additional consideration for evolutionary studies is that k-corrections in the NIR are smaller than in the optical and less dependent on galaxy type. The NIR is thus useful for comparisons over a range of redshifts. As a result, the NIR LF provides information on the underlying mass distribution of galaxies and galaxy evolution.

Table 1.1: Table of Previous Field Luminosity Functions in the Near Infrared

Reference	N	M_K^* [mag]	α	Sample Notes
Heath Jones et al. 2006	60869	-24.60 ± 0.03	-1.16 ± 0.04	2MASS & 6dFGRS redshifts
Huang et al. 2003	1056	-24.47 ± 0.08	-1.38 ± 0.09	Hawaii K-band Galaxy Survey
Kochanek et al. 2001	3878	-24.16 ± 0.05	-1.09 ± 0.06	2MASS & ZCAT redshifts
Cole et al. 2001	17173	-24.21 ± 0.03	-0.96 ± 0.05	2MASS & 2dFGRS redshifts
Loveday 2000	345	-24.35 ± 0.42	-1.16 ± 0.19	Optically selected
Szokoly 1998	110	-24.31 ± 0.3	-1.27 ± 0.2	
Gardner 1997	532	-23.89 ± 0.17	-0.91	
Glazebrook et al. 1995	98	-23.81 ± 0.23	-1.04 ± 0.31	
Mobasher et al. 1993	95	-23.79 ± 0.3	-1.00 ± 0.3	Optically selected

NOTE.– M_K^* has been scaled for $H_0 = 70h_{70}$ km s^{-1} Mpc^{-1}. No corrections have been made to account for different types of K-band magnitudes used.

Field LFs in the NIR

The first determinations of the NIR field LF using a wide-field NIR selected survey were made by Gardner et al. (1997) and Szokoly et al. (1998). These were preceeded by determinations of the K-band LF using an optically selected redshift survey (Mobasher, Sharples & Ellis 1993) and small K-band selected redshift survey (Glazebrook et al. 1995). The results of these surveys are consistent with a flat faint-end slope of $\alpha = -1$, though Szokoly et al. (1998) found a slightly steeper slope of -1.27 ± 0.2. The sample used by Gardner et al. (1997) included 567 galaxies over a wider area (4.4 deg^2) than Szokoly et al. (1998) but only to a magnitude limit of $K = 15.^m0$. The Szokoly et al. (1998) study covered an area of 0.6 deg^2, obtaining 867 galaxies, down to a magnitude limit of $K = 16.^m5$. Redshifts were determined for only 175 ($\sim$ 30%) of these. Loveday (2000) also used an optically selected sample to determine the LF in the K-band for 345 galaxies.

The 2MASS survey increased the number of galaxies with NIR photometry and redshifts by an order of magnitude, making it possible to determine a NIR LF for a sample comparable to the optical, for the first time. Cole et al. (2001) and Kochanek et al. (2001) determined NIR LFs based on 2MASS Second Instrumental Release data. Jones et al. (2006) have improved on this yet further, using 2MASS photometry and a subset of the 6 degree Field Galaxy Redshift Survey (6dFGRS). Their findings suggest that a Schechter function is not an ideal fit to the LF, although the parameters obtained agree well with previous determinations.

A summary of the NIR field LFs is given in Table 1.1. Here N is the number of galaxies included in the sample, M_K^* is the absolute K-band characteristic magnitude and α is the

Table 1.2: Table of Previous NIR Cluster Luminosity Functions

Cluster	Reference	Band	M^* [mag]	α	Sample Notes
Coma	Mobasher & Trentham 1998	K		$-1.41^{+0.34}_{-0.37}$	0.03 Mpc^2
Coma	de Propris et al. 1998	H	-23.82	-0.93	central 0.53 Mpc^2
Coma	de Propris et al. 1998	K	-24.02	-0.98	central 0.53 Mpc^2
Coma	Andreon & Pello 2000	H	-23.86	-1.3	off-centre 0.30 Mpc^2
A118	Barger 1996	K'	-24.5	-1.0 $\pm$ 0.12	Centre
A118	Andreon 2001	K_s	-25.26	-1.2	1.36 Mpc^2
A118	Andreon 2001	K_s	-23.96	-0.5	0.26 Mpc^2 Main clump
A118	Andreon 2001	K_s	-23.56	-0.9	0.26 Mpc^2 NW clump
5 clusters	Trentham & Mobasher 1998	K		-1.38	Composite LF

NOTE.– M^* has been scaled for $H_0 = 70h_{70}$ km s^{-1} Mpc^{-1}. Where no value of M^* is given, the parameter was not constrained in a fit to the Schechter function. No corrections have been made to account for different types of magnitudes used, however H and K magnitudes can be compared through the colour difference of $H - K \sim 0.22$ mag (see Section 3.2.3).

faint end slope of the LF. Note that the normalisations (ϕ^*) aren't given here, since these are not relevant for comparisons to the cluster LF (see Huang et al. 2003 for a summary of field LFs determined before 2003).

Cluster LFs in the NIR

Table 1.2 summarises the most recent cluster LF determinations in the NIR. In this case M^* refers to the characteristic magnitude in the wavelength band given in Column 3. The Coma cluster is the most comprehensively studied, in both the optical and NIR bands. The NIR LF has been found to be consistent with the optical LF, shifted by the mean colour in magnitudes (Mobasher & Trentham 1998; Andreon & Pelló 2000). A number of authors have found a dip in the optical LF at $B \sim -18$ mag (see for e.g. Mobasher et al. 2003), corresponding to the transition between giant and dwarf galaxies. Jerjen & Tammann (1997) find the dip to be prominent in the Centaurus and Fornax LFs but less so for Virgo. Andreon & Pelló (2000) found a similar dip in the NIR LF of Coma, at $H \sim -22$ mag. Mobasher et al. (2003) suggest that this may be caused by the contribution of the early-type galaxies at the bright end, which could be better fit by a Gaussian, while the faint end could be fit by a power law. The observation of the dip in the NIR suggests that it is not the result of increased star formation at the bright end, which could be attributed to the hostile cluster environment.

The Schechter parameters depend on the location and size of the area surveyed and the depth of the survey. This can be seen from the variation in the parameters, for example

those of Andreon (2001) in Table 1.2, where different regions of the same cluster have been analysed using the same techniques. Andreon (2001) find that the slope of the LF is shallower in higher density regions towards the centre of the cluster, because the relative number of bright galaxies increases while the number of dwarfs decreases. The range in parameters suggests that useful comparisons between cluster LFs can only be made when corresponding areas are surveyed to similar depth. The core radius of the cluster can be used to specify the area, for example (Jerjen & Tammann 1997).

1.5 Outline of this Thesis

Chapter 2 of this thesis provides details of the NIR observations of the Norma cluster and describes the data reduction. The data reduction process consists of astrometry (Section 2.2), star-subtraction (Section 2.3) and photometry (Section 2.4). The astrometric solution and photometry are compared with 2MASS to check the consistency of the results. An internal consistency check confirms that the photometry of objects observed more than once on overlapping fields corresponds satisfactorily.

Chapter 3 presents the results of the survey and the determination of the LF. The K_s-band catalogue, which can be found in Appendix A, is described and cross-referenced with the optical catalogue of Woudt & Kraan-Korteweg (2001). The distribution of the objects and their properties are presented. The LF is derived and compared to those of other clusters and environments.

A number of avenues for future work on the LF of the cluster have become clear through the research that has gone into this thesis. In the final chapter, the resultant LF is summarised and future prospects for the study of the Norma cluster are presented.

Chapter 2

Near Infrared Observations and Data Reduction

2.1 Observations

A survey of the Norma cluster in the near infrared was undertaken with the Simultaneous 3 colour InfraRed Imager for Unbiased Surveys (SIRIUS) on the Infrared Survey Facility (IRSF), the 1.4-m Japanese telescope at the South African Astronomical Observatory (SAAO) site in Sutherland. SIRIUS allows simultaneous observations in the J ($\lambda = 1.26$ μm), H ($\lambda = 1.63$ μm) and K_s ($\lambda = 2.14$ μm) bands. It has three 1024 $\times$ 1024 HgCdTe (HAWAII) arrays. The field of view is approximately 7.8 $\times$ 7.8 arcmin^2 and the pixel scale is 0.45 arcseconds per pixel (Nagashima et al. 1999, Nagayama et al. 2003).

Ninety one slightly overlapping fields were observed by Dr P.A. Woudt, during three observing runs in June and July 2001 and July 2002, covering the area within 1/3 Abell radius of the cluster (approximately 0.6°; Woudt et al. 2005). Thirty dithered 20-second exposures (10 offset positions along a 30″ circle from the central position) were combined for each field, giving a total exposure time of 600 seconds per frame, in each of the three bands. Near infrared standard stars (Persson et al. 1998) were observed for photometric calibration. The seeing varied from approximately 1.″1 to 1.″6 with a mean full width at half maximum (FWHM) of 1.″35 (Woudt et al. 2005). Dark current subtraction, sky subtraction and flat-fielding were done using tasks in the Image Reduction and Analysis Facility[1] (IRAF) and the data reduction pipeline written by Yasushi Nakashima[2].

The central region, consisting of 47 of the 91 fields, covers an area of $\sim$ 0.6 square degrees. At the distance of the Norma cluster, this corresponds to $0.9h_{70}^{-2}$ Mpc^2. This

[1]IRAF is distributed by the National Optical Astronomy Observatory, which is operated by the Association of Universities for Research in Astronomy, Inc., under cooperative agreement with the National Science Foundation

[2]This pipeline is available as the IRAF package SIRIUS at http://optik2.mtk.nao.ac.jp/ yas/pipeline/siriuspipeline.html.

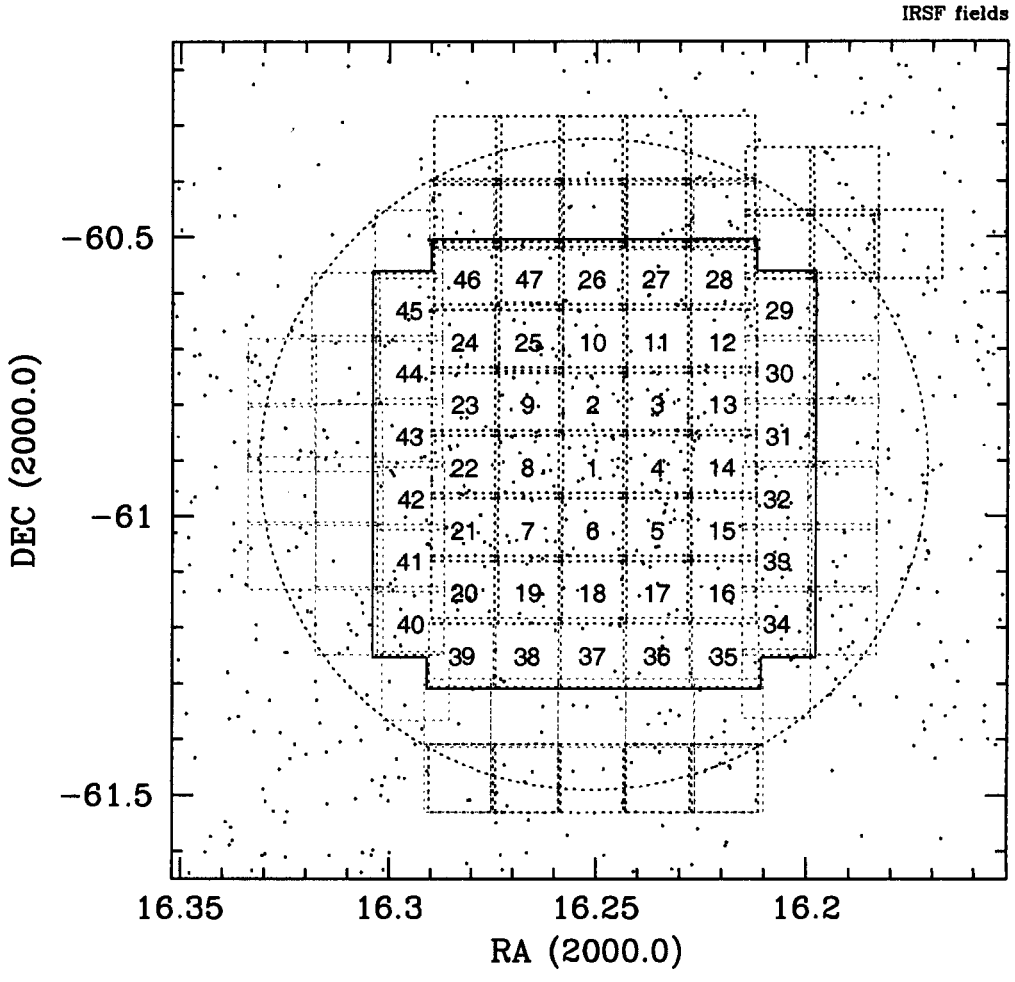

Figure 2.1: The 91 IRSF fields centered on the Norma cluster, in equatorial coordinates. Each field is 7.8 × 7.8 arcmin^2. The central 47 fields, demarcated by the solid line, have been used for the determination of the K_s band LF. The dotted circle is equivalent to $\frac{1}{3}$ Abell radius (0.6°) for the cluster. The dots represent galaxies found in a deep optical search using SRC IIIaJ sky survey plates (Woudt 1998; Woudt & Kraan-Korteweg 2001). One hundred and six galaxies were identified in the optical in the central 47 fields.

Table 2.1: Observational properties of the Norma cluster K_s-band fields used for the determination of the LF

Date	Zeropoint[a] [mag]	Extinction/ Airmass [mag]	Mean FWHM ["]	Best Seeing ["]	Worst Seeing ["]	Fields
26/06/2001	20.405 ± 0.008	0.05[b]	1.39	1.26	1.61	1 - 9, 13 - 15, 21 - 23
25/07/2001	20.425 ± 0.045	0.075 ± 0.039	1.36	1.26	1.50	10 - 12, 16 - 20, 24, 25
26/07/2001	20.393 ± 0.036	0.052 ± 0.028	1.46	1.29	1.73	35 - 45
27/07/2001	20.433 ± 0.009	0.05[b]	1.18	1.04	1.28	26 - 34, 46, 47

[a]Zeropoints determined from the standard star solution

[b]A fixed value was used rather than computing the value from the fit

region, outlined by the solid line in Fig. 2.1, has been used for the current determination of the K_s band LF of the Norma cluster. It is centred on (Right Ascension (RA), Declination (Dec)) = ($16^h15^m01^s.4$, -60°54′23″, J2000), close to the giant elliptical galaxy at the centre of the cluster (ESO 137-G006, WKK6269; Woudt & Kraan-Korteweg 2001). Details of the observations are given in Table 2.1.

2.2 Astrometry

Astrometry was done on the K_s-band images to obtain positional information. The image header world coordinate system (wcs) information for each image was updated with the solution of the transformation from pixel coordinates to J2000 equatorial coordinates. This was done using the IRAF task CCMAP. CCMAP determines the best fit based on a given list of physical image coordinates (the centroid x and y positions on the infrared array) and corresponding right ascension and declination for a number of stars on each image. Approximately 10 stars were used for the fit on each frame. *jskycat*[3] was used to identify the same stars on the 2nd generation of the Digitized Sky Survey (DSS2) images of the region. Their equatorial coordinates were obtained from the United States Naval Observatory (USNO) catalogue.

The astrometrically-calibrated images were processed to remove the majority of point sources, as will be described in Section 2.3. Objects in the "cleaned" images were identified

[3]The *jskycat* application is distributed by the European Southern Observatory (ESO) at http://archive.eso.org/JSky/.

using Source Extractor[4] (SExtr) (Bertin & Arnouts 1996). The positions of the identified objects were compared with their counterparts in the 2MASS point source catalogue (PSC) and extended source catalogue (XSC) (Skrutskie et al. 2006).

The stellarity index given by SExtr was used to distinguish between point sources and extended sources for this comparison – objects with an index above 0.9 are taken as point sources. Although the star-subtracted images were used, the number of point sources greatly exceeds the number of extended sources (6488 point sources with 2MASS $K_s \geq 11$ mag). For point sources, the mean offset in RA, $\langle \Delta \mathrm{RA} \rangle$, where $\Delta \mathrm{RA} = \mathrm{RA}_{\mathrm{2MASS}} - \mathrm{RA}_{\mathrm{SExtr}}$, and Dec, $\langle \Delta \mathrm{Dec} \rangle$where $\Delta \mathrm{Dec} = \mathrm{Dec}_{\mathrm{2MASS}} - \mathrm{Dec}_{\mathrm{SExtr}}$, were calculated for each field using a python script. The mean offset, μ, and corresponding standard deviation, σ, across the whole region were determined by averaging the offsets over all 47 fields. For extended sources, the 2MASS XSC and final catalogue of galaxies for the whole region were directly compared, rather than evaluating the offset for each field separately. Sixty nine extended sources were found in common. The results of the comparison for point sources and extended sources across the whole region are given in Table 2.2.

Figure 2.2 shows the offsets in RA and Dec for the 6,488 point sources compared. The mean values are indicated by the dotted lines. No significant trends across the region are found in either ΔRA or ΔDec, and the overall agreement with 2MASS is good, though some individual fields have large scatter and systematic offsets. The results for each field were individually examined to try to understand the large deviations from the mean, particularly obvious in ΔRA (left hand plot in Fig. 2.2). Objects at the edges of each field have larger positional offsets, accounting for some of the observed scatter. The mean offsets in RA and Dec, $\langle \Delta \mathrm{RA} \rangle$ and $\langle \Delta \mathrm{Dec} \rangle$, and corresponding standard deviations, for individual fields deviating by more than 1σ from the mean value of the whole region are given in Table 2.3. Excluding these six fields from the comparison improves the agreement in RA, however it does not significantly change the mean in Dec. The scatter in both RA and Dec is reduced (see Table 2.2).

The increased scatter in ΔRA that can be seen in Fig. 2.2 for $16.^{\mathrm{h}}21 \lesssim \mathrm{RA} \lesssim 16.^{\mathrm{h}}23$, is due to a systematic deviation from 2MASS across Field 14, with individual stars having offsets of up to an arcsecond at the edges. In the same range of RA, a dense locus of points can be seen around Field 16's mean offset of $\langle \Delta \mathrm{RA} \rangle = 0.''307$. This is the largest offset from the mean of all the fields, but the spread about this value is small. Fields 8 and 11 have the largest deviations in ΔDec. The CCMAP fits for the fields with large offsets and standard deviations were recomputed, after confirming the input. However, the offsets remained high and the reasons for the discrepancy are not yet understood. The pixel scales given by CCMAP were the same for all the images ($0.453''$ per pixel).

Figure 2.3 shows the offsets for the 69 extended sources identified by SExtr that had counterparts in the 2MASS XSC. No significant trends are found in either ΔRA or ΔDec.

[4]The Source Extractor software is described in detail in Section 2.4.1

Table 2.2: Positional comparison with 2MASS PSC and XSC over the whole region

2MASS Catalogue	No. of Objects	ΔRA ["]		ΔDec ["]	
		μ	σ	μ	σ
PSC	6488	0.041 ± 0.002	0.180	-0.022 ± 0.002	0.177
PSC (excl. 6 fields)	5667	0.024 ± 0.002	0.126	-0.025 ± 0.002	0.150
XSC	69	-0.049 ± 0.045	0.376	-0.105 ± 0.042	0.345

Table 2.3: Positional comparison with 2MASS PSC: Fields with large deviation

Field	No. of Objects	⟨ΔRA⟩ ["]	Std. Dev. ["]	⟨ΔDec⟩ ["]	Std. Dev ["]
8	135	0.120 ± 0.02	0.243	0.187 ± 0.02	0.285
11	148	0.051 ± 0.01	0.145	0.186 ± 0.01	0.145
14	136	0.261 ± 0.03	0.382	-0.035 ± 0.02	0.142
15	108	0.266 ± 0.02	0.195	-0.203 ± 0.01	0.243
16	157	0.307 ± 0.01	0.075	-0.056 ± 0.02	0.132
20	137	-0.165 ± 0.02	0.193	-0.106 ± 0.01	0.114

The mean offsets are indicated by the dotted lines in Fig. 2.3. The scatter in ΔRA and ΔDec for extended sources is ~3 times the scatter for point sources.

2.3 Star Subtraction

2.3.1 Overview

Images of the galaxies in the Norma cluster are severely affected by star-crowding, due to the location of the cluster at low galactic latitudes. It was necessary to clean the images of foreground stars before accurate photometry of the galaxies could be derived. Buta & McCall (1999) developed an IRAF routine known as KILLALL to deal with this problem for the IC 342/Maffei group of galaxies. KILLALL is built around the tasks in the DAOPHOT package (Stetson et al. 1987). It largely follows the procedure for crowded-field photometry. A point spread function (psf) is fitted to the stars. It is then used to subtract stars from the image. We applied three runs of KILLALL in the cleaning process described below. Examples of images at different stages of the cleaning process are shown in Fig. 2.4.

KILLALL: The KILLALL task divides each image into subsections. Stars within each

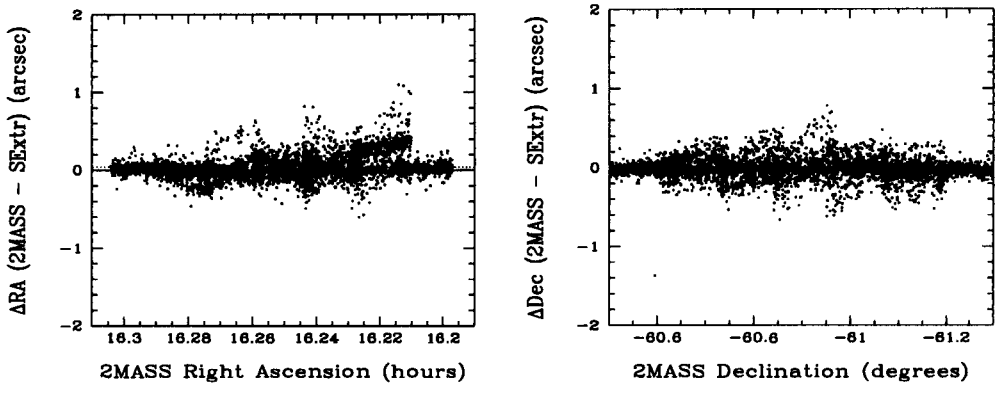

Figure 2.2: The differences in right ascension (left) and declination (right) for 6,488 point sources compared with 2MASS.

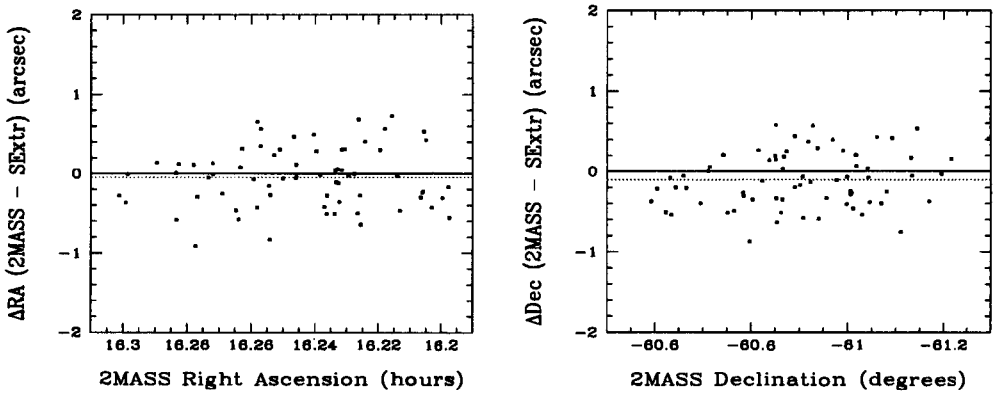

Figure 2.3: The differences in right ascension (left) and declination (right) for 69 extended sources across the region compared with the 2MASS XSC.

subsection are identified and fitted using the DAOFIND and ALLSTAR tasks. Four passes of these tasks are required in each run of KILLALL. On the first pass, a median filter is applied to subtract extended sources and large-scale variations in the sky background. In R-band images the median-filtering process smoothes background variations due to $H\alpha$ emission and thus makes a significant difference, but since this does not affect the K_s-band, it is less important here. Three further passes fit and subtract as many stars as possible. Once the procedure has been run on every subsection of the original image, the catalogues of stellar photometry created by DAOPHOT's ALLSTAR task are concatenated to form a master list of removed stars. The image subsections are reassembled to produce a star-free image. A sky background image, in which both stars and galaxies are removed, is produced by median-filtering the star-subtracted image. This is used to accurately determine the sky background around each star. Each run of KILLALL produces a catalogue of removed stars,

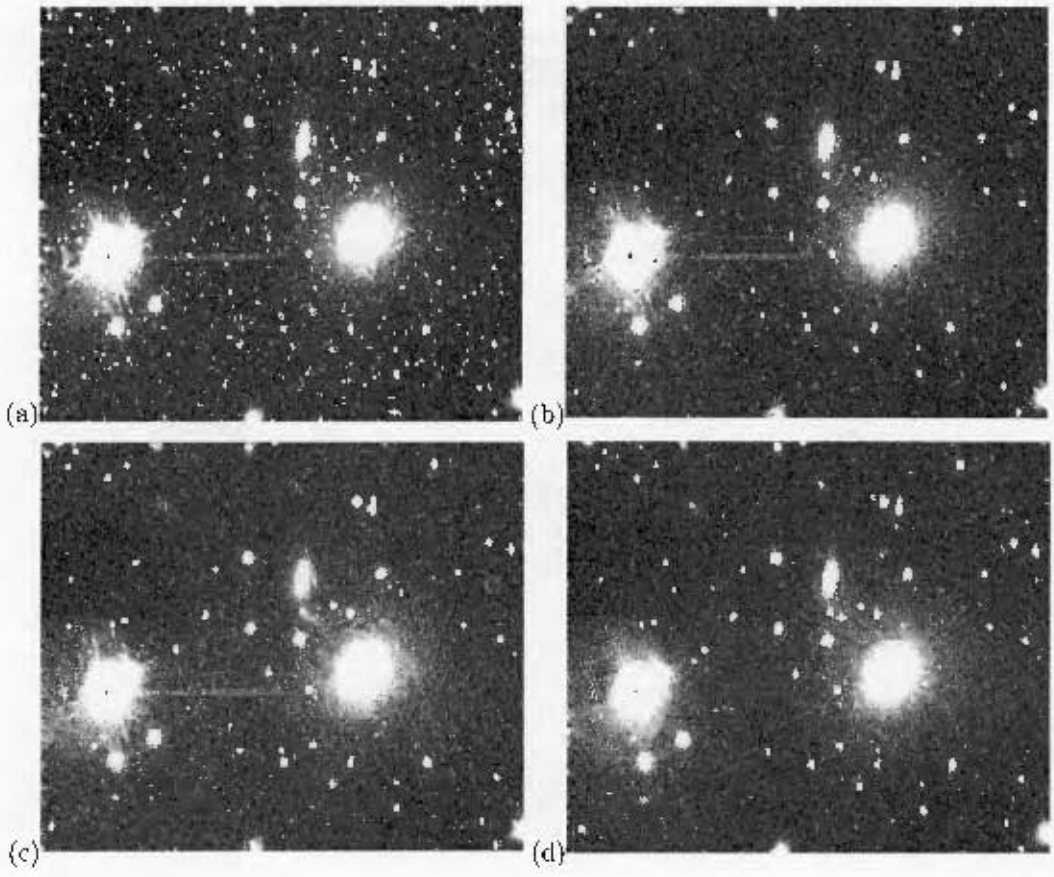

Figure 2.4: A section of the K_s band image of the central field at different stages of the cleaning process (see text for details): (a) The original image after data reduction, (b) after CLEAN1, (c) after despotting, and (d) the final image after ADDBACK and editing by hand.

a galaxy-free image, a star-free image and a sky image. The positions and magnitudes of the stars found in the first run of KILLALL are used as initial estimates for the SUBSTAR and ALLSTAR tasks in the second run.

CLEAN1: Five IRAF scripts were programmed to handle different aspects of the cleaning process. In the first script, called CLEAN1, tasks associated with the first run of KILLALL are implemented. The KILLALL parameters particular to each image, such as the size of the image, are found by reading information from the image header. KILLALL is run for the first time, using the same initial estimate of the psf and fitting parameters for all the images. The parameters are set in the parameter file *k1.pars*. Examples are given in Table 2.4. The detection threshold is 5σ, where σ is an estimate of the background noise, given by the parameter SIGMA in DATAPARS. For the optimisation of the psf, a list of possible psf stars is extracted from the catalogue produced in the first run of KILLALL.

Stars within the instrumental magnitude range -5 to -7, where the instrumental magnitude is given by

$$M_{\rm instr} = -2.5\log((\text{counts} - \text{background})/\text{sec})$$

are selected as candidate psf stars using PSELECT to create a photometry file. This file may be used as an exclusion file for the SUBSTAR task, producing an image with all but these stars subtracted. This image and file are then used as input for the PSF task, to determine an improved, image-specific psf (see Section 2.3.2).

CLEAN2: The second script, CLEAN2, checks whether an image-specific psf has been found. A star-subtracted image is created by applying the SUBSTAR task to remove stars using the improved psf. Residuals from the star removal process are indistinguishable from the background noise if the psf is adequate. If large residuals or holes remain where stars were subtracted, the psf is redetermined using adjusted fitting parameters or more stars. The parameters for KILLALL are updated and KILLALL is run a second time, using the improved psf and the values given in the parameter file *k2.pars*. Examples of the parameters are given in Table 2.4. The image-dependent full width at half maximum (DATAPARS FWHMPSF) and fitting radius (DAOPARS FITRAD) parameters are adjusted for each image. The star-subtracted image resulting from the second run of KILLALL contains fewer stars and smaller deviations in the background from the star removal process. However a number of "spots", the residuals of bright unsaturated stars, remain. The subroutine DESPOT, called within CLEAN2, removes these using non-interactive editing.

Despotting: DESPOT displays the original and latest cleaned image. The magnitude range of bright unsaturated stars that have not been cleanly subtracted is estimated. The range varies slightly from image to image but can be adjusted until the majority of spots are selected. The coordinates are marked on the image and used as input for the IMEDIT task in non-interactive mode. A circular aperture at each point is replaced with the background value found in an annulus 2 pixels wide around the point. The radius of the aperture can be adjusted for each image, but is usually chosen to be 3 or 4 pixels. Points despotted too close to extended objects or bright remaining stars resulted in larger "speckled" patches. Points despotted too close to extended sources could also affect the photometry of the sources. To avoid these problems, such points are interactively selected using TVMARK and removed from the coordinate list before imediting. This limits the automation of the task and makes the despotting process very time-consuming. However, this conservative approach was found to be best because it required less editing by hand after despotting. If holes still remain, they are edited interactively or the removed object is added back using ADDSTAR, as described below.

CLEAN3: In CLEAN3, remaining faint stars are removed in a process termed "depeppering" (Buta & McCall 1999). The images are run through the KILLALL process for a third time, but with a detection limit of only 3σ. The output catalogue from this final run is appended to a master catalogue containing the output from the second run.

Table 2.4: Examples of the parameters used as input for each run of the KILLALL task, as defined in the parameter files *k1.pars*, *k2.pars* and *k3.pars*

```
datapars.scale = 1.
datapars.fwhmpsf = 2.91
datapars.emission = yes
datapars.sigma = 7.5
datapars.datamin = -150.
datapars.datamax = 1500
datapars.noise = "poisson"
datapars.ccdread = "ron_av"
datapars.gain = "gain_av"
datapars.readnoise = 0.
datapars.epadu = 1.
datapars.exposure = "expos"
datapars.airmass = "airmass"
datapars.filter = "filter"
datapars.obstime = "time_utc"
datapars.itime = 1.
datapars.xairmass = INDEF
datapars.ifilter = "INDEF"
datapars.otime = "INDEF"
datapars.mode = "ql"
# EOF
findpars.threshold = 5.
findpars.nsigma = 1.5
findpars.ratio = 1.
findpars.theta = 0.
findpars.sharplo = 0.2
findpars.sharphi = 1.
findpars.roundlo = -1.
findpars.roundhi = 1.
findpars.mkdetections = no
findpars.mode = "ql"
# EOF
centerpars.calgorithm = "centroid"
centerpars.cbox = 6.4
centerpars.cthreshold = 0.
centerpars.minsnratio = 1.
centerpars.cmaxiter = 10
centerpars.maxshift = 1.
centerpars.clean = no
centerpars.rclean = 1.
centerpars.rclip = 2.
centerpars.kclean = 3.
centerpars.mkcenter = no
centerpars.mode = "ql"
# EOF
```

```
fitskypars.salgorithm = "mode"
fitskypars.annulus = 12.9
fitskypars.dannulus = 8.
fitskypars.skyvalue = 0.
fitskypars.smaxiter = 10
fitskypars.sloclip = 0.
fitskypars.shiclip = 0.
fitskypars.snreject = 50
fitskypars.sloreject = 3.
fitskypars.shireject = 3.
fitskypars.khist = 3.
fitskypars.binsize = 0.1
fitskypars.smooth = no
fitskypars.rgrow = 0.
fitskypars.mksky = no
fitskypars.mode = "ql"
# EOF
photpars.weighting = "constant"
photpars.apertures = "9."
photpars.zmag = 20.405 #check
photpars.mkapert = no
photpars.mode = "ql"
# EOF
daopars.function = "penny1"
daopars.varorder = -1
daopars.nclean = 0
daopars.saturated = no
daopars.matchrad = 2.
daopars.psfrad = 22.
daopars.fitrad = 3.
daopars.recenter = yes
daopars.fitsky = yes
daopars.groupsky = no
daopars.sannulus = 8.
daopars.wsannulus = 8.
daopars.flaterr = 0.75
daopars.proferr = 5.
daopars.maxiter = 50
daopars.clipexp = 6
daopars.cliprange = 2.5
daopars.mergerad = INDEF
daopars.critsnratio = 1.
daopars.maxnstar = 50000
daopars.maxgroup = 100
daopars.mode = "ql"
# EOF
```

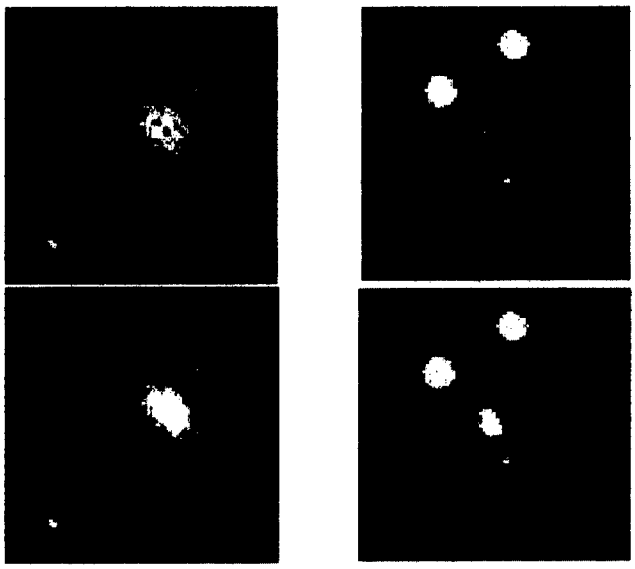

Figure 2.5: Top Panel: Examples of galaxies which had nuclei removed during the cleaning process, as they appear after CLEAN3. Lower Panel: The same galaxies once the removed parts have been replaced using ADDOBJECT. The galaxy on the left is from Field 4 and the one one the right from Field 5.

Unfortunately, the cleaning process may also remove faint obscured galaxies or the nuclei of galaxies. Examples of this are shown in Fig. 2.5, where the top panel shows two galaxies, from Field 4 and Field 5, that have had parts removed and the bottom panel shows the same galaxies with those parts replaced. When KILLALL was initially developed, it was used to remove stars on nearby low latitude galaxies in the IC 342/Maffei group, estimated to be less than 5 Mpc away (Buta & McCall 1999). In this thesis, we have a number of smaller galaxies at greater distances (approx. $69h_{70}^{-1}$ Mpc), some of which are indistinguishable from stars at first sight. It is therefore more important to replace objects or parts of objects that should not have been removed. This is done with a script called ADDOBJECT. The coordinates of all the removed objects are marked using the PDUMP and TVMARK tasks. Objects that should be added back are interactively selected using TVMARK. A python script run from within ADDOBJECT then extracts the corresponding entries from the master catalogue and adds them back to the star-subtracted image using DAOPHOT's ADDSTAR task (ADDSTAR uses the image-specific psf, adjusted by magnitude, to recreate the removed objects).

Interactive Editing: The cleaned image is interactively edited using IMEDIT, to remove spikes from saturated stars, residuals from bright stars and other cosmetic defects resulting from the cleaning process. In some cases bright stars covering galaxies are not removed by KILLALL. These are dealt with individually. The galaxy is modelled using

the ELLIPSE and BMODEL tasks within the ISOPHOTE package. Sigma-clipping is applied to mask out the star light on the first iteration. The model galaxy is subtracted from the original using IMARITH. The overlapping stars are then clearly visible and can be subtracted by fitting the psf to them. In cases where the stars are saturated, this is not successful and an IMEDIT aperture replacement is used. The model of the galaxy is then added back. A second iteration, with no sigma-clipping, may be used if necessary.

2.3.2 Point Spread Function Determination

The DAOPHOT PSF task builds a two-component model of the point spread function (psf), by fitting a function to a number of stars across the image. The analytic component of the model is one of six possible functions approximating the shape of the stellar light curve. The parameters of the analytic function are found by fitting the chosen psf stars, weighted by their signal-to-noise ratios. A two-dimensional image is created, with parameters such as the centroid, magnitude and size of the psf model (stored in the image header), as well as information on the analytic function. Depending on the order of the psf, as given by the DAOPARS VARORDER parameter, one, two or five look-up tables are created. These contain the residuals from fitting the analytic model to the actual observed psf and are used to improve the fit. If VARORDER is -1, the psf model contains only an analytic component. A VARORDER of zero corresponds to a constant psf across the image, while higher orders are used when the psf varies systematically across the frame in a linear or quadratic way. The help file for PSF provides a useful "Guide to Computing a PSF in a Crowded Field" which describes an iterative process that can be used to find the psf. This was closely followed to obtain the first estimate of the psf.

Initial estimates of the psf were determined interactively using the PSF task on two central K_s-band fields (Field 1 and Field 2, observed on June 26th, 2001). The psf for the second image was later used as the psf in the first run of KILLALL for all the images, as suggested by Buta & McCall (1999). The full width at half maximum (FWHM) for this image was determined to be 2.91 pixels (1.″31) using IMEXAMINE on a number of unsaturated stars across the image. After experimenting with different values of the fitting radius and psf radius, the values shown in Table 2.4 were used. The help file suggests a value similar to that of the FWHM for the fitting radius. The initial radius of the psf was the radius at which the signal from the brightest stars used for the psf determination disappears into the noise, i.e. 8 pixels. Large remnant annuli were found where the brightest stars were subtracted, however, as well as numerous holes even where fainter stars had been. By trial and error, it was found that the fit was much improved by increasing the psf radius to 22 pixels and lowering the maximum data value so that the brightest stars were not included in the photometry file or used to find the psf. Although this results in higher numbers of bright stars remaining in the images, the majority of fainter stars are removed more cleanly. Since the fields are small, the psf was assumed

to be constant for the initial estimate, thus the parameter VARORDER was set to zero. This was found to be a reasonable assumption, as no systematic residuals were observed in the star-subtracted image. The analytic function was initially set to "auto". The analytic model of the psf is then found using all six possible analytic functions. The "Penny1" function was found to have the smallest standard deviation and was thus used on subsequent fits.

To find an improved psf specific to each image, candidate psf stars are selected in CLEAN1 (see above). Stars appropriate for the fit are chosen interactively from these, by looking at the graphical radial profile plots and mesh plots provided by the PSF task. It was possible to select at least 20 stars across each image and for some images, up to 100 stars were chosen as possible psf stars. The list of stars to be used for the fit is then refined by graphically examining the residuals, obtained by subtracting the current psf estimate from the light profile of each star. For stars that are not well fit, large bright cores, holes or noisy annuli are visible in the radial and mesh plot. Such stars are rejected and the psf refitted.

Although the initial estimate of the psf was taken to be constant, the psf was found to vary mildly across the $8' \times 8'$ field of view of the IRSF. These variations can be exaggerated if the images are not quite in focus. At the start of CLEAN2, SUBSTAR is used to subtract stars from the original image using the improved estimate of the psf. The star-subtracted image is displayed to check how well the psf removes stars across the image. Variability was obvious in some of the star-subtracted images, as large holes or residual cores could be seen on one side of the image while stars on the other side were cleanly subtracted. In such cases, the psf was redetermined with the VARORDER parameter increased to 2. It is particularly important that enough stars are selected to sample the psf across the whole image when fitting a variable psf.

2.4 Photometry

2.4.1 Source Extraction

After the star removal process, each image is run through Source Extractor (SExtractor, Bertin & Arnouts 1996). This software automatically extracts and does photometry on objects in astronomical images. SExtractor is ideal for this work because of its flexibility and speed, allowing many images to be processed quickly, with the outcome of a source catalogue with photometric parameters.

The process is made up of six steps: background estimation, detection of objects, separation of neighbouring objects, cleaning of spurious detections, photometry and star/galaxy classification. Each of these steps is described in detail in Bertin & Arnouts (1996) and summarised below. Parameters controlling the various sub-processes are stored in a configuration file, an example of which is shown in Table 2.5. The configuration file can be

updated for each image and easily adjusted to test the choice of parameters.

Background Estimation: To estimate the sky background, the image is divided up into a grid. The sky value is determined for each mesh of the grid, using a combination of σ-clipping and mode estimation. The mean and standard deviation (σ) of the local background histogram are calculated and outliers beyond 3σ excluded until convergence is reached. The mode is taken to be the mean of the clipped histogram if σ doesn't change by more than 20% during this process. Otherwise the field is considered crowded. A combination of the mean and median, given by

$$\text{mode} = 2.3 \times \text{median} - 1.5 \times \text{mean} \tag{2.1}$$

is then used as an estimate of the mode. A median filter is applied, to smooth over local variations due to bright objects in the image. A background map is created using bilinear interpolation across the filtered grid. The detection threshold is based on the background map. Since the flux from an object is calculated by subtracting the background contribution from the total flux, the background estimation is very important for photometry. The local background, re-estimated in an annulus around each object, can be used for photometry, rather than the value from the background map.

The size of the grid meshes can be chosen, as well as the number of meshes to be smoothed over during filtering. If the mesh size is too small, the background estimation will be strongly influenced by individual objects. If too large, small scales changes across the image will not be represented. To balance these factors, a mesh size of 64 pixels and filter size of 5 meshes were found to be optimal. The background for the central field was overestimated in regions due the presence of the giant cD galaxy and large saturated stars. However for most fields the average size of objects is much smaller than the chosen mesh size, avoiding this problem. A number of different mesh sizes were tested for the central field but the overall magnitude difference was found to be small (less than 0.01 mag for stars and 0.05 mag for extended sources). A constant background value gave similar results. The same mesh size and filter size were thus used for all the fields.

The background and rms map can be viewed after each run, which is useful for checking the background settings. The parameters were tested by comparing the photometry of stars in test fields with those matched in the 2MASS PSC. A constant background value can be manually chosen, rather than using the value found by SExtractor, however this does not allow for variations across the image. The final values used for all parameters are shown in the example configuration file in Table 2.5.

Detection: For an object to be detected, it must consist of a number of connected pixels above the detection threshold. The minimum area, in pixels, and the detection threshold are specified in the configuration file. The detection threshold can be relative to the background, or an absolute surface brightness or number of counts. In this case the detection threshold was chosen to be 3σ above the background value. A gaussian

Table 2.5: An example of the configuration file used as input for Source Extractor

```
# Configuration file for SExtractor 2.3.2
#------------------------------- Catalog ------------------------------------

CATALOG_NAME    output/catalogs/K.01.cat       # name of the output catalog
CATALOG_TYPE    ASCII_HEAD      # "NONE","ASCII_HEAD","ASCII","FITS_1.0"
# or "FITS_LDAC"
PARAMETERS_NAME config_files/K.01.param    # name of the file containing catalog contents

#------------------------------ Extraction ----------------------------------

DETECT_TYPE     CCD             # "CCD" or "PHOTO"
#FLAG_IMAGE     flag.fits       # filename for an input FLAG-image
DETECT_MINAREA  10              # minimum number of pixels above threshold
DETECT_THRESH   3   # <sigmas> or <threshold>,<ZP> in mag.arcsec-2
ANALYSIS_THRESH 3   # <sigmas> or <threshold>,<ZP> in mag.arcsec-2
FILTER          Y               # apply filter for detection ("Y" or "N")?
FILTER_NAME     config/gauss_3.0_5x5.conv       # name of the file containing filter
DEBLEND_NTHRESH 64              # Number of deblending sub-thresholds
DEBLEND_MINCONT 0.001           # Minimum contrast parameter for deblending
CLEAN           Y               # Clean spurious detections? (Y or N)?
CLEAN_PARAM     1.0             # Cleaning efficiency
MASK_TYPE       CORRECT         # type of detection MASKing: can be one of
# "NONE", "BLANK" or "CORRECT"

#------------------------------ Photometry ----------------------------------

PHOT_APERTURES  22.22, 31.11, 44.44, 66.67      # MAG_APER aperture diameter(s) in pixels
# corr. to 5,7,10,15 arcsec radius ap
PHOT_AUTOPARAMS 2.5, 3.5        # MAG_AUTO parameters: <Kron_fact>,<min_radius>
PHOT_FLUXFRAC  0.5         # half-light radius
SATUR_LEVEL     50000.0         # level (in ADUs) at which arises saturation
MAG_ZEROPOINT   24.026827          # magnitude zero-point
MAG_GAMMA       4.0             # gamma of emulsion (for photographic scans)
GAIN            66.667          # detector gain in e-/ADU
PIXEL_SCALE     0.45            # size of pixel in arcsec (0=use FITS WCS info)

#------------------------ Star/Galaxy Separation ---------------------------

SEEING_FWHM     1.5                # stellar FWHM in arcsec
STARNNW_NAME    config/default.nnw              # Neural-Network_Weight table filename

#------------------------------ Background ----------------------------------

BACK_TYPE AUTO
#BACK_VALUE 0.
BACK_SIZE       64          # Background mesh: <size> or <width>,<height>
BACK_FILTERSIZE 5               # Background filter: <size> or <width>,<height>
BACKPHOTO_TYPE  GLOBAL # can be "GLOBAL" or "LOCAL"
#BACKPHOTO_THICK 24

#------------------------------ Check Image ----------------------------------

CHECKIMAGE_TYPE APERTURES   # can be one of "NONE", "BACKGROUND",
# "MINIBACKGROUND", "-BACKGROUND", "OBJECTS",
# "-OBJECTS", "SEGMENTATION", "APERTURES",
# or "FILTERED"
CHECKIMAGE_NAME output/check_images/K.01.ap.fits # Filenames for the check-images
```

convolution mask, adjusted to match the average seeing, was used to improve the detection of faint sources.

Deblending: Objects that are very close together may initially be detected as one object and need to be separated in a process termed "deblending". To distinguish overlapping objects as separate, there must be a detectable saddle in the light profile. Two or more objects are separated if their individual fluxes are each greater than a fraction of the composite object's flux. This is determined by dividing the light profile into exponentially spaced levels and calculating the flux at each level. The deblending algorithm depends critically on the number of levels into which the profile is divided and the fraction of flux each component must contain. These parameters are given in the configuration file (the number of deblending thresholds and minimum contrast). Blended objects made up of neighbouring stars were identified by eye and used as test cases to find the best value of the deblending parameters. Increasing the parameter controlling the number of thresholds to 64 and using a minimum contrast of 0.001 improved the separation of overlapping objects.

Before photometry is done, there is an option to check whether each object would have been detected without the contribution of light from its neighbours, since often there are spurious detections near saturated stars or elliptical galaxies, due to the higher local background. A Moffat profile, given by Equation 2.2, is is fit to neighbouring objects.

$$\frac{I(r)}{I(0)} = \frac{1}{(1 + k \times r^2)^{\beta}} \tag{2.2}$$

Here $I(r)$ is the intensity at radius r, $I(0)$ is the central intensity, k and β are parameters. The additional light from the wings of the neighbour's profile is subtracted. If the flux is no longer above the detection threshold, the object is rejected. This is controlled by the cleaning parameter in the configuration file (β in the above equation).

Photometry: There are four types of photometry that can be output by SExtractor: isophotal, corrected isophotal, aperture and Kron photometry. The area of pixels above the detection threshold is the isophotal area of the object. The flux from within this area, after subtracting the background contribution, is the isophotal flux. The number of counts is converted to a magnitude using the effective gain and the magnitude zeropoint. The effective gain, given by Equation 2.3 for a median combined image, is dependent on the gain of the detector and the number of frames combined, N. In this case, 20 frames have been combined, each with an exposure time of 30 seconds. With an instrument gain of 5 electrons/ADU, the effective gain is 66.67.

$$\text{gain}_{\text{eff}} = 2 \times N \times \frac{1}{3} \text{gain}_{\text{detector}} \tag{2.3}$$

The zeropoints for each night have been found using standard star solutions, and are given in Table 2.1. These are used to calculate the magnitude zeropoint (`magzp`), given by Equation 2.4, where zp is the zeropoint from the standard star solution. The magnitudes

are also corrected for the extinction due to the atmosphere, using the extinction per airmass (given in Table 2.1) and the airmass value extracted from the image header.

$$\text{magzp} = \text{zp} + \text{airmass} \times \text{ext/airmass} + 2.5 \log_{10}(\text{ave.exp.time}) \tag{2.4}$$

The best estimate of total magnitude for galaxies is based on Kron photometry (Kron 1980). The Auto or Kron magnitude is found using an adjustable elliptical aperture. There are two parameters that can be adjusted: the minimum radius of the ellipse (R_{min}) and a multiplicative factor k which influences the size of the ellipse axes. The default values of $R_{min} = 3.5$ and $k = 2.5$ were retained throughout. A second estimate of the total magnitude is given by a corrected isophotal magnitude. The isophotal magnitude is adjusted to take flux in the wings of an object's profile into account. It is assumed the profile is approximately Gaussian due to the atmosphere. This magnitude is most reliable for stars, though it may be useful for disk galaxies (Bertin & Arnouts 1996). For consistency, we have chosen to use the Auto magnitude as the total magnitude for all the identified galaxies.

Magnitudes within a fixed circular aperture are useful for for obtaining colours and comparison with other data sets, where the total magnitudes have been estimated differently. Radii of 5″, 7″, 10″ and 15″ were chosen for aperture photometry. The diameter of each aperture is given in the configuration file, in pixel units rather than arcseconds. Geometric quantities include the half-light radius, the radius enclosing an area containing half the emitted light from the object, an estimate of the Full Width at Half Maximum (FWHM) assuming a Gaussian core, the ellipticity $(1 - \frac{b}{a})$ and elongation $(\frac{a}{b})$ of the Kron ellipse, where a and b are the semi-major and semi-minor axes, respectively.

SExtractor provides a set of useful images to check the output. In addition to the background and rms maps, mentioned above, an image showing how the area has been broken up into objects (the segmentation image) and an image showing the photometric apertures around each object (the aperture image) can be viewed. Examples of these are shown in Fig. 2.6

2.4.2 Star-Galaxy Separation

A number of techniques have been used to distinguish between stars and galaxies, usually based on two parameters, such as the magnitude and central surface brightness or magnitude and isophotal area. Objects identified by SExtractor are classified as stars or extended sources, using a Neural Network (NN) to distinguish between them. A NN allows many more parameters to be taken into account. In this case there are 10 parameters: the seeing FWHM (input by the user in the configuration file), the peak intensity and 8 isophotal areas. Taking a number of isophotal areas into account utilises much more of the information available in the object's profile. The NN outputs an index between 0

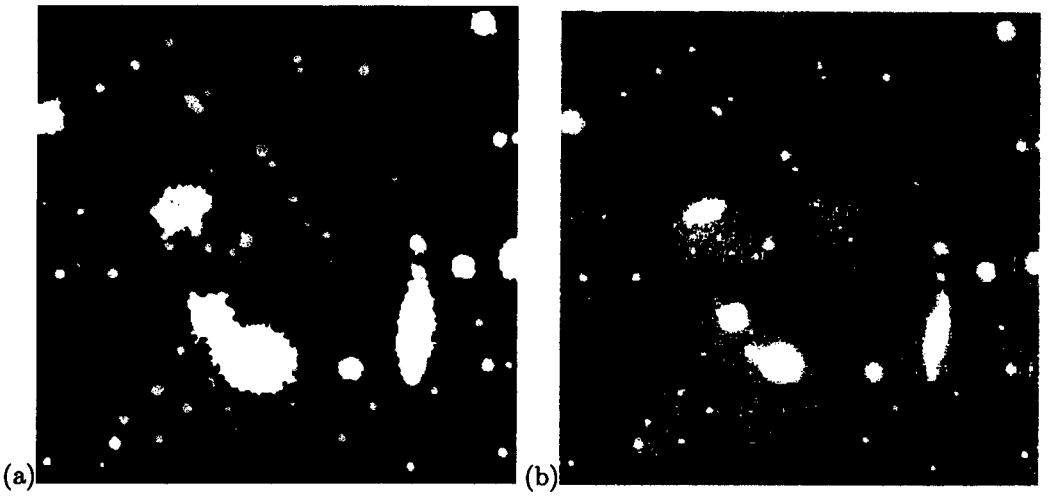

Figure 2.6: (a) The segmentation image given by SExtractor for a section of Field 5, showing how pixels above the threshold are separated into objects, and (b) the aperture image for the same section, showing the circular and elliptical apertures used for aperture and Kron photometry.

and 1, indicating the degree of stellarity. Point sources have and index close to 1, while galaxies have an index close to 0. Objects that cannot be clearly classified as either stars or galaxies are allocated a value between 0 and 1.

Classification is difficult for faint and blended objects. In the ZOA, the star crowding and extinction make the problem even more severe. The stellarity index given by SExtractor is plotted versus magnitude in Fig. 2.7 for objects found in all 47 fields. Note the group of bright objects with an index of approximately 0.8. These are saturated stars. The separation between stars and galaxies begins to be indeterminate for objects with $K_s \gtrsim 11^m$. The stellarity index is not a reliable indicator for most objects beyond $K_s = 13^m$. For this reason, we decided to identify galaxies by examining the images by eye. More uncertain cases are found in images with worse seeing: faint stars are blurred, becoming indistinguishable from extended sources, groups of faint stars may appear to be nebulous and even bright blended stars may appear to be a single elongated object. Bright blended stars can be distinguished from galaxies because the surface brightness of stars drops off rapidly compared to extended sources. Often two distinct stars can be resolved by changing the cut level of the image.

Possible extended sources identified by SExtr were classified as "galaxies", "candidates" or "uncertain" by examining each image by eye. The resulting catalogue was compared to the deep B-band catalogue from the IIIaJ Sky Survey plates (Woudt 1998; Woudt & Kraan-Korteweg 2001). Deep R-band images (Markus 2006) were used to confirm or reject candidates as galaxies. The R-band images have higher spatial resolution of 0.237

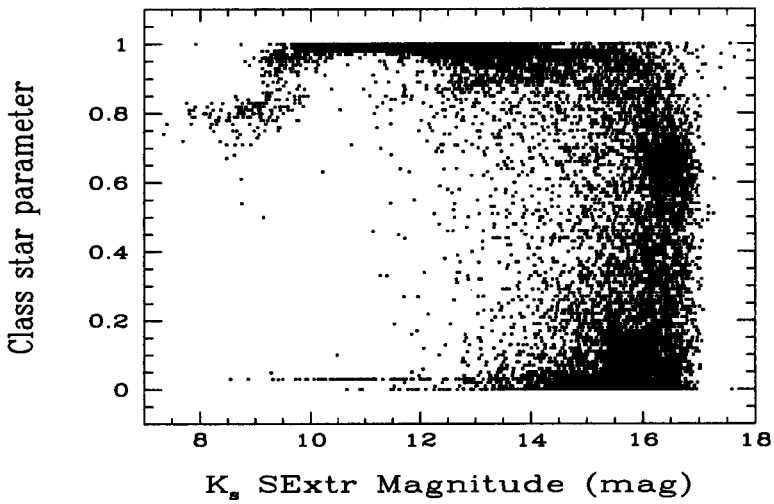

Figure 2.7: Stellarity index against magnitude for all objects found by Source Extractor. Point sources have an index close to 1, while extended sources have an index close to 0. See text for details.

arcsec/pixel compared to the K_s band image resolution of 0.453 arcsec/pixel and are thus useful for resolving pairs or groups of stars identified as candidates in the K_s-band. A total of 390 objects were identified, 235 of which are classified as galaxies and 155 as candidate galaxies. The final catalogue is given in Appendix A and described in Section 3.1.1.

2.5 Photometric Verification

2.5.1 Internal Consistency Check

Objects identified in the overlapping regions on more than one field were used to check consistency between fields. A python script was used to find objects on neighbouring fields within 1.″5 of each other. Objects with incomplete aperture data due to their proximity to the edge of a field were excluded from the comparison. More than 100 objects in each field could be compared with corresponding objects in the surrounding fields. Nine test fields (the shaded fields in Fig. 2.8) were compared with the fields surrounding them, thus covering the whole region. The mean Auto magnitude difference, $\langle \Delta K \rangle = \langle K_{\text{test field}} - K_{\text{surrounding fields}} \rangle$, and standard deviation for each test field are given in Table 2.6. These results reflect the maximum difference, since the objects compared are all near the edges of the images, where their parameters are least well determined. The results show that there are no systematic differences in photometry over the region. The differences in magnitudes

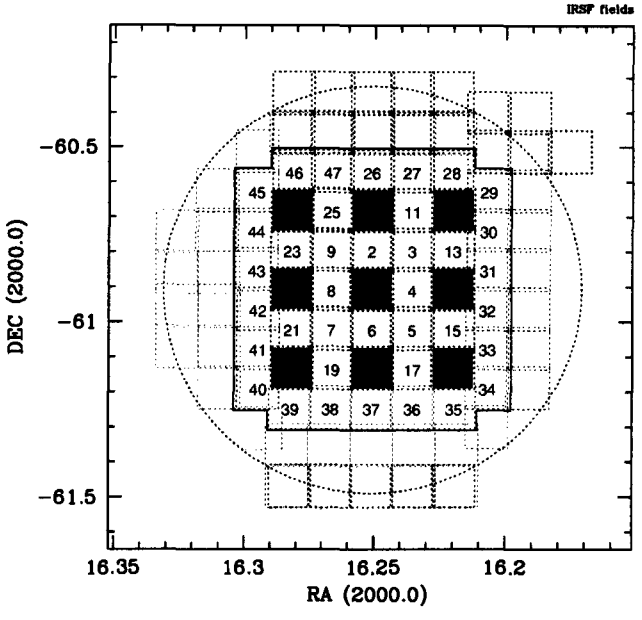

Figure 2.8: The 91 IRSF fields centered on the Norma cluster, in equatorial coordinates, as shown in Figure 2.1. Here the 9 shaded fields have been used to check the consistency of photometry, by comparing the magnitudes of objects in overlapping regions on surrounding fields with those in the test fields.

for the objects in Field 16 and the overlapping fields are plotted in Fig. 2.9, as an example. Field 1 shows the largest mean difference in magnitudes. This can be attributed to the difference in background determination, due to the number of saturated stars and central cD galaxy, as described in Section 2.4.1 above. Further comparisons were made to check the consistency of isophotal and isophotal-corrected photometry. The results using these magnitudes were consistent with the Auto magnitude comparison.

Some objects were found in one field but not in an overlapping field. This was initially a cause for concern, but can be attributed to differences in image quality and the star-removal process. For example, objects towards the right-hand edge of some of the images show systematic elongation. Faint stars in affected fields appear to be extended sources. The star may be completely removed during the cleaning process on another field where the seeing is better and thus only identified on one of two overlapping fields. This was taken into account during the final selection of extended sources, where objects were examined by eye in each of the images in which they appear.

Table 2.6: Photometric comparison of objects in overlapping fields

Field	No. of Objects	$\langle \Delta K \rangle$ [mag]	Std. Dev. [mag]
1	128	-0.060 ± 0.018	0.201
10	132	0.006 ± 0.014	0.160
12	106	-0.041 ± 0.011	0.115
14	137	0.000 ± 0.018	0.209
16	160	-0.018 ± 0.010	0.131
18	143	0.008 ± 0.009	0.111
20	128	-0.016 ± 0.007	0.077
22	179	-0.015 ± 0.016	0.210
24	145	-0.014 ± 0.015	0.184

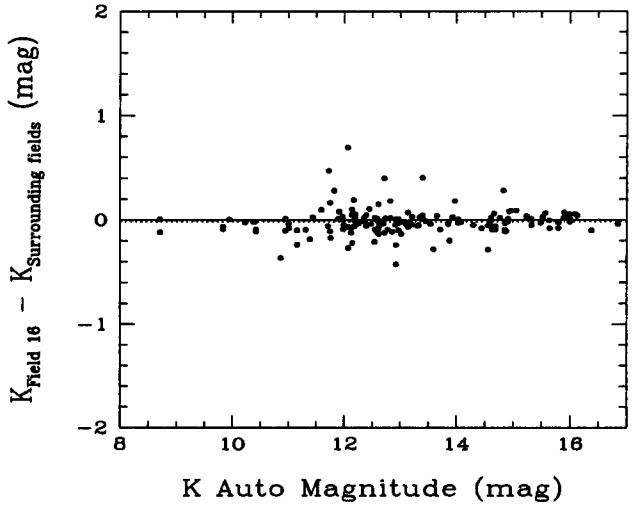

Figure 2.9: The differences in magnitude for objects found in Field 16 and the overlapping regions of surrounding fields.

2.5.2 Comparison with 2MASS Photometry

The photometric system of SIRIUS on the IRSF is the same as that of 2MASS, allowing for the direct comparison of photometry. The IRSF survey of the Norma Cluster improves on the data for this region provided by 2MASS, due to the depth of the survey and differences in resolution of 2MASS and the IRSF (2.0 arcsec/pixel vs. 0.45 arcsec/pixel). The completeness limit of this survey is two magnitudes fainter than that of 2MASS when candidate galaxies are included in the sample ($K_s = 15.^{\rm m}25$ vs. $K_s = 13.^{\rm m}1$; see Section 3.1.4 and Section 1.2), while galaxies can be identified beyond $K_s = 16$ mag, 3 magnitudes deeper than the 2MASS completeness limit. The higher spatial resolution of the IRSF makes it possible to separate stars and extended sources to a greater extent, thus improving star subtraction over large galaxies. Postage stamp images of three galaxies from the 2MASS XSC are compared to the corresponding images from the IRSF in Fig. 2.10 to illustrate the differences between the surveys.

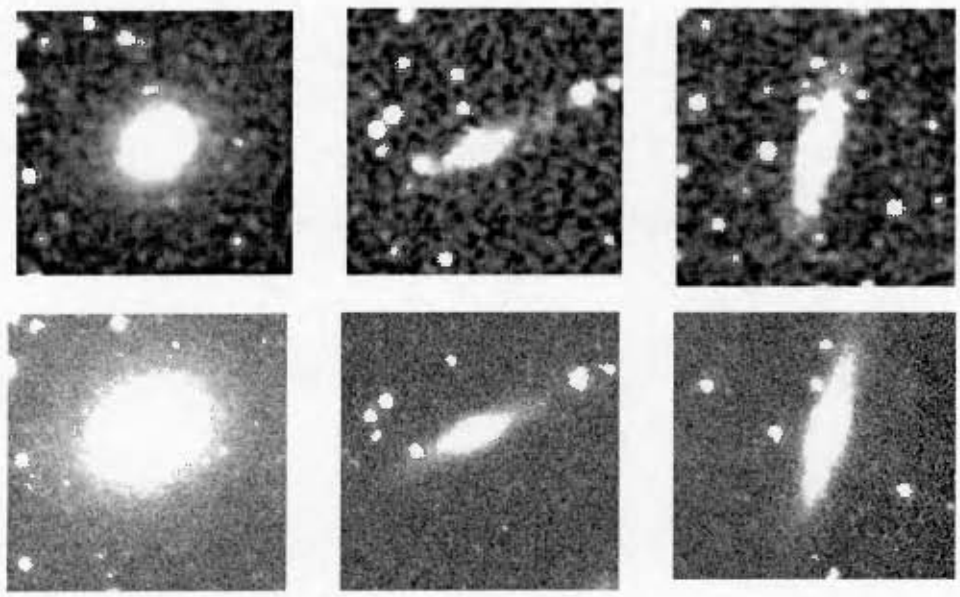

Figure 2.10: Postage stamp K_s-band images of three galaxies from the 2MASS XSC (top) and the corresponding processed IRSF images (bottom).

The isophotal-corrected magnitudes of point sources in each star-subtracted image are compared to the K_s-band magnitudes given in the 2MASS PSC in Fig. 2.11. For this comparison, point sources were taken to be those objects with a stellarity index above 0.9. Only stars with $11^{\rm m} \lesssim K_s \lesssim 15^{\rm m}$ were compared, in order to avoid bright saturated stars. No significant trend is found, although there are a number of objects with significantly different magnitudes in the two catalogues. The objects with a negative difference are

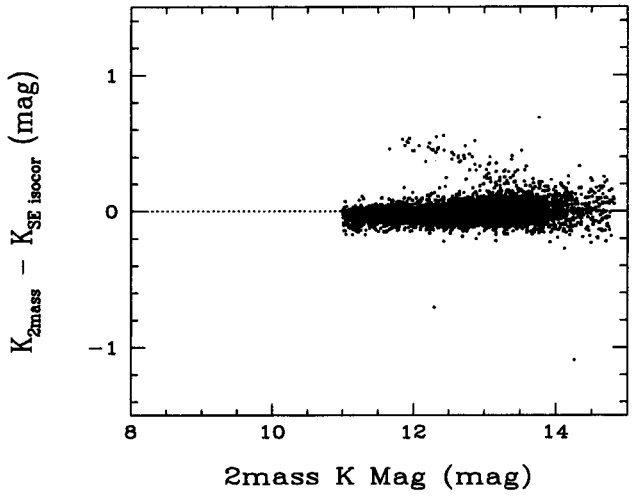

Figure 2.11: The differences in magnitudes for 6,488 point sources across the region compared with the 2MASS PSC. The objects with large offsets, forming a "trail" above the mean are objects near the edges of fields or near a bright star or galaxy.

brighter in the 2MASS catalogue - these are likely to be unresolved pairs or small groups of stars. The individual objects resolved by the IRSF have lower magnitudes than the combined object identified by 2MASS. A few objects were found to have very large offsets. On closer inspection, these were identified as objects cut-off on the edges of fields or found very near an edge. Some objects found to be brighter in this survey than in 2MASS are situated near bright stars or galaxies. These objects and those near an edge account for the diagonal "trail" above the mean in Fig. 2.11. The mean offset and corresponding standard deviation for 6,488 objects across the 47 fields are

$$\mu = -0.029 \pm 0.003 \text{ mag}, \sigma = 0.236 \text{ mag}.$$

The comparison to the 2MASS XSC yielded 69 matches. The differences between the Auto magnitude given by SExtr and the 2MASS "K ext" magnitude (an estimate of the total magnitude, based on the flux within a Kron aperture or extrapolated fit to the surface brightness profile of the object) for these objects are shown in Fig. 2.12. The mean difference and standard deviation are

$$\mu_{\text{Auto},K_{\text{ext}}} = -0.093 \pm 0.026 \text{ mag}, \sigma = 0.217 \text{ mag},$$

A straight line with equation

$$\Delta K_s = (0.068 \pm 0.018) K_s - (0.865 \pm 0.200) \text{ mag}$$

was fitted to the data, with a standard deviation of 0.198 mag and $R^2 = 0.184$. A comparison of the 2MASS "K 20" magnitude, the magnitude within the 20 mag/arcsec^2 isophote, and the Auto magnitude given by SExt yielded a mean and standard deviation of

$$\mu_{\mathrm{Auto},K_{20}} = 0.071988 \pm 0.027 \text{ mag}, \sigma = 0.227 \text{ mag},$$

A similar trend was found for this comparison: a straight line given by

$$\Delta K_s = (0.092 \pm 0.016) K_s - (0.986 \pm 0.188) \text{ mag}$$

was fitted to the data, with a standard deviation of 0.188 mag and $R^2 = 0.325$. In both cases, the low R^2 parameter indicates that the trend is not significant. The observed trend indicates that the 2MASS magnitudes of bright objects are systematically brighter than the IRSF magnitudes. The most likely cause of this is that fewer stars superimposed on bright galaxies have been resolved and removed by 2MASS. The stellar flux thus contributes to the total magnitude of the galaxy. The IRSF magnitudes are brighter for faint objects, due to the improved resolution of the instrument. The scatter increases towards the faint end.

The isophotal magnitudes of the two surveys are compared in Fig. 2.13. The mean difference and standard deviation are

$$\mu_{\mathrm{Iso},K_{20}} = -0.207 \pm 0.023 \text{ mag}, \sigma = 0.187 \text{ mag},$$

indicating that the 2MASS magnitudes within an isophote of 20 mag/arcsec^2 are 0.2 mag brighter than the isophotal magnitudes measured by SExtr. In this case, a linear fit to the data gave

$$\Delta K_s = (0.007 \pm 0.016) K_s - (0.290 \pm 0.188) \text{ mag}$$

with a standard deviation of 0.189 mag and $R^2 = 0.003$, confirming that the data are consistent with a horizontal line through the mean. However there is a systematic offset, as expected, due to the difference in the isophotal limits of the surveys.

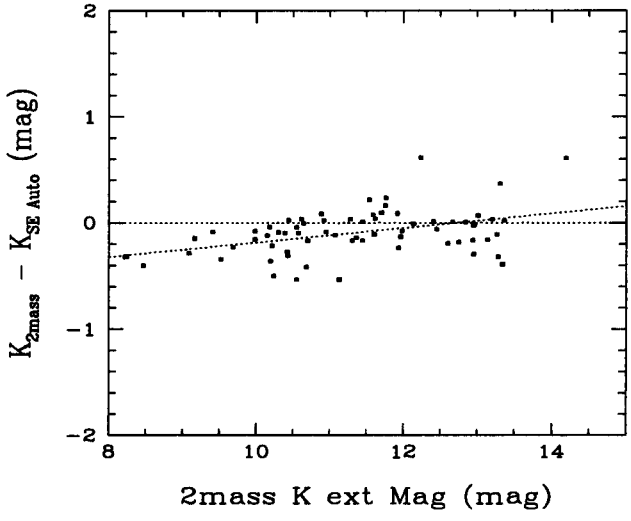

Figure 2.12: The differences between 2MASS "K ext" magnitude and SExtr Auto magnitude for 69 extended sources across the region compared with the 2MASS XSC.

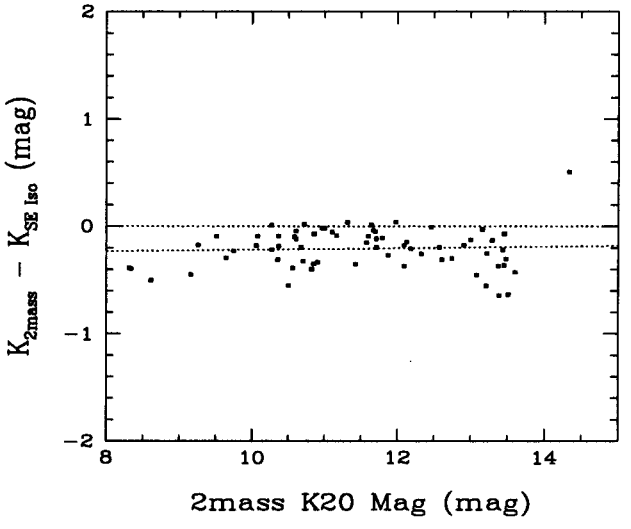

Figure 2.13: The differences between 2MASS "K20" magnitude and SExtr Isophotal magnitude for 69 extended sources across the region compared with the 2MASS XSC.

Chapter 3

Data Analysis and Results

3.1 Properties of the Observed Galaxies

3.1.1 The Catalogue

The catalogue of objects identified in the K_s-band contains 390 objects, 235 of which are classified as galaxies and 155 as candidate galaxies. The catalogue, given in Appendix A, contains the following information:

Column 1: Identification number from this survey.

Column 2: Identification number from the catalogue of Woudt & Kraan-Korteweg (2001), if a corresponding object was found in their deep optical search of the SRC IIIaJ sky survey plates, or an 'R' indicating identification on the R-band images of the cluster.

Column 3: Right Ascension (RA) and Declination (Dec) (J2000)

Column 4: Galactic longitude (l) and latitude (b) in degrees

Column 5: Galactic Extinction in the K_s-band (A_{K_s}) in magnitudes, as derived from the Schlegel, Finkbeiner & Davis (1998) reddening maps (see Section 3.1.2)

Column 6: Classification as likely galaxy (G) or candidate (C), based on eye-balling of the K_s- and R-band images of the cluster

Column 7: Total K_s-band magnitude and error, given by the Auto (Kron) magnitude of SExtr (uncorrected for galactic extinction or k-correction for redshift)

Column 8: B_J magnitude, corresponding approximately to B_{25} isophotal magnitude, from the catalogue of Woudt & Kraan-Korteweg (2001). The typical 1σ uncertainty associated with these magnitudes is $0.^{\mathrm{m}}5$.

Column 9: Diameter of the object (D) in arcseconds, as estimated from SExtractor's `ISOAREA` parameter: $D \simeq 2A_{\mathrm{iso}} = 2\sqrt{\frac{\mathtt{ISOAREA}\times\mathtt{ELONGATION}}{\pi}}$ where A_{iso} is the isophotal semi-major axis, `ISOAREA` is the isophotal area and `ELONGATION` is the ratio of the semi-major and semi-minor axes.

Column 10: Heliocentric velocity in km s^{-1} from NED[1], with additional sources from 2dF spectroscopy (Woudt et al. 2007, in preparation).

Column 11: The field/s the object was identified in, corresponding to those shown in Fig. 2.1, followed by a photometric flag in brackets. The flag indicates the reliability of photometry in each image in which the object was detected. The number given is the sum of one or more of the following flags: "0" indicates reliable photometry, "1" indicates that neighbouring objects may have an influence on the photometry of the object, "2" indicates that the object was originally blended with another object, "4" indicates that at least one pixel is saturated, "8" indicates that the object was truncated due to proximity to the boundary of an image, "16" indicates that the object's aperture data is incomplete or corrupted, "32" indicates that the object's isophotal data is incomplete or corrupted. If an object is identified in more than one field, the magnitude given in Column 7 is the average of the data from all fields in which the photometric flag is zero.

3.1.2 Magnitude Corrections

The Norma cluster is located at a mean heliocentric recession velocity of 4844 ± 63 km s^{-1} (Woudt 1998), which translates to a velocity-distance of $v_{CMB} = 4928 \pm 63$ km s^{-1} in the CMB rest frame (Kogut et al. 1993). Although the Norma cluster is nearby ($z = 0.01615$), the k-correction to account for differences in the rest-frame and observed wavelengths is not negligible. For redshifts smaller than $z = 0.2$ the k-correction in the K-band is $-3.3z$ magnitudes to first order (Glass 1999). At the redshift of the Norma cluster, the correction is thus -0.05 mag. The effective distance modulus of the cluster is

$$m - M = 5 \log D(z) + 25 + k(z) + A(l, b) \tag{3.1}$$

where $D(z)$ is the distance to the cluster in Megaparsecs (rather than parsecs, as in the usual definition), $k(z)$ is the k-correction and $A(l, b)$ is the galactic extinction, as described below. Using a distance of $70h_{70}^{-1}$ Mpc (assuming that the cluster is at rest with respect to the CMB rest frame) and a k-correction of -0.05 magnitudes, the distance modulus for the Norma cluster becomes

$$m - M = 34.18 - 5 \log h_{70} + A(l, b) \tag{3.2}$$

The magnitude of each galaxy in the catalogue can be corrected for Galactic extinction due to the dust of the Milky Way described in Section 1.3. The colour excess $E(B - V)$ at the position of each galaxy is determined from the dust maps of Schlegel, Finkbeiner & Davis (1998). This is converted to a K_s-band magnitude correction using the near-infrared extinction law of Cardelli, Clayton & Mathis (1989) with a value of $R_V = 3.1$, such that

$$A_{K_s}(l, b) = 0.37E(B - V)(l, b) \tag{3.3}$$

[1]The NASA/IPAC Extragalactic Database (NED) is operated by the Jet Propulsion Laboratory, California Institute of Technology, under contract with the National Aeronautics and Space Administration.

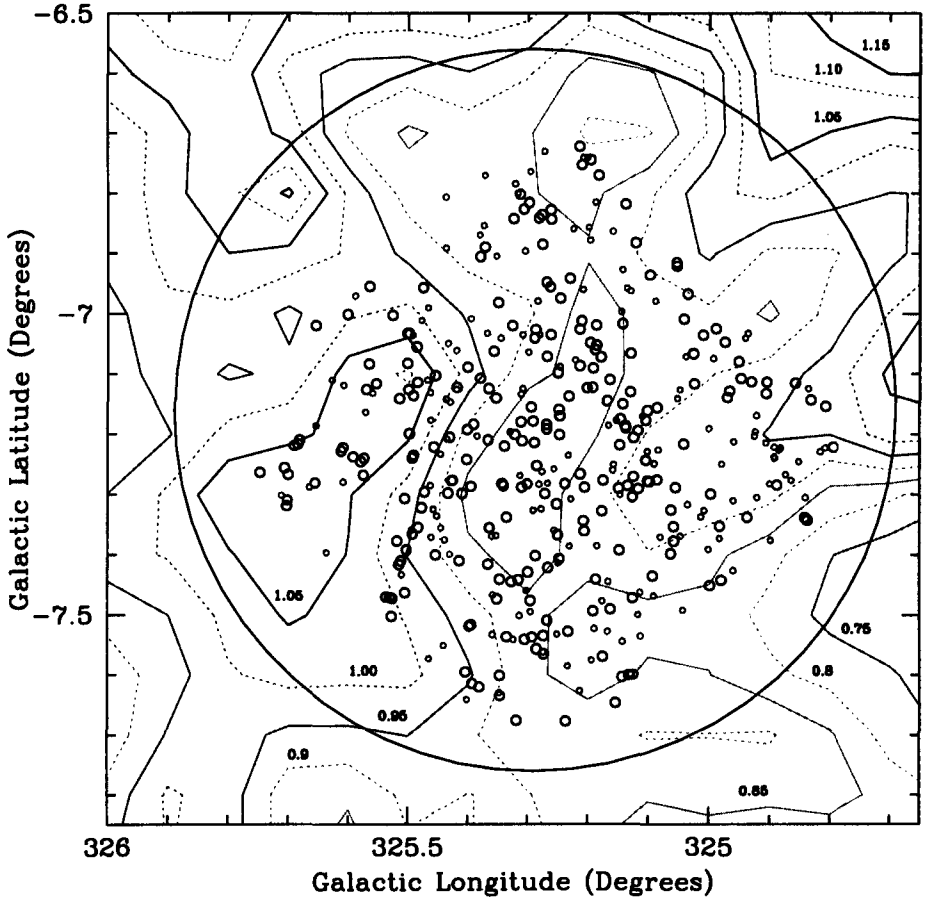

Figure 3.1: The distribution of galaxies identified in the K_s-band images, in Galactic coordinates. Galaxies are marked with large circles, while candidates are shown as small circles. The contours of Galactic extinction as determined from the dust maps of Schlegel et al. (1998) and the corresponding values of B-band extinction are shown, in magnitudes. The central region of the Norma cluster is demarcated by the solid circle with a radius of $\frac{1}{3}$ Abell radius (0.6°).

For comparison, the extinction in the B-band is given by $A_B = 4.14E(B-V)$. The value of A_{K_s} for each galaxy is given in Column 5 of the catalogue in Appendix A. The absolute magnitude of each galaxy is then calculated using Equation 3.2. Magnitudes corrected for extinction are indicated with a superscript "0" in the remainder of this thesis (e.g K_s^0).

The contours of Galactic extinction determined from the IRAS/DIRBE maps and the distribution of objects, in Galactic coordinates, are shown in Fig. 3.1. Likely galaxies are marked with large circles, while candidate galaxies are shown as small circles. The extinction contours are labelled with the B-band extinction. The corresponding K_s-band extinction correction is 9% of that in the B-band, as shown above.

3.1.3 Spatial Distribution of Galaxies

The galaxies are centrally concentrated, as shown in the distributions in Fig. 3.1 and 3.2. Fig. 3.2 shows the positions of the galaxies found in this survey, in equatorial coordinates, as well as the galaxies identified in the deep optical search of Woudt & Kraan-Korteweg (2001) using IIIaJ film copies of the SRC sky survey. Of the 106 optically identified objects in this region, only 5 were not detected in the K_s-band (see Section 3.1.5).

The density distribution is shown in a low-resolution contour plot in Fig. 3.3. Each contour represents an increase in density of 150 galaxies per square degree. The density increases smoothly towards the centre and there is no strong subclustering within the region surveyed, approximately covering the area within 1/3 Abell radius. The contours are almost spherical. The *ROSAT* PSPC image of the cluster (Fig. 1; Böhringer et al. 1996), covering approximately the same region, shows more elongated contours of X-ray emission and provides evidence for an ongoing merger with a smaller subcluster approximately $9'$ from the central cD galaxy, WKK6269.

The filled circle in Fig. 3.3 represents the centre of the cluster, as given by NED, while the cross represents the position of WKK6269. The offset of WKK6269 from the centre of the density distribution is interesting, particularly since its peculiar velocity is unusually large compared to the velocity centroid of the cluster ($v_{pec} = 588 \pm 80$ km s^{-1}; Woudt 1998). This provides further evidence that the cluster is not relaxed and may support a merger scenario.

3.1.4 Sample Completeness

The completeness limit was estimated using the method described in (Garilli, Maccagni & Andreon 1999) and Andreon, Cuillandre & Pelló (2000). Galaxies begin to be lost when their central surface brightness drops below the detection threshold at a particular magnitude. The relationship between maximum surface brightness, given by SExtr, and the magnitude within a 5 arcsecond aperture is shown in Fig. 3.4. In this figure galaxies

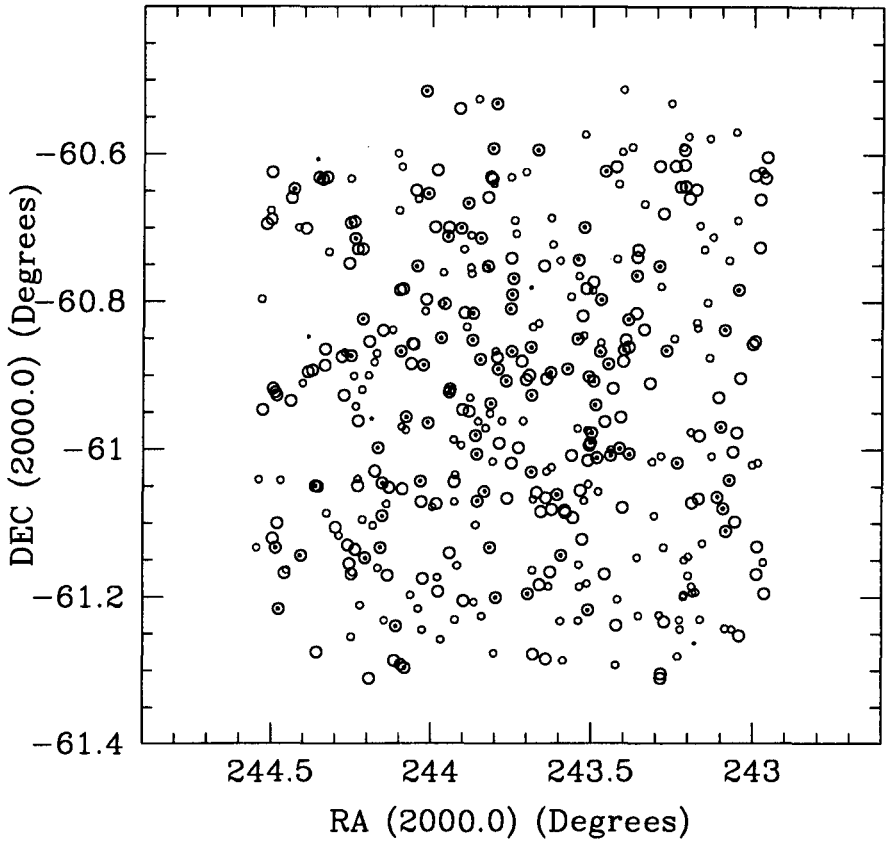

Figure 3.2: The distribution of galaxies in equatorial coordinates. Galaxies identified in the K_s-band images are marked with large open circles, while candidates are shown as small open circles. Galaxies identified on the IIIaJ film copies of the SRC sky survey by Woudt & Kraan-Korteweg (2001) are shown as small filled circles.

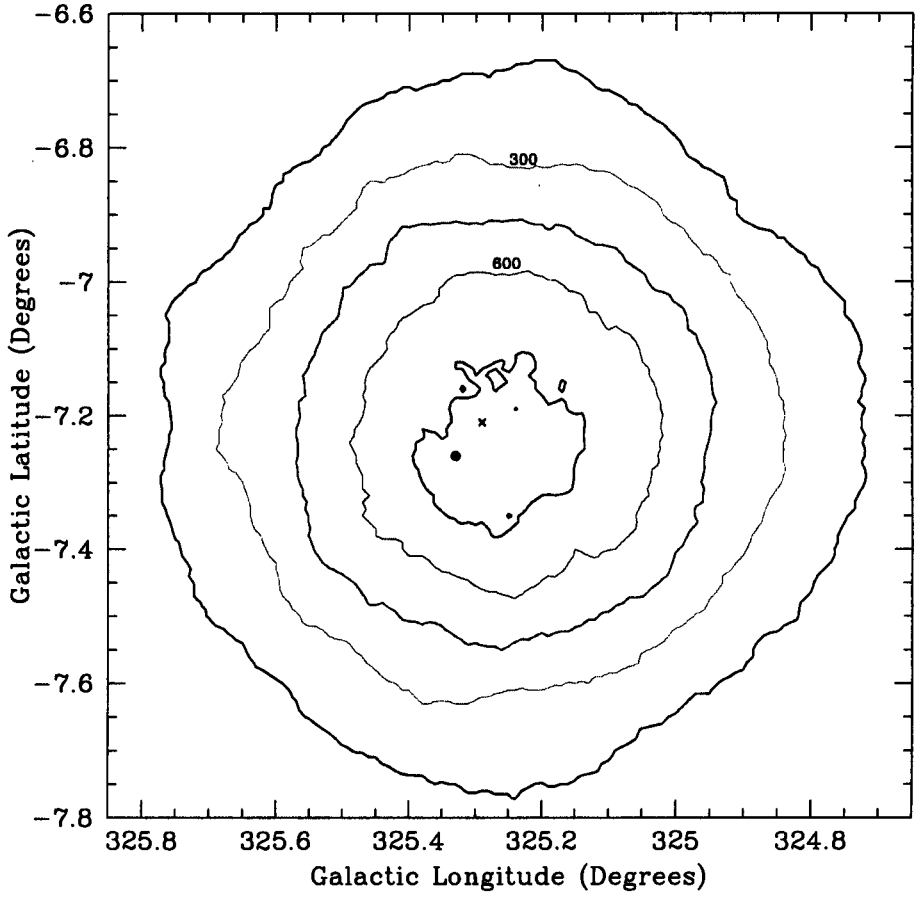

Figure 3.3: A low-resolution contour plot of the spatial distribution of objects (galaxies and candidates) identified in the K_s-band images. The density contours are labelled with the number of galaxies per square degree. The filled circle represents the centre of the cluster, as given by NED, while the cross represents the position of the central cD galaxy (WKK6269).

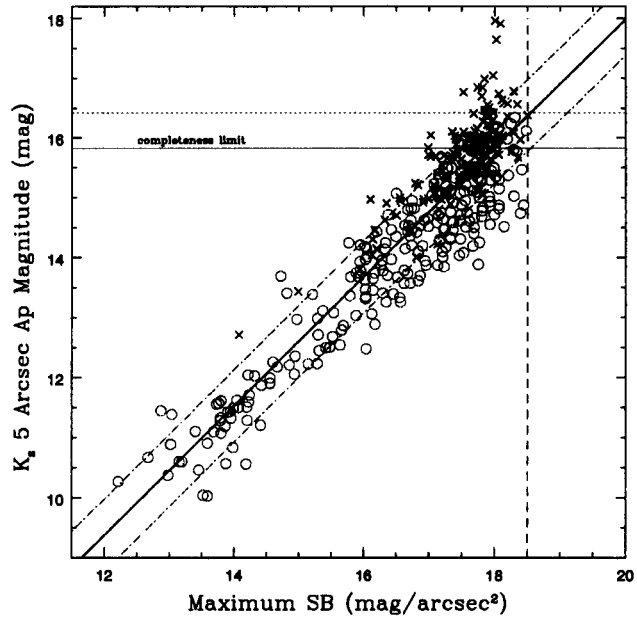

Figure 3.4: Surface brightness vs. magnitude in a 5 arcsecond aperture. The fitted relation is indicated by the thick solid line, with the dash-dot lines representing a deviation of 1σ on either side. The completeness magnitude is indicated by the solid line. Reliable galaxies are shown as open circles and candidates as crosses.

are indicated by open circles, while candidate galaxies are shown as crosses. The thick solid line is a linear fit to all the objects ($+1\sigma$ and -1σ are shown as dash-dot lines). The dashed line indicates the surface brightness detection limit. Galaxies to the right of the surface brightness limit, yet below the dotted line (the intercept between the surface brightness limit and the fitted relation) are not detected. The completeness limit is thus given by the solid line, at the magnitude where the surface brightness limit intersects with the -1σ relation, rather than with the dotted line.

The completeness limit determined in this way is $K_s = 15.^{\rm m}82$ using 5 arcsecond aperture magnitudes. The slope of the relationship between surface brightness and magnitude changes slightly and has smaller scatter if the candidate galaxies are excluded from the fit. This results in a completeness limit of $K_s = 15.^{\rm m}37$. The completeness limits for a range of magnitude types are shown in Table 3.1.

Histograms of the number of galaxies and candidates in magnitude bins of $0.^{\rm m}5$ are shown in Fig. 3.5 for the Kron and 5 arcsecond aperture magnitudes. The completeness limit for all objects is indicated by the dashed line in each case. It is clear that the number of objects reliably identified as galaxies begins to drop off for magnitudes beyond

Table 3.1: Completeness limits using different magnitude types

Magnitude Type	Completeness limit [mag]	
	All objects	Excl. Candidates
5″ Ap	15.82	15.37
7″ Ap	15.58	15.12
10″ Ap	15.34	14.91
15″ Ap	14.88	14.61
Iso	16.85	16.30
Kron	15.74	15.10

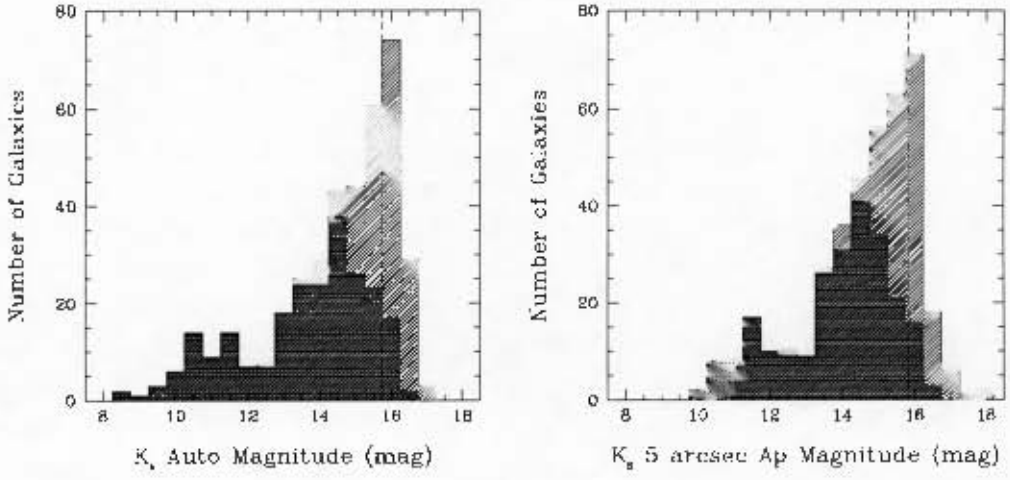

Figure 3.5: Histograms of the galaxy (dark shading) and candidate (diagonal shading) distribution with auto magnitudes (left) and 5 arcsecond aperture magnitudes (right). The completeness limits determined for all objects are shown as dashed lines in each case.

the $K_s = 14.^m5$ bin, although the total number of objects increases to approximately $K_s = 16$ mag. For Kron magnitudes, the galaxy completeness limit is $15.^m10$, thus a bin with a width of $0.^m5$ centered at $15.^m00$ would not be complete. We thus adopt $K_s = 14.^m75$ as the completeness limit for the determination of the LF; this sample consists of 170 galaxies. When candidates are included the LF can be extended by approximately half a magnitude. The complete sample then consists of 231 objects, 196 galaxies and 35 candidates.

3.1.5 Comparison with Optical Data

Counterparts for 101 of the 235 (43%) of the galaxies in our catalogue have counterparts in the catalogue obtained from the deep optical search by Woudt & Kraan-Korteweg (2001). An additional 89 galaxies (38%) were previously identified on deep R_C-band images of the Norma cluster taken with the Wide Field Imager on the MPG/ESO 2.2-m telescope (Woudt 2006, private communication). Velocity information is available for 102 galaxies (43% of the total galaxy sample), many of which have been observed in a follow-up survey with 2dF (Woudt et al. 2007, in preparation). The distribution of galaxies with B_J magnitudes (as given in column 10 of the catalogue in Appendix A) as well as galaxies identified in the K_s-band in equatorial coordinates is shown in Fig. 3.2. The distribution of velocities as a function of distance to the central galaxy (WKK6269) is shown in Fig. 3.6. Galaxies with velocities greater than 8000 km s^{-1} are assumed to be background galaxies. The mean velocity of cluster galaxies is 4816 km s^{-1} with a dispersion of 978 km s^{-1}.

The extinction-corrected $B_J^0 - K_s^0$ colour vs. magnitude for the galaxies with photometric information in both bands is shown in Fig. 3.7. Note however, that the B_J-band magnitude is an isophotal magnitude, corresponding approximately to the flux measured within the 25 mag/arcsec^2 isophote (B_{25}), whereas the K_s-band Auto (or Kron) magnitude is an estimate of the total magnitude. B_{25} magnitudes are ~ 0.2 mag fainter than total B magnitudes, depending on the type of galaxy (Doi et al. 1995). The apparent colour of galaxies depends on their intrinsic properties such as morphological type and dust content, as well as redshift and reddening along the line of sight (McCall 2004). The mean extinction-corrected $B_J^0 - K_s^0$ colour in the range $8 \leq K_s^0 \leq 13$ mag is 3.9 mag, however the scatter is large ($\sigma = 0.6$ mag). The York Extinction Solver[2] (YES) gives a k-correction in $B - K_s$ of 0.12 mag for elliptical galaxies. Subtracting 0.12 mag to account for the k-corrections and 0.2 mag to convert to total B magnitude, gives a colour of 3.6 mag. This corresponds to the intrinsic colour of early type spiral galaxies given by YES, however it is not inconsistent with $B - K_s = 3.85$ mag calculated by YES for ellipticals and $B - K_s \sim 4$ mag for early-type galaxies from Jarrett et al. (2003), given the high uncertainty in the B-band extinction, which may lead to an over-estimate of the correc-

[2]The York Extinction Solver (YES) is available at http://www2.cadc-ccda.hia-iha.nrc-cnrc.gc.ca/community/YorkExtinctionSolver/. See McCall 2004 for more information.

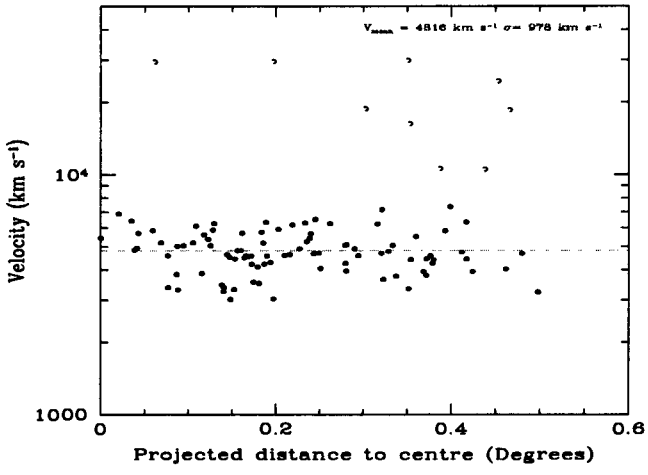

Figure 3.6: The observed radial velocities as a function of distance from the central galaxy (WKK6269). Galaxies with velocities less than 8000 km s^{-1} (filled circles) are assumed to be members of the cluster. Those with velocities greater than 8000 km s^{-1} are shown as open circles. The mean velocity of the cluster galaxies is shown as a dashed line.

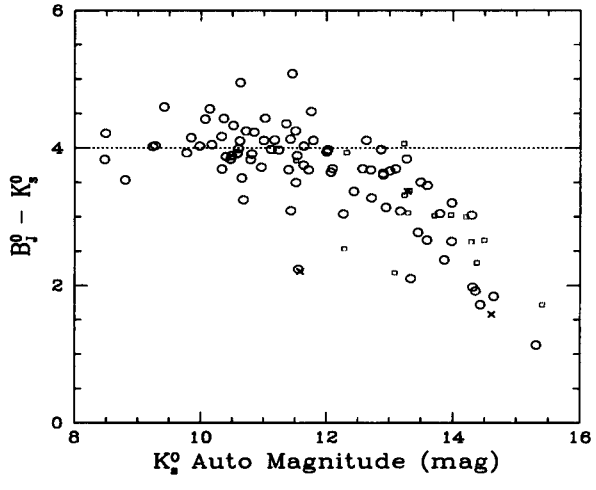

Figure 3.7: The colour-magnitude distribution of galaxies with counterparts in the Woudt & Kraan-Korteweg (2001) catalogue. Magnitudes in both B_J and K_s have been corrected for extinction. The dotted line indicates the expected colour of early type galaxies (Jarrett et al. 2003). Spectroscopic members of the cluster are shown as open circles, non-members as crosses and galaxies with no velocity information as open squares.

Table 3.2: B_J-band galaxies not detected in the K_s-band

WKK ID	B_J [mag]	A_B [mag]	A_K [mag]	Approx. K_s [mag]
WKK6369[a]	16.5	0.855	0.075	13.7
WKK6255	17.2	0.976	0.086	14.3
WKK6141	17.4	0.829	0.073	14.6
WKK6408	18.4	1.04	0.091	15.5
WKK6410	18.9	1.04	0.092	16.0

[a]Covered by a saturated star in the K_s-band image

tion, as well as the scatter of ~ 0.5 mag in B_J. Fainter galaxies are found to be bluer, suggesting that more of them are late-type galaxies; compare for instance Fig. 3.7 with Fig. 19 of Jarrett et al. (2003). In Fig. 3.7 galaxies with velocities less than 8000 km s^{-1} (open circles) are assumed to be members of the cluster, while those with greater velocities (crosses in Fig. 3.7) are assumed to be background galaxies (see Fig. 3.6). Galaxies with no velocity information are shown as open squares.

Five galaxies identified on the IIIaJ film copies of the SRC sky survey by Woudt & Kraan-Korteweg (2001) were not detected in the K_s-band. The B_J-band magnitudes and extinctions of these galaxies are given in Table 3.2, along with the estimated K_s-band magnitudes they would have if they are assumed to be late-type galaxies with a colour of $B_J^0 - K_s^0 \sim 2$. The brightest galaxy (WKK6369) can be seen on two of the fields, however it is partially obscured by a saturated star and thus was not detected by SExtr. WKK6255, WKK6141 and WKK6408 were all identified by eye as low surface brightness galaxies but not extracted by SExtr, while the faintest galaxy (WKK6410) was difficult to identify by eye. In the case of WKK6255, a comparison with the original image showed that a star was removed very close to the galaxy. These results suggest that the detection of low surface brightness galaxies may be influenced by star-subtraction and that the completeness is lower than expected from the surface brightness-magnitude relation, however these 5 galaxies amount to less than 5% of the sample of galaxies with B_J-band magnitudes in the region.

3.2 The K_s-Band Luminosity Function

3.2.1 Derivation of the Luminosity Function

The LF is derived by binning the galaxy number counts in bins of 0.5 mag after correcting for background counts. The magnitudes of each galaxy are corrected for extinction before

binning, as discussed in Section 3.1.2. No correction is made for stellar confusion because the majority of stars have already been removed during the star subtraction process. The number of objects that are misclassified as galaxies is also reduced by classifying all the objects by eye. Uncertain cases are labelled as candidates, thus the LF determined for certain galaxies can be seen as a lower limit.

Cluster Membership

The largest source of uncertainty in the determination of the LF is correcting for the number of background galaxies. Spectroscopic information is available for 99 of the 170 K_s-band galaxies brighter than the completenesss limit (58%). Mobasher et al. (2003) developed a method for correcting a large spectroscopic survey in the Coma cluster for incompleteness and determined the R-band LF. Although the number counts are lower in this case, we will follow the same approach.

Let the number of galaxies in the area covered by the K_s-band survey with spectroscopic information be $N_s(m)$, in a given range of apparent magnitude. None of the galaxies in the spectroscopic sample have velocity $\lesssim$ 2000 km s^{-1}, which would place them as foreground galaxies. All galaxies with velocities less than 8000 km s^{-1} are thus assumed to be members of the cluster (see Fig. 3.6). Let the number of galaxies that are members and non-members of the cluster be $N_m(m)$ and $N_{nm}(m)$ respectively. The fraction of galaxies satisfying the membership criterion in each magnitude bin is then

$$f(m) = \frac{N_m(m)}{N_m(m) + N_{nm}(m)} = \frac{N_m(m)}{N_s(m)}.$$

The membership fraction, presented in Table 3.3 and Fig. 3.8, gives the probability that a random galaxy drawn from the spectroscopic sample will be a member of the cluster, as a function of magnitude. The error in the membership fraction, shown in brackets in Table 3.3, is determined using Poisson statistics, following Mobasher et al. (2003). The number of members $N_m(m)$ is a binomial random variable, since it is the number of successes (members) in a fixed number of trials (number of objects with spectroscopic data), with the probability of a galaxy being a member given by $f(m)$.

The Luminosity Function

The number counts in each magnitude bin in the K_s-band photometric sample ($N_p(m)$) and spectroscopic sample ($N_s(m)$) are shown as a histogram in Fig. 3.9, where the darkest shading refers to members of the cluster, as defined above, the cross-hatched area to non-members, the diagonal shading to galaxies without spectroscopic information and the open histogram the total number of objects in the photometric sample, including candidate galaxies. If the spectroscopic sample reflects the proportions of members and non-members that can be expected in the full photometric sample, the number of galaxies

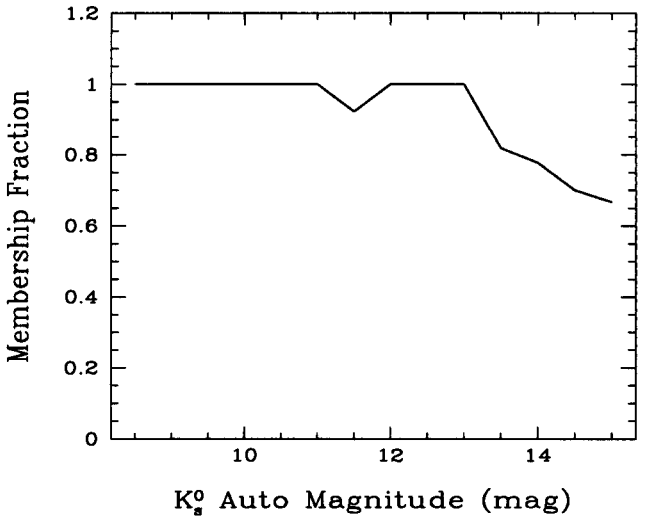

Figure 3.8: The membership fraction of the spectroscopic sample as a function of extinction-corrected Auto magnitude. Galaxies with velocities less than 8000 km s^{-1} are assumed to be members of the cluster.

Table 3.3: Spectroscopic number counts and the membership fraction in K_s-band magnitude intervals

K_s^0 [mag]	$N_s(m)$	$N_m(m)$	$f(m)$
8.50	2.00	2.00	1.00 (0.71)
9.00	2.00	2.00	1.00 (0.71)
9.50	2.00	2.00	1.00 (0.71)
10.00	7.00	7.00	1.00 (0.38)
10.50	14.00	14.00	1.00 (0.27)
11.00	9.00	9.00	1.00 (0.33)
11.50	13.00	12.00	0.92 (0.08)
12.00	6.00	6.00	1.00 (0.41)
12.50	6.00	6.00	1.00 (0.41)
13.00	8.00	8.00	1.00 (0.35)
13.50	11.00	9.00	0.82 (0.14)
14.00	9.00	7.00	0.78 (0.18)
14.50	10.00	7.00	0.70 (0.21)
15.00	2.00	1.00	0.50 (0.71)

NOTE.–Errors for the membership fraction are given in parentheses.

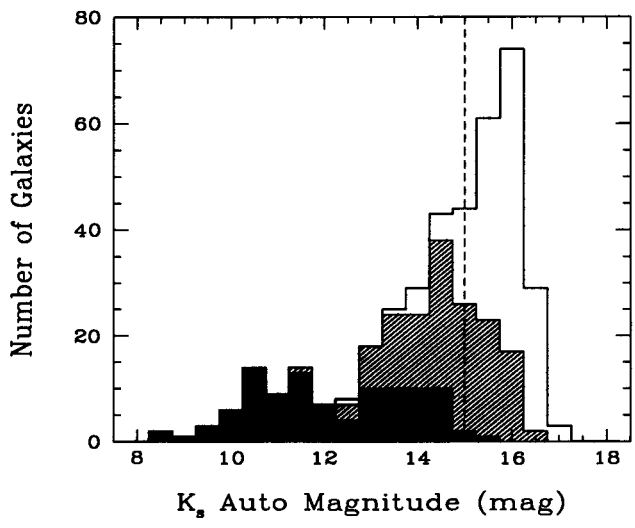

Figure 3.9: The number counts in half-magnitude bins. Galaxies with velocities less than 8000 km s^{-1} are assumed to be members of the cluster, shown as the darkest shading. Non-members have the second darkest shading, galaxies with no spectroscopic information have diagonal shading and the remaining region represents candidate galaxies.

without velocity information that are cluster members can be estimated as $f(m)N_{nv}(m)$, where $N_{nv}(m)$ is the number of galaxies without velocity information, in a given range of apparent magnitude.

The LF can then be estimated as

$$\phi(m) = \frac{1}{A}(N_m(m) + f(m)N_{nv}(m)) = \frac{N_p(m)}{A}f(m), \tag{3.4}$$

where A is the area of the survey (Mobasher et al. 2003). The error in the LF is given by

$$\frac{\delta\phi(m)}{\phi(m)} = [\frac{1}{N_p(m)} + \frac{1}{N_m(m)} - \frac{1}{N_s(m)}]^{1/2}. \tag{3.5}$$

This reduces to $1/\sqrt{N_m(m)}$ if all the galaxies in the photometric sample have spectroscopic data and $1/\sqrt{N_p(m)}$ if all the galaxies in the spectroscopic sample at magnitude m are members of the cluster. The number counts and corresponding LF are shown in Table 3.4. The left-hand column includes all the objects, while the right-hand column excludes objects classified as candidate galaxies.

3.2.2 The Shape of the Luminosity Function

The LF determined above is plotted in Fig. 3.10. The circular data points represent the LF obtained from the total number counts (left-hand column of Table 3.4). The triangular

Table 3.4: The total number counts and resultant LF

	All objects			Excluding candidates		
K_s [mag]	$N_p(m)$	$N_p(m)f(m)$	$\phi(m)$ [mag^{-1}Mpc^{-2}]	$N_p(m)$	$N_p(m)f(m)$	$\phi(m)$ [mag^{-1}Mpc^{-2}]
8.50.....	2.00	2.00	2.50 (1.77)	2.00	2.00	2.50(1.77)
9.00.....	2.00	2.00	2.50 (1.77)	2.00	2.00	2.50(1.77)
9.50.....	2.00	2.00	2.50 (1.77)	2.00	2.00	2.50(1.77)
10.00.....	7.00	7.00	8.75 (3.31)	7.00	7.00	8.75(3.31)
10.50.....	14.00	14.00	17.50 (4.68)	14.00	14.00	17.50(4.68)
11.00.....	9.00	9.00	11.25 (3.75)	9.00	9.00	11.25(3.75)
11.50.....	14.00	12.92	16.15 (4.51)	14.00	12.92	16.15(4.51)
12.00.....	6.00	6.00	7.50 (3.06)	6.00	6.00	7.50(3.06)
12.50.....	10.00	10.00	12.50 (3.95)	9.00	10.00	11.25(3.75)
13.00.....	19.00	19.00	23.75 (5.45)	19.00	19.00	23.75(5.45)
13.50.....	27.00	22.09	27.61 (6.61)	24.00	22.09	24.55(6.11)
14.00.....	28.00	21.78	27.22 (7.07)	25.00	21.78	24.31(6.51)
14.50.....	44.00	30.80	38.50 (9.86)	37.00	30.80	32.38(8.56)
15.00.....	47.00	23.50	29.38 (21.21)	...	...	...

NOTE.–Errors for the LF are given in parentheses.

data points represent the number counts of objects classified as definite or likely galaxies only (candidates excluded), as given in the right-hand column of Table 3.4. The two LFs are very similar over the entire magnitude range considered, deviating slightly for $K \gtrsim 13.^{\rm m}5$. The LF is flat for the three brightest bins, increasing thereafter. There is a shallow dip at $K = 12^{\rm m}$, corresponding to an absolute magnitude of $M_{K_s} = -22.^{\rm m}18$. This is approximately at the transition between dwarf and giant galaxies and arises due to the relative contributions of the type-specific LFs. Apparent magnitudes are transformed to absolute magnitudes using a distance modulus of $34.^{\rm m}18$, calculated in Section 3.1.2.

The LF can be fitted with a Schechter function (Schechter 1976) of the form

$$\phi(M)dM = \phi^* 10^{0.4(\alpha+1)(M^*-M)} e^{-10^{0.4(M^*-M)}} dM \tag{3.6}$$

as described in Section 1.4. The characteristic magnitude, M^*, faint-end slope, α, and normalisation, ϕ^*, were found using a nonlinear least-squares Marquardt-Levenberg algorithm implemented in Gnuplot[3]. The resulting parameters are shown in Table 3.5 and the Schechter functions including and excluding candidates are plotted with the data in Fig. 3.10.

The effects of removing one or more data points from the fit are shown in Table 3.5 and Fig. 3.11. The Schechter parameters were found to be robust to changes in the

[3]Gnuplot is an interactive plotting program, available from http://www.gnuplot.info/.

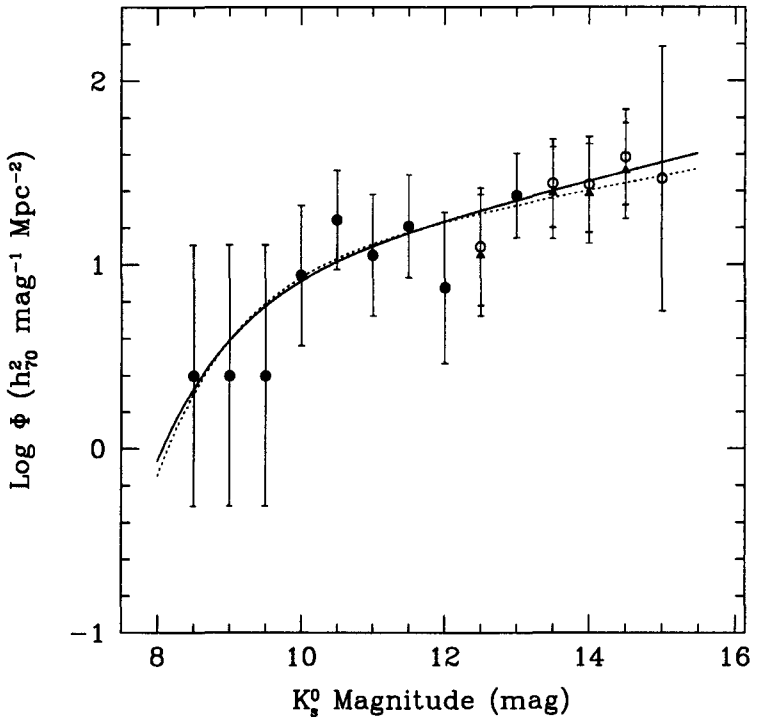

Figure 3.10: The LF of the Norma cluster in the K_s-band (see text for details). Data points and error bars are from Table 3.4: Open circles represent the LF including all objects, while the triangles exclude candidate galaxies. The solid line is the best fit Schechter function for all objects, while the dotted line is the best fit Schechter function excluding candidate galaxies.

Table 3.5: Resulting Schechter parameters from fits to the observed LF

Data fitted	$M^*_{K_s} - 5\log h_{70}$ [mag]	α	ϕ^* [h^2_{70}Mpc^{-2}]	χ^2	ν	P($\chi^2|\nu$) [%]
Including candidates						
All bins.....	-25.36 ± 0.74	-1.25 ± 0.10	8.74 ± 2.01	2.42	11	99.6
Exclude $K > 13.^m75$.....	-25.18 ± 0.80	-1.20 ± 0.16	10.53 ± 3.02	2.27	8	97.1
Exclude $K > 14.^m25$.....	-25.21 ± 0.73	-1.21 ± 0.13	10.20 ± 2.55	2.28	9	98.6
Exclude $K > 14.^m75$.....	-25.39 ± 0.80	-1.26 ± 0.10	8.51 ± 2.14	2.41	10	99.2
Dip point flagged.....	-25.03 ± 0.40	-1.20 ± 0.07	12.22 ± 1.8	1.06	9	99.9
Exclude $K = 8.^m5$.....	-25.05 ± 0.95	-1.23 ± 0.12	10.36 ± 2.91	2.39	10	99.2
Exclude $K = 8.^m5$ & dip	-24.52 ± 0.42	-1.15 ± 0.08	16.69 ± 2.55	0.90	8	99.9
Excluding candidates						
All bins.....	-25.24 ± 0.63	-1.19 ± 0.10	9.97 ± 2.19	2.40	10	99.2

completeness limit. Similar values (within 1σ of the fit to all the data) were obtained for all three parameters, using limiting values from $K = 13.^m75$ (excluding the last 3 bins) to $K = 15.^m25$ (including all bins). The fit improved slightly by flagging the dip point (bins $K = 12^m$ and $K = 12.^m5$), however the characteristic magnitude and faint end slope remain within 1σ of the parameters obtained by fitting all the data. The uncertainty on the parameters is approximately halved. In some clusters, the fit to a Schechter function is improved by excluding the brightest cD galaxy from the fit (Binggeli, Sandage & Tammann 1988). In this case, excluding the brightest bin, which contains the two cD galaxies, produces a slightly fainter characteristic magnitude but does not significantly change the results. The most dramatic change occurs when both the dip point and the brightest bin are excluded. The normalisation increases by more than 3σ and the characteristic magnitude is fainter by more than 1σ. χ^2 is lowest for this fit, which is termed "best fit" in the comparisons to other LF below. The χ^2 parameter, number of degrees of freedom, ν, and goodness-of-fit probability, P($\chi^2|\nu$), for each fit are listed in Table 3.5. The high probabilities obtained in each case indicate that the Schechter function is a reasonable form to assume for the cluster LF.

3.2.3 Comparisons to Other Luminosity Functions

The derived LF of the Norma cluster in the K_s-band is comparable in form to the LFs of other clusters and the field LF. The shape of the LF, including the dip at the transition between giant and dwarf galaxies ($M_{K_s} \sim 22$ mag), is similar to the observed LFs of other rich clusters. In this section, the LF is compared quantitatively with those of the nearby clusters, such as Coma, Virgo and Centaurus, a more distant cluster, A118, and the field.

The Schechter parameters fitted to the Norma cluster LF data can be directly compared

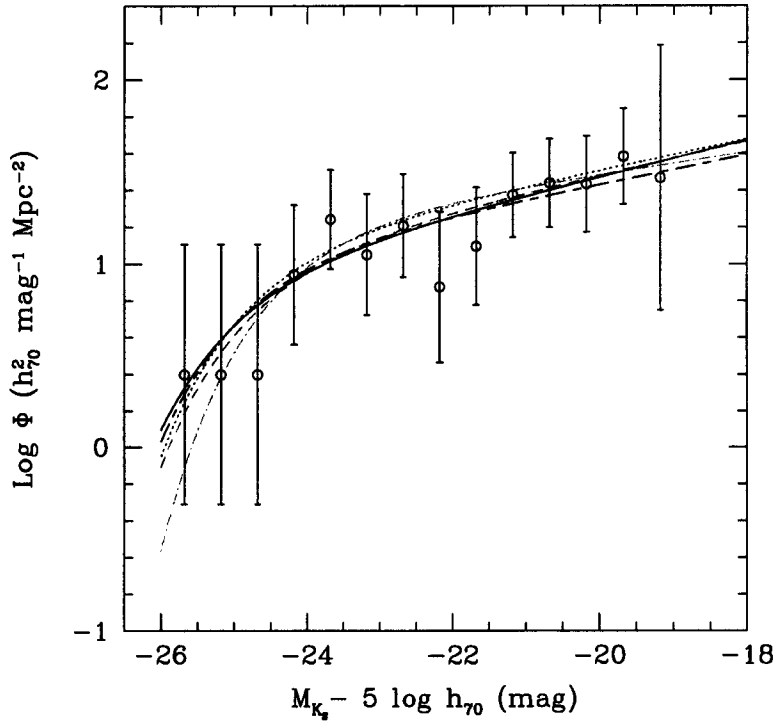

Figure 3.11: The LF of the Norma cluster in the K_s-band, in terms of absolute magnitude (see text for details). Data points and error bars represent the LF for all objects, including candidates. The solid line is the best fit Schechter function, including all data points. The long-dash line is the fit to $M_{K_s} = -20^{\rm m}.43$ ($K = 13.^{\rm m}75$). The dotted line excludes the dip point at $M_{K_s} \approx -22$. The dashed line excludes the brightest bin. The dash-dot line excludes the dip point and brightest bin.

Table 3.6: Resulting Schechter parameters from fits to the observed LF, with various adopted fixed faint end slopes

	All Bins		"Best Fit"[a]	
α	$M^*_{K_s} - 5\log h_{70}$ [mag]	ϕ^* [h^2_{70}Mpc^{-2}]	$M^*_{K_s} - 5\log h_{70}$ [mag]	ϕ^* [h^2_{70}Mpc^{-2}]
-0.98	-24.40 ± 0.25	24.50 ± 1.39	-23.99 ± 0.17	29.48 ± 1.25
-1.00	-24.45 ± 0.26	23.07 ± 1.29	-24.04 ± 0.17	27.82 ± 1.16
-1.16	-24.94 ± 0.33	13.18 ± 0.78	-24.57 ± 0.24	16.03 ± 0.73
-1.20	-25.11 ± 0.38	11.11 ± 0.72	-24.75 ± 0.29	13.50 ± 0.70
-1.30	-25.69 ± 0.65	6.56 ± 0.70	-25.43 ± 0.62	7.80 ± 0.80

[a]Excludes $K = 8.^m5$ & dip

to those of other LFs. The comparison is not straight forward, however, due to differences in wavelength band, magnitude system, area covered by the survey, depth of the survey, region within the cluster etc. All magnitudes from the literature used in the comparison have been converted to $H_0 = 70h_{70}$ km s^{-1} Mpc^{-1}.

The characteristic magnitude for the Coma cluster found by De Propris et al. (1998) in the K-band ($M^*_K = -24.^m02$) and Andreon & Pelló (2000) in the H-band ($M^*_H = -23.^m86$) agree well, taking into account the colour difference $H - K \approx 0.^m22$ (De Propris et al. 1998). No errors for M^* are quoted in De Propris et al. (1998), however the 1σ error ellipse shown in their Fig. 2 indicates that $1\sigma \sim 0.^m75$. The confidence interval for the LF fit of Andreon & Pelló (2000) is even larger (their Fig. 3). De Propris et al. (1998) claim that their characteristic magnitude agrees well with the field LF determined by Gardner et al. (1997) and the B-band LF of Virgo (Sandage, Binggeli & Tammann 1985), with $B - H \approx 4.^m2$. The characteristic magnitude of $M^*_{K_s} = -25.36 \pm 0.74$ mag for the Norma cluster is brighter than for Coma, comparing the parameters at face value. Excluding the dip point and brightest bin, the characteristic magnitude of the Norma cluster is $M^*_{K_s} = -24.52 \pm 0.42$ mag, within 1σ of the De Propris et al. (1998) determination.

There is some degeneracy between the Schechter parameters, thus a further comparison can be made by fixing the faint-end slope and re-fitting M^* and ϕ^*. The results for various fixed values of α are shown in Table 3.6 for fits to all the data and the "best fit" case, where the brightest bin and dip points are excluded. The values of α have been chosen to match a selection of those in the literature. The results indicate that M^* is fainter and ϕ^* higher for flatter faint-end slopes. For $\alpha = -0.98$, corresponding to the slope measured by De Propris et al. (1998) for the bright end of the LF, M^* agrees well with their characteristic magnitude. For all choices of $\alpha > -1.20$, M^* is within 1σ of the De

Propris et al. (1998) and Andreon & Pelló (2000) values, in both the fits. A steeper faint slope of $\alpha = -1.30$, however, produces an even brighter M^* which does not agree with previous determinations. The parameters are not well constrained for more negative values of α. Andreon & Pelló (2000) find a deep dip in the H-band LF of the Coma cluster. The position of the dip at $H \sim -22$ mag agrees with the position of the dip found in this study, however the amplitude of the dip in the Coma LF is much larger - ϕ at the dip point is the same as in the brightest bin.

The shape of the K_s-band LF of the Norma cluster is consistent with the optical B- and R-band LFs of the Coma cluster determined by Mobasher et al. (2003). Mobasher et al. (2003) survey a larger area (1 deg^2) but the magnitude range is approximately the same as in this work, shifted by $(R-K) \sim 2.^{\rm m}5$. A shallow dip is found in both B- and R-band LFs at $M_R = -19.^{\rm m}5$, which corresponds to the position of the dip at $K_s = -22^{\rm m}$, again shifted by a mean colour of $R-K \sim 2.^{\rm m}5$. This suggests that the dip is not caused by an increase in star formation at the bright end due to the hostile cluster environment, since the NIR is less affected by short bursts of star formation (see Andreon & Pelló 2000 and references therein). The most likely explanation for the dip is that the morphological mix of galaxies leads to a decrease in number counts at the transition between giant and dwarf galaxies. The Schechter parameters in the R-band are $M_R^* = -21.^{\rm m}62$ and $\alpha = -1.18$, while in the B-band, $M_B^* = -19.^{\rm m}78$ and $\alpha = -0.96$. The slope and characteristic magnitude in R are consistent with the "best fit" K_s-band parameters. The B-band slope is shallower and M_B^* fainter, however Mobasher et al. (2003) state that their M_B^* is approximately 1 mag fainter than those determined for a sample of nearby ($z < 0.11$; De Propris et al. 2002) and intermediate redshift clusters ($z \sim 0.3$; Valotto et al. 1997).

A number of authors have found a steep faint-end slope for Coma, in the optical (e.g. Secker & Harris 1996, Trentham & Mobasher 1998) and NIR (e.g. Mobasher & Trentham 1998, De Propris et al. 1998). Most of these studies use statistical background subtraction and extend to fainter magnitudes, thus an upturn in the LF may only occur for fainter magnitudes than are considered here. De Propris et al. (1998) find an upturn in the slope for $M^* + 3$ mag, well within the limits of this survey, however. It is possible that a Gaussian or Schechter function fitted to the bright end with a power-law fitted to the faint end is an equally valid assumption of the form of the LF. There has also been a suggestion that the slope in the central region of clusters may be shallower than in the outskirts (e.g. Lobo et al. 1997), with evidence for this in Coma (Andreon & Pelló 2000) and A118 (Andreon 2001). A similar analysis using fields offset from the center would be necessary to confirm whether this is the case for the Norma cluster.

Jerjen & Tammann (1997) compared the B_T-band LFs of Centaurus, Virgo and Fornax within an area of 2.4 core radii. For the Norma cluster, the core radius is 0.17° (Kraan-Korteweg et al. 1996), thus the corresponding area is 0.5 square degrees, slightly smaller than the area used for this determination of the LF (0.6 square degrees). The Schechter

parameters of Centaurus, Virgo and Fornax vary dramatically, depending on the limiting magnitude. Jerjen & Tammann (1997) caution that the parameters determined using only a bright population are unstable and as a result, M^* cannot be used as a distance indicator. M^* is essentially unconstrained for Fornax, due to the large errors. For Centaurus and Virgo, $M^*_{B_T} = -20.22 \pm 0.41$ mag and -21.80 ± 0.60 mag, respectively, down to a limiting magnitude of $M_{B_T} = -15.^{\rm m}3$. The corresponding slopes are -1.18, -1.35 and -1.48 for Centaurus, Virgo and Fornax. Chiboucas & Mateo (2006) constructed the V-band LF of the Centaurus cluster over an area of 0.83 square degrees, using a spectroscopic sample to correct for cluster membership, as well as statistical methods. Using surface-brighteness criteria to correct for the expected number of background galaxies, they found $M^*_V = -21.^{\rm m}22$ and $\alpha = -1.40$, however slopes between -1.22 and -1.50 were consistent with the data. Using a control field to statistically correct for background galaxies, they found $M^*_V = -21.^{\rm m}25$ and $\alpha = -1.40$. The faint-end slopes in both cases are steeper than we find in the K_s-band LF.

The LF of the Norma cluster can be compared to that of A118, a cluster at $z = 0.3$ (Barger et al. 1996, Andreon 2001), by noting that the K_s-band corresponds approximately to the rest-frame H-band at $z = 0.3$. The transformation is

$$M_{H_{z=0}} = M_{K_{z=0.3}} + 0.09 \text{ mag}$$

(Andreon 2001). An offset of ~ 0.22 mag, corresponding to the $H - K$ colour, gives the relation

$$M_{K_{z=0}} \sim M_{K_{z=0.3}} - 0.13 \text{ mag}.$$

A fixed slope of -1.0 yields a characteristic magnitude in agreement with that of Barger et al. (1996) ($M^*_{K'} = -24.^{\rm m}5$), while a slope of -1.2 gives a brighter M^*, corresponding to $M^*_{K_s} = -25.^{\rm m}26$ measured by Andreon (2001). This suggests that there is little evolution in the LF from intermediate redshifts to today.

A recent determination of the field LF (Jones et al. 2006), using the 6-degree Field Galaxy Survey (6dFGS), finds that the Schechter function is not an ideal fit to the LF. The Schechter function is unable to reproduce the flat faint-end slope and drop-off at the bright end simultaneously. Nevertheless, a Schechter function provides a good approximation to the LF. The Schechter parameters obtained in the K_s-band are $M^* = -24.60 \pm 0.03$ mag and $\alpha = -1.16 \pm 0.04$. These results are within 1σ of the fit to all the data and very similar to the "best fit" case, given in Table 3.5, where all the parameters are free to vary. Even better agreement between the characteristic magnitudes are obtained with a fixed slope of -1.16, as shown in Table 3.6. No correction has been made to account for the different types of magnitudes used (Jones et al. 2006 subtract 0.135 mag from M^* of previous 2MASS LFs to convert from Kron to total magnitude). No dip is present in the field LF, which suggests that the cluster environment contains higher numbers of dwarfs than the field. The 6dFGS LF, normalised to fit our data, is shown with the Norma

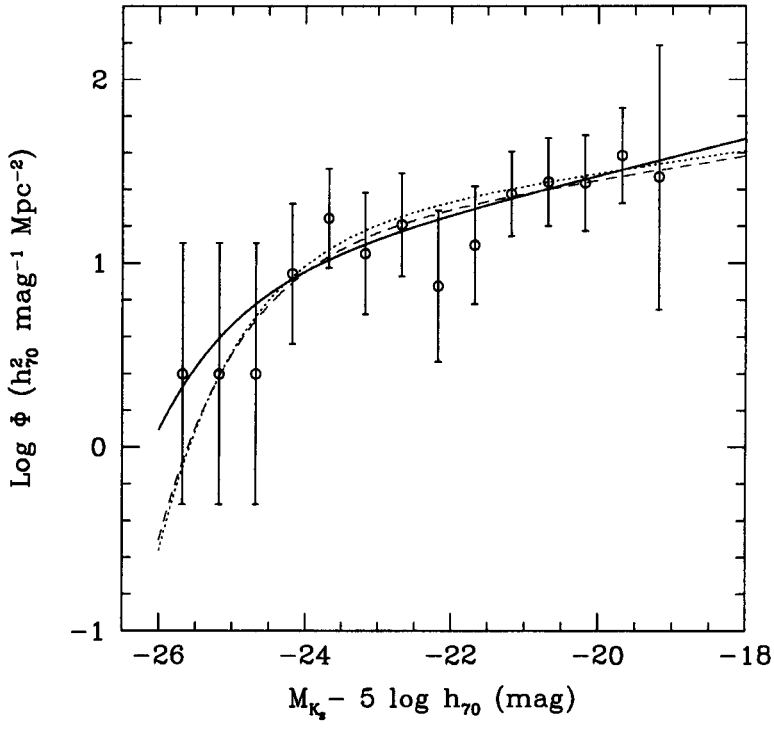

Figure 3.12: The LF of the Norma cluster in the K_s-band, in terms of absolute magnitude (see text for details). Data points and error bars represent the LF for all objects, including candidates. The solid line is the best fit Schechter function, including all data points. The dotted line represents the "best fit", with the brightest bin and the dip point excluded. The dashed line is the field LF determined by Jones et al. (2006), normalised to the data.

cluster LFs in Fig. 3.12. It is somewhat surprising that the agreement with the field LF is so strong, given that the environments are so different. The errors on the cluster LF parameters are much larger than for the field, due to the large number of galaxies used in the field LF determination, and thus the favourable comparison may be fortuitous, rather than supportive of a universal LF.

Chapter 4

Discussion and Conclusions

4.1 Summary of Results

In this thesis, the K_s-band LF of the central $0.8h_{70}^{-2}$ Mpc^2 of the Norma cluster has been determined for $M_{K_s} \lesssim -19$ mag. The Norma cluster is a rich, nearby cluster, comparable to the Coma cluster, yet it has received little attention due to its position near the galactic plane. In this thesis, it has been shown that semi-automated star-subtraction techniques can be effectively used on NIR ZOA data, enabling accurate photometry of galaxies at low latitudes. IRAF routines, encompassing the KILLALL routine of Buta & McCall (1999), were developed and implemented to remove contaminating star-light. The effects of foreground dust were taken into account using the dust maps of Schlegel, Finkbeiner & Davis (1998). The detection and photometry of galaxies was done using SExtractor (Bertin & Arnouts 1996), producing a catalogue containing 390 objects, 235 of which are classified as likely or definite galaxies and 155 as candidate galaxies. The catalogue is presented in Appendix A.

The K_s-band photometry was used to construct the LF of the cluster. The number of background galaxies at each magnitude was estimated from the membership fraction of a smaller spectroscopic sample. The results are summarised as follows:

1. The constructed LF has a similar shape to the NIR LF of other clusters and the field. A Schechter function provides a reasonable fit to the data, with a characteristic magnitude of $M^*_{K_s} = -25.32 \pm 0.74$ mag and faint-end slope of $\alpha = -1.25 \pm 0.10$. There is a shallow dip at $M_{K_s} \sim -22$ mag, where the transition from giant to dwarf galaxies occurs. The presence of the dip in the NIR LF as well as optical LFs suggests that it is not caused by increased star formation at the bright end, but rather arises due to the relative contributions of different galaxy types.

2. The faint-end slope of the LF is flatter than many previous determinations in both the NIR and optical (e.g. Trentham & Mobasher 1998, De Propris et al. 1998). However similar intermediate slopes have been found in optical LFs of Coma (Mobasher

et al. 2003) and Centaurus (Jerjen & Tammann 1997, Chiboucas & Mateo 2006) and NIR LFs of A118 (Barger et al. 1996, Andreon 2001). The limiting magnitude is $M_{K_s} \sim -19$ mag, thus the LF extends to $M^*_{K_s} + 6$, within the dwarf regime.

3. $M^*_{K_s}$ is brighter than found in previous determinations of the NIR LF of the Coma cluster (De Propris et al. 1998, Andreon & Pelló 2000), which may indicate that there is a higher proportion of bright galaxies in the Norma cluster. Fixing α to the value of De Propris et al. (1998) brings the characteristic magnitudes within 1σ of each other, however.

4. The fit to a Schechter function is slightly improved by excluding the brightest bin and dip, though this lacks physical motivation. The resultant parameters are $M^*_{K_s} = -24.48 \pm 0.42$ mag and $\alpha = -1.15 \pm 0.08$.

5. Both the fit to all the data and the improved fit agree with the Schechter parameters found for the field from the 6dFGS (Jones et al. 2006). No dip is present in the field LF, suggesting that the cluster LF has a higher contribution from dwarf galaxies than the field LF.

In this study, the K_s-band LF of the Norma cluster has been determined over a relatively large area, to the depth of dwarf galaxies. This provides an alternative LF for a local rich cluster, which can be compared to the Coma cluster and more distant clusters for evolutionary studies. The error bars on the LF are still large however, and future work should aim to provide better constraints on the LF parameters.

4.2 Future Prospects

There are several possible directions for future work on the LF of the Norma cluster to take. The first possibility is to further constrain the K_s-band LF and determine the K_s-band LF of different cluster regions. The error bars on the LF can be reduced by increasing the number counts. The area used for the LF can be approximately doubled using existing K_s-band images of the outer region. A comparison of the K_s-band LF of the central region, from this study, with outer regions or a larger area encompassing the centre, can be used to investigate trends such as the increase in the faint-end slope of the LF with clustercentric radius and other environmental effects.

The J- and H-bands were simultaneously imaged and the cluster has also been observed in the R_C-band (Woudt 2006, private communication). A similar analysis of these bands, combined with the B_J- and K_s-band photometry discussed in this work, would make photometry of the cluster area available in 5 bands. The automation of the star-subtraction process has already been improved with the development of KILLALL and subsequent IRAF routines, described in this thesis. This can be improved further however, since these

methods are still very time-consuming. The catalogues of objects identified on the K_s-band may be useful as input when using these techniques on the J- and H-band images. The classification of objects as definite galaxies and members of the cluster, based on morphological and surface-brightness criteria, can be improved by utilising the information from all the available wavelength bands. A colour-colour or colour-magnitude selection can be used as an alternative estimate of cluster membership (e.g. Garilli, Maccagni & Andreon 1999, De Propris et al. 1998) which can be compared to the estimate based on an incomplete spectroscopic sample.

An investigation into the contribution of different morphological types to the LF has only been possible with nearby clusters, such as Virgo (Kraan-Korteweg 1981), Coma (Thompson & Gregory 1980), and Centaurus (Jerjen & Tammann 1997). The morphologies of the cluster galaxies can be estimated by visually examining the images in different wavelength bands (e.g in the analysis of DENIS galaxies in the ZOA Schröder et al. 2006). This would provide insight into the complex make-up of the cluster and give a better understanding of the shape of the total LF and significance of the dip. An independent estimate of the distance to the Norma cluster may be obtained using the type-specific LFs, as discussed in Jerjen & Tammann (1997).

The availability of photometry in a number of wavelength bands for the same area suggests a further avenue of research. The difficulty of comparing different LFs often arises from differences in the techniques used and survey properties, rather than intrinsic differences in the LF. A comparison of the NIR and optical LFs of the Norma cluster, determined using similar methods and covering the same area to equivalent depths, would provide a more complete picture of the galaxy distribution in the cluster and improve our understanding of the processes occuring in the dense cluster environment.

Appendix A

Catalogue of Galaxies in the Norma Cluster

The catalogue of galaxies identified in the K_s-band survey of the central 0.8 Mpc^2 of the Norma cluster is given in Table A.1. The table contains the following columns:

Column 1: Identification number from this survey.

Column 2: Identification number from the catalogue of Woudt & Kraan-Korteweg (2001), if a corresponding object was found in their deep optical search of the SRC IIIaJ sky survey plates, or an 'R' indicating identification on the R-band images of the cluster.

Column 3: Right Ascension (RA) and Declination (Dec) (J2000)

Column 4: Galactic longitude (l) and latitude (b) in degrees

Column 5: Galactic Extinction in the K_s-band (A_{K_s}) in magnitudes, as derived from the Schlegel, Finkbeiner & Davis (1998) reddening maps (see Section 3.1.2)

Column 6: Classification as likely galaxy (G) or candidate (C), based on eye-balling of the K_s- and R-band images of the cluster

Column 7: Total K_s-band magnitude and error, given by the Auto (Kron) magnitude of SExtr (uncorrected for galactic extinction or k-correction for redshift)

Column 8: B_J magnitude, corresponding approximately to B_{25} isophotal magnitude, from the catalogue of Woudt & Kraan-Korteweg (2001). The typical 1σ uncertainty associated with these magnitudes is $0.^m5$.

Column 9: Diameter of the object (D) in arcseconds, as estimated from SExtractor's `ISOAREA` parameter: $D \simeq 2A_{\rm iso} = 2\sqrt{\frac{\rm ISOAREA \times ELONGATION}{\pi}}$ where $A_{\rm iso}$ is the isophotal semi-major axis, `ISOAREA` is the isophotal area and `ELONGATION` is the ratio of the semi-major and semi-minor axes.

Column 10: Heliocentric velocity in km s^{-1} from NED[1], with additional sources from 2dF spectroscopy (Woudt et al. 2007, in preparation).

[1]The NASA/IPAC Extragalactic Database (NED) is operated by the Jet Propulsion Laboratory, California Institute of Technology, under contract with the National Aeronautics and Space Administration.

Column 11: The field/s the object was identified in, corresponding to those shown in Fig. 2.1, followed by a photometric flag in brackets. The flag indicates the reliability of photometry in each image in which the object was detected. The number given is the sum of one or more of the following flags: "0" indicates reliable photometry, "1" indicates that neighbouring objects may have an influence on the photometry of the object, "2" indicates that the object was originally blended with another object, "4" indicates that at least one pixel is saturated, "8" indicates that the object was truncated due to proximity to the boundary of an image, "16" indicates that the object's aperture data is incomplete or corrupted, "32" indicates that the object's isophotal data is incomplete or corrupted. If an object is identified in more than one field, the magnitude given in Column 7 is the average of the data from all fields in which the photometric flag is zero.

Table A.1: Photometric Catalogue of Galaxies Identified in the K_s-band

K_s ID	Optical ID	RA (J2000) [^{h} ^{m} ^{s}]	Dec [$^\circ$ $'$ $''$]	Gal l [$^\circ$]	Gal b [$^\circ$]	A_{K_s} [mag]	Class	K_s [mag]	B_J [mag]	D [$''$]	Vel. km s^{-1}	Field (Flag)
(1)	(2)	(3a)	(3b)	(4a)	(4b)	(5)	(6)	(7) (8)	(9)	(10)	(11)	
K001	WKK6091	16 11 50.8	-60 36 14	325.21	-6.72	0.070	G	13.34 ± 0.02	17.9	8	3235	29(0)
K002	WKK6092	16 11 51.4	-60 37 55	325.20	-6.74	0.070	G	10.74 ± 0.00	14.7	26	4688	29(2)
K003	WKK6090	16 11 52.0	-61 11 41	324.81	-7.15	0.084	G	13.17 ± 0.02	16.2	7	...	34(2)
K004	...	16 11 52.1	-60 37 34	325.20	-6.74	0.070	C	15.04 ± 0.04	...	3	...	29(0)
K005	...	16 11 52.6	-61 09 09	324.84	-7.12	0.086	C	15.39 ± 0.05	...	3	...	34(0)
K006	...	16 11 54.2	-60 37 18	325.21	-6.74	0.070	C	16.33 ± 0.07	...	2	...	29(0)
K007	...	16 11 55.6	-60 39 39	325.18	-6.77	0.074	G	15.19 ± 0.05	...	4	...	29(0)
K008	WKK6100	16 11 55.9	-60 43 33	325.14	-6.82	0.079	G	12.36 ± 0.01	15.7	9	...	30(0)
K009	...	16 11 56.8	-61 01 05	324.94	-7.03	0.074	C	15.72 ± 0.06	...	2	...	32(0)
K010	WKK6098	16 11 57.1	-61 07 53	324.86	-7.11	0.082	G	14.69 ± 0.04	17.1	4	10482	33(0) 34(0)
K011	R	16 11 57.6	-61 10 07	324.83	-7.14	0.086	G	14.57 ± 0.03	...	4	...	34(0)
K012	WKK6101	16 11 58.6	-60 51 11	325.05	-6.92	0.081	G	12.51 ± 0.01	16.7	15	4416	31(0)
K013	...	16 11 59.4	-60 37 43	325.21	-6.75	0.074	G	13.17 ± 0.01	...	11	...	29(0)
K014	R	16 12 00.4	-60 51 26	325.05	-6.92	0.081	G	13.71 ± 0.02	...	7	...	31(0)
K015	...	16 12 01.0	-61 01 15	324.94	-7.04	0.074	C	15.68 ± 0.06	...	3	...	33(0)
K016	R	16 12 09.7	-60 54 11	325.04	-6.97	0.079	G	14.54 ± 0.02	...	5	...	31(0) 32(0)
K017	R	16 12 10.5	-61 15 09	324.79	-7.22	0.084	G	14.26 ± 0.02	...	6	...	34(0)
K018	WKK6116	16 12 11.6	-60 46 60	325.12	-6.88	0.081	G	9.85 ± 0.00	14.6	31	3803	30(0) 31(16)
K019	...	16 12 12.2	-60 41 21	325.19	-6.82	0.074	C	15.25 ± 0.05	...	3	...	29(0) 30(0)
K020	R	16 12 12.9	-60 58 36	324.99	-7.02	0.079	G	14.90 ± 0.04	...	4	16300	32(0)
K021	R	16 12 13.3	-61 05 52	324.91	-7.11	0.082	G	14.48 ± 0.03	...	5	...	33(0)
K022	...	16 12 13.6	-60 34 12	325.27	-6.73	0.076	C	15.84 ± 0.06	...	3	...	29(0)
K023	R	16 12 15.6	-61 00 10	324.98	-7.05	0.079	G	14.50 ± 0.03	...	8	...	32(2)
K024	...	16 12 16.0	-61 14 38	324.81	-7.22	0.084	C	16.26 ± 0.06	...	3	...	34(0)
K025	WKK6120	16 12 18.3	-61 02 29	324.95	-7.08	0.079	G	12.15 ± 0.01	16.6	13	5508	33(0)
K026	...	16 12 18.5	-60 44 37	325.16	-6.86	0.076	C	15.85 ± 0.04	...	3	...	30(0)
K027	WKK6123	16 12 20.2	-61 06 38	324.91	-7.13	0.082	G	11.66 ± 0.00	14.7	15	10611	33(0)
K028	...	16 12 21.0	-61 14 35	324.82	-7.23	0.084	C	15.66 ± 0.05	...	2	...	34(0)
K029	WKK6126	16 12 21.2	-60 50 15	325.10	-6.94	0.081	G	12.18 ± 0.01	16.7	18	3770	31(0)
K030	WKK6125	16 12 22.3	-61 04 48	324.93	-7.11	0.082	G	12.80 ± 0.01	16.9	12	3937	33(0)
K031	WKK6131	16 12 24.2	-60 58 11	325.01	-7.04	0.079	G	11.61 ± 0.00	16.3	18	4784	32(0)

Table A.1 – Continued

K_s ID	Optical ID	RA (J2000) Dec		Gal l	Gal b	A_{K_s}	Class	K_s [mag]	B_J	D	Vel.	Field (Flag)
		[^{h} ^{m} ^{s}]	[$^\circ$ $'$ $''$]	[$^\circ$]	[$^\circ$]	[mag]		[mag]	[mag]	[$''$]	km s^{-1}	
(1)	(2)	(3a)	(3b)	(4a)	(4b)	(5)	(6)	(7) (8)	(9)	(10)	(11)	
K032	R	16 12 26.1	-60 55 44	325.04	-7.01	0.079	G	15.39 ± 0.04	...	3	...	32(0)
K033	WKK6135	16 12 26.6	-61 03 52	324.95	-7.11	0.082	G	14.39 ± 0.03	17.2	5	4426	33(0)
K034	...	16 12 30.3	-60 42 43	325.20	-6.86	0.076	C	16.05 ± 0.06	...	3	...	30(0)
K035	...	16 12 31.2	-61 00 35	324.99	-7.07	0.079	C	15.97 ± 0.06	...	2	...	32(0)
K036	...	16 12 32.5	-60 52 31	325.09	-6.98	0.077	C	15.55 ± 0.05	...	5	...	31(0)
K037	...	16 12 33.3	-60 34 43	325.30	-6.76	0.075	C	16.02 ± 0.06	...	3	...	29(0)
K038	...	16 12 34.4	-60 48 03	325.14	-6.93	0.081	C	15.41 ± 0.05	...	3	...	31(0)
K039	...	16 12 36.7	-60 43 44	325.20	-6.88	0.076	C	16.48 ± 0.08	...	2	...	30(0)
K040	...	16 12 37.7	-61 07 38	324.92	-7.17	0.084	C	15.55 ± 0.05	...	3	...	34(0)
K041	...	16 12 39.4	-61 13 51	324.85	-7.25	0.084	C	15.77 ± 0.06	...	2	...	34(0)
K042	R	16 12 40.2	-60 58 52	325.03	-7.07	0.079	G	14.55 ± 0.03	...	5	...	15(0)
K043	...	16 12 40.2	-60 41 46	325.22	-6.86	0.076	C	16.49 ± 0.07	...	2	...	12(0)
K044	R	16 12 40.2	-60 58 52	325.03	-7.07	0.079	G	14.43 ± 0.02	...	5	...	32(0)
K045	...	16 12 40.3	-61 03 59	324.97	-7.13	0.079	G	14.95 ± 0.03	...	4	...	15(0)
K046	...	16 12 41.6	-60 50 06	325.13	-6.96	0.077	C	15.01 ± 0.04	...	3	...	31(0)
K047	...	16 12 42.2	-60 49 41	325.14	-6.96	0.077	C	16.53 ± 0.08	...	2	...	31(0)
K048	...	16 12 42.6	-61 11 36	324.88	-7.22	0.084	C	16.28 ± 0.07	...	3	...	16(0)
K049	...	16 12 42.7	-60 38 51	325.26	-6.83	0.075	G	15.89 ± 0.04	...	3	...	12(0) 29(0)
K050	...	16 12 44.9	-61 11 39	324.89	-7.23	0.084	C	16.63 ± 0.08	...	2	...	16(0)
K051	...	16 12 45.4	-61 04 19	324.97	-7.14	0.079	G	14.87 ± 0.03	...	4	...	16(0) 33(0)
K052	...	16 12 45.6	-61 11 08	324.89	-7.22	0.084	C	15.96 ± 0.05	...	3	...	16(0) 34(0)
K053	...	16 12 46.3	-60 58 35	325.04	-7.07	0.079	C	16.26 ± 0.08	...	2	...	15(0)
K054	R	16 12 47.7	-60 39 34	325.26	-6.84	0.075	G	13.73 ± 0.01	...	6	...	12(0) 29(0)
K055	...	16 12 48.0	-61 08 43	324.92	-7.20	0.084	C	15.44 ± 0.04	...	4	...	34(0)
K056	...	16 12 48.2	-61 10 15	324.91	-7.21	0.084	C	15.89 ± 0.06	...	4	...	16(0)
K057	...	16 12 48.9	-60 34 33	325.32	-6.78	0.075	C	16.77 ± 0.08	...	2	...	28(0)
K058	WKK6148	16 12 50.8	-60 38 36	325.28	-6.84	0.075	G	11.71 ± 0.00	16.5	17	4272	12(0) 29(0)
K059	...	16 12 51.0	-61 08 59	324.93	-7.20	0.084	C	16.14 ± 0.07	...	2	...	34(0)
K060	...	16 12 51.3	-60 36 51	325.30	-6.82	0.075	G	15.37 ± 0.04	...	4	...	28(0) 29(0)
K061	...	16 12 51.4	-61 11 49	324.89	-7.24	0.084	C	16.19 ± 0.07	...	2	...	34(0)
K062	...	16 12 51.7	-61 11 57	324.89	-7.24	0.084	C	15.62 ± 0.05	...	3	...	16(0)
K063	R	16 12 51.9	-60 35 39	325.31	-6.80	0.075	G	14.60 ± 0.03	...	4	...	28(0) 29(0)

Table A.1 – Continued

K_s ID	Optical ID	RA (J2000) [^{h} ^{m} ^{s}]	Dec [$^\circ$ $'$ $''$]	Gal l [$^\circ$]	Gal b [$^\circ$]	A_{K_s} [mag]	Class	K_s [mag] [mag]	B_J [mag]	D [$''$]	Vel. km s^{-1}	Field (Flag)
(1)	(2)	(3a)	(3b)	(4a)	(4b)	(5)	(6)	(7) (8)	(9)	(10)	(11)	
K064	...	16 12 52.8	-60 35 24	325.32	-6.80	0.075	C	15.85 ± 0.05	...	3	...	28(0)
K065	...	16 12 54.4	-60 38 38	325.28	-6.84	0.075	G	14.21 ± 0.01	...	5	...	12(0) 29(0)
K066	...	16 12 54.6	-61 13 53	324.87	-7.27	0.081	C	14.98 ± 0.03	...	5	...	35(0)
K067	...	16 12 54.7	-61 14 39	324.86	-7.28	0.081	C	15.71 ± 0.06	...	3	...	35(0)
K068	...	16 12 56.0	-61 16 51	324.84	-7.30	0.074	C	16.09 ± 0.06	...	3	...	35(0)
K069	WKK6152	16 12 56.7	-61 01 04	325.03	-7.12	0.079	G	10.70 ± 0.00	15.6	32	4266	15(3) 32(27) 33(19)
K070	...	16 12 58.1	-60 36 57	325.31	-6.83	0.075	G	14.27 ± 0.01	...	6	...	12(0) 28(0)
K071	...	16 12 58.6	-60 50 59	325.15	-7.00	0.077	C	15.91 ± 0.06	...	3	...	14(0)
K072	...	16 13 01.7	-60 31 52	325.37	-6.77	0.076	C	15.32 ± 0.03	...	3	...	28(0)
K073	WKK6160	16 13 04.8	-60 51 55	325.14	-7.02	0.077	G	12.94 ± 0.01	17.7	10	6508	14(0)
K074	...	16 13 05.9	-61 14 00	324.89	-7.28	0.081	G	15.22 ± 0.04	...	3	...	35(0)
K075	...	16 13 06.4	-61 07 57	324.96	-7.21	0.081	C	15.41 ± 0.05	...	4	...	16(0)
K076	R	16 13 07.4	-60 40 45	325.28	-6.89	0.077	G	15.23 ± 0.03	...	4	...	12(0)
K077	...	16 13 08.0	-61 18 15	324.84	-7.34	0.074	G	15.58 ± 0.06	...	3	...	35(0)
K078	...	16 13 08.1	-61 18 37	324.84	-7.34	0.074	G	15.27 ± 0.05	...	3	...	35(0)
K079	...	16 13 08.5	-61 00 32	325.05	-7.13	0.079	C	15.80 ± 0.06	...	2	...	15(0)
K080	...	16 13 08.7	-60 46 46	325.21	-6.96	0.073	C	16.44 ± 0.07	...	2	...	13(0) 13(0)
K081	...	16 13 09.4	-61 13 28	324.90	-7.28	0.081	C	15.01 ± 0.03	...	4	...	35(0)
K082	R	16 13 10.0	-60 36 56	325.32	-6.84	0.075	G	15.09 ± 0.02	...	4	...	28(0)
K083	WKK6166	16 13 10.1	-60 45 04	325.23	-6.94	0.076	G	13.25 ± 0.01	17.1	9	5073	12(24) 13(2)
K084	...	16 13 13.4	-61 05 23	325.00	-7.19	0.081	C	16.25 ± 0.04	...	3	...	16(0)
K085	...	16 13 15.1	-61 01 01	325.05	-7.14	0.076	C	15.67 ± 0.05	...	3	...	15(0)
K086	R	16 13 16.8	-60 54 36	325.13	-7.07	0.076	G	15.96 ± 0.07	...	3	...	14(0)
K087	...	16 13 21.0	-60 40 03	325.31	-6.90	0.077	C	16.35 ± 0.07	...	2	...	12(0)
K088	R	16 13 21.2	-60 50 14	325.19	-7.02	0.073	G	15.10 ± 0.04	...	3	...	13(0)
K089	...	16 13 24.9	-61 13 33	324.92	-7.30	0.081	C	14.45 ± 0.01	...	5	...	35(0)
K090	...	16 13 25.9	-60 43 45	325.27	-6.95	0.077	G	16.14 ± 0.06	...	2	...	12(0)
K091	...	16 13 26.3	-61 08 47	324.98	-7.25	0.081	C	15.59 ± 0.05	...	3	...	16(2)
K092	R	16 13 26.4	-60 44 21	325.26	-6.96	0.080	G	14.07 ± 0.03	...	7	...	12(0) 13(0)
K093	R	16 13 27.2	-60 48 55	325.21	-7.01	0.073	G	15.76 ± 0.05	...	3	...	13(0)
K094	WKK6176	16 13 27.2	-60 45 50	325.25	-6.97	0.073	G	11.62 ± 0.01	14.6	19	4680	13(0)
K095	...	16 13 30.7	-60 35 24	325.37	-6.85	0.078	C	16.02 ± 0.06	...	2	...	28(0)

Table A.1 – Continued

K_s ID	Optical ID	RA (J2000) [^{h} ^{m} ^{s}]	Dec [$^\circ$ $'$ $''$]	Gal l [$^\circ$]	Gal b [$^\circ$]	A_{K_s} [mag]	Class	K_s [mag] [mag]	B_J [mag]	D [$''$]	Vel. km s^{-1}	Field (Flag)
(1)	(2)	(3a)	(3b)	(4a)	(4b)	(5)	(6)	(7) (8)	(9)	(10)	(11)	
K096	WKK6180	16 13 32.2	-61 00 22	325.09	-7.16	0.080	G	10.55 ± 0.00	15.2	24	4602	5(18) 15(2)
K097	R	16 13 32.3	-60 51 41	325.19	-7.05	0.073	G	14.17 ± 0.03	...	4	...	14(2)
K098	WKK6183	16 13 32.9	-60 49 23	325.21	-7.03	0.073	G	10.44 ± 0.00	15.6	25	5909	3(18) 13(0)
K099	R	16 13 34.5	-60 51 05	325.20	-7.05	0.073	G	12.94 ± 0.01	...	8	4583	3(3) 4(3) 13(2) 14(2)
K100	WKK6186	16 13 35.7	-60 51 54	325.19	-7.06	0.073	G	9.91 ± 0.00	14.8	50	5743	3(27) 4(18) 14(2)
K101	R	16 13 36.5	-60 52 49	325.18	-7.07	0.073	G	14.83 ± 0.04	...	4	4117	14(0)
K102	...	16 13 36.9	-60 30 45	325.44	-6.81	0.076	C	15.57 ± 0.05	...	3	...	28(0)
K103	R	16 13 37.1	-61 04 45	325.04	-7.22	0.081	G	15.58 ± 0.05	...	3	...	5(0) 15(0) 16(0) 17(0)
K104	...	16 13 38.3	-60 35 49	325.38	-6.87	0.078	C	16.77 ± 0.08	...	2	...	28(0)
K105	R	16 13 39.0	-60 57 20	325.13	-7.13	0.076	G	15.27 ± 0.04	...	3	...	5(0) 14(0) 15(0)
K106	WKK6190	16 13 39.4	-60 59 56	325.10	-7.16	0.080	G	11.08 ± 0.00	16.0	19	4309	5(0) 15(0)
K107	...	16 13 40.4	-60 38 26	325.35	-6.90	0.078	C	15.50 ± 0.04	...	3	...	11(0) 12(0)
K108	...	16 13 40.4	-61 12 12	324.96	-7.31	0.083	C	15.93 ± 0.07	...	2	...	36(0)
K109	...	16 13 41.3	-61 17 34	324.90	-7.38	0.072	C	15.58 ± 0.06	...	3	...	36(0)
K110	...	16 13 41.6	-60 44 30	325.28	-6.98	0.080	C	15.70 ± 0.06	...	2	...	3(0)
K111	R	16 13 41.8	-61 14 19	324.94	-7.34	0.081	G	14.41 ± 0.02	...	5	...	35(0)
K112	...	16 13 42.2	-60 37 01	325.37	-6.89	0.078	G	15.37 ± 0.04	...	3	...	11(0)
K113	R	16 13 44.4	-60 55 01	325.17	-7.11	0.073	G	13.90 ± 0.02	...	6	5705	4(0) 14(16)
K114	...	16 13 45.6	-61 00 01	325.11	-7.17	0.080	C	12.45 ± 0.01	...	12	...	5(3)
K115	WKK6193	16 13 46.0	-61 00 29	325.10	-7.18	0.080	G	10.06 ± 0.00	14.9	44	4235	5(3)
K116	WKK6196	16 13 47.6	-60 53 04	325.19	-7.09	0.073	G	11.71 ± 0.01	16.2	14	4818	4(3)
K117	R	16 13 50.1	-61 10 09	325.00	-7.30	0.083	G	13.97 ± 0.03	...	9	...	17(3)
K118	WKK6199	16 13 50.2	-60 37 22	325.38	-6.91	0.078	G	11.60 ± 0.00	16.2	24	...	11(2) 27(0)
K119	R	16 13 50.6	-60 57 45	325.14	-7.15	0.080	G	16.16 ± 0.07	...	2	...	4(0) 5(0)
K120	...	16 13 53.1	-60 51 19	325.22	-7.08	0.073	C	16.26 ± 0.07	...	3	...	3(0)
K121	WKK6202	16 13 53.5	-60 47 49	325.26	-7.04	0.080	G	11.32 ± 0.01	16.1	22	3521	3(0)
K122	WKK62** NC0656	16 13 53.7	-60 52 02	325.21	-7.09	0.073	G	10.67 ± 0.00	15.4	36	3007	4(2)
K123	...	16 13 55.3	-61 03 27	325.08	-7.23	0.080	C	15.30 ± 0.05	...	3	...	5(0)
K124	WKK6204	16 13 56.2	-61 00 41	325.12	-7.19	0.080	G	9.49 ± 0.00	14.9	40	4584	5(3)
K125	WKK6207	16 13 57.5	-60 56 24	325.17	-7.14	0.073	G	10.39 ± 0.00	15.3	34	3468	4(2)
K126	WKK6209	16 13 58.6	-60 54 27	325.19	-7.12	0.073	G	13.30 ± 0.02	18.1	7	...	4(2)
K127	...	16 13 59.0	-60 46 23	325.29	-7.03	0.080	G	13.60 ± 0.02	...	9	...	3(0)

Table A.1 – Continued

K_s ID	Optical ID	RA (J2000) [^{h} ^{m} ^{s}]	Dec [° ′ ″]	Gal l [°]	Gal b [°]	A_{K_s} [mag]	Class	K_s [mag] [mag]	B_J [mag]	D [″]	Vel. km s^{-1}	Field (Flag)
(1)	(2)	(3a)	(3b)	(4a)	(4b)	(5)	(6)	(7) (8)	(9)	(10)	(11)	
K128	...	16 13 59.8	-60 47 04	325.28	-7.04	0.080	C	16.37 ± 0.07	...	2	...	3(0)
K129	WKK6211	16 14 00.0	-60 58 39	325.15	-7.17	0.080	G	12.98 ± 0.01	17.4	11	4520	4(16) 5(0)
K130	WKK6212	16 14 01.0	-60 59 28	325.14	-7.19	0.080	G	10.22 ± 0.00	15.6	28	3323	5(2)
K131	R	16 14 01.8	-60 59 40	325.14	-7.19	0.080	G	13.14 ± 0.02	...	10	...	5(3)
K132	WKK6216	16 14 02.1	-60 54 05	325.20	-7.12	0.073	G	12.66 ± 0.01	17.1	12	5056	4(0)
K133	...	16 14 02.6	-61 02 50	325.10	-7.23	0.080	C	15.98 ± 0.06	...	3	...	5(0)
K134	WKK6214	16 14 02.7	-61 13 04	324.98	-7.35	0.076	G	13.67 ± 0.02	17.1	8	5054	36(0)
K135	R	16 14 02.8	-61 00 54	325.12	-7.21	0.080	G	13.66 ± 0.02	...	7	4501	5(0)
K136	...	16 14 03.2	-60 58 28	325.15	-7.18	0.074	C	16.39 ± 0.08	...	2	...	5(0)
K137	...	16 14 03.3	-61 10 55	325.01	-7.33	0.083	C	16.18 ± 0.07	...	2	...	17(0)
K138	R	16 14 04.4	-60 46 55	325.29	-7.04	0.080	G	14.43 ± 0.03	...	4	3564	3(0)
K139	...	16 14 05.4	-60 34 25	325.44	-6.89	0.078	C	15.85 ± 0.04	...	2	...	27(0)
K140	...	16 14 05.7	-61 04 11	325.09	-7.25	0.080	C	15.72 ± 0.05	...	3	...	5(2)
K141	...	16 14 05.8	-60 50 45	325.25	-7.09	0.073	C	14.87 ± 0.02	...	5	...	3(0)
K142	WKK6228	16 14 06.1	-60 41 54	325.35	-6.98	0.083	G	10.93 ± 0.00	16.0	28	5671	11(3)
K143	...	16 14 07.0	-61 07 19	325.06	-7.29	0.083	G	14.31 ± 0.02	...	6	...	17(0)
K144	R	16 14 07.7	-60 49 08	325.27	-7.07	0.076	G	14.66 ± 0.04	...	4	4647	3(2)
K145	R	16 14 08.6	-61 03 20	325.10	-7.24	0.080	G	13.90 ± 0.02	...	6	5185	5(0)
K146	...	16 14 08.7	-61 11 10	325.01	-7.34	0.083	C	15.22 ± 0.03	...	3	...	17(3)
K147	...	16 14 09.2	-61 09 21	325.03	-7.32	0.083	C	14.50 ± 0.01	...	5	...	17(0)
K148	...	16 14 09.6	-60 45 54	325.31	-7.04	0.080	C	15.84 ± 0.06	...	3	...	3(0)
K149	...	16 14 09.8	-61 13 57	324.98	-7.37	0.076	C	15.34 ± 0.04	...	4	...	36(0)
K150	WKK6229	16 14 10.4	-60 51 01	325.25	-7.10	0.076	G	11.58 ± 0.00	16.6	13	5376	3(0) 4(0)
K151	...	16 14 10.6	-60 58 18	325.17	-7.19	0.074	C	15.40 ± 0.05	...	3	...	5(0)
K152	WKK6230	16 14 10.7	-60 44 32	325.33	-7.02	0.080	G	11.44 ± 0.00	16.6	22	3025	11(2) 3(2)
K153	...	16 14 13.5	-61 05 33	325.09	-7.28	0.083	G	12.84 ± 0.01	...	9	...	17(0)
K154	R	16 14 15.3	-61 00 28	325.15	-7.22	0.080	G	15.05 ± 0.04	...	3	...	5(0)
K155	...	16 14 15.8	-60 47 34	325.30	-7.06	0.076	C	15.58 ± 0.06	...	3	...	3(0)
K156	WKK6233	16 14 18.0	-60 53 26	325.23	-7.14	0.073	G	11.83 ± 0.00	17.1	13	5055	4(0)
K157	R	16 14 19.2	-61 05 09	325.10	-7.28	0.083	G	14.78 ± 0.03	...	6	...	5(16) 17(0)
K158	R	16 14 19.8	-61 04 58	325.10	-7.28	0.083	G	14.06 ± 0.02	...	7	29515	5(0) 17(0)
K159	...	16 14 20.5	-61 17 12	324.96	-7.43	0.076	C	15.63 ± 0.06	...	3	...	36(0)

Table A.1 – Continued

K_s ID	Optical ID	RA (J2000) Dec		Gal l	Gal b	A_{K_s}	Class	K_s [mag]	B_J	D	Vel.	Field (Flag)
		[^{h} ^{m} ^{s}]	[$^\circ$ $'$ $''$]	[°]	[°]	[mag]		[mag]	[mag]	[″]	km s^{-1}	
(1)	(2)	(3a)	(3b)	(4a)	(4b)	(5)	(6)	(7) (8)	(9)	(10)	(11)	
K160	WKK6235	16 14 22.6	-61 08 38	325.06	-7.33	0.083	G	11.04 ± 0.00	15.6	21	4053	17(0)
K161	...	16 14 23.0	-61 13 59	325.00	-7.39	0.076	C	16.02 ± 0.07	...	2	...	36(0)
K162	...	16 14 24.1	-60 44 38	325.35	-7.04	0.080	C	15.82 ± 0.04	...	3	...	11(0)
K163	WKK6239	16 14 25.4	-61 03 40	325.12	-7.27	0.083	G	10.48 ± 0.00	15.2	34	4235	5(2)
K164	...	16 14 29.4	-60 43 20	325.37	-7.03	0.083	C	15.97 ± 0.04	...	3	...	11(0)
K165	...	16 14 29.4	-61 04 52	325.12	-7.29	0.083	G	15.08 ± 0.04	...	4	...	5(0) 17(0) 18(2)
K166	...	16 14 30.0	-61 01 28	325.16	-7.25	0.077	C	15.78 ± 0.04	...	3	...	5(0)
K167	WKK6242	16 14 30.5	-60 53 46	325.25	-7.16	0.074	G	10.71 ± 0.00	16.4	21	5197	1(0) 4(2)
K168	...	16 14 30.5	-60 41 11	325.39	-7.01	0.083	C	16.88 ± 0.08	...	2	...	11(0)
K169	...	16 14 30.8	-61 09 56	325.06	-7.35	0.079	G	15.91 ± 0.06	...	2	...	17(0)
K170	...	16 14 31.8	-61 11 09	325.05	-7.37	0.076	C	15.95 ± 0.05	...	3	...	37(0)
K171	...	16 14 33.3	-61 17 03	324.98	-7.44	0.076	G	15.42 ± 0.05	...	3	...	36(0) 37(3)
K172	...	16 14 33.6	-61 01 48	325.16	-7.26	0.077	C	15.97 ± 0.05	...	3	...	5(0)
K173	R	16 14 33.7	-60 54 16	325.25	-7.17	0.074	G	14.19 ± 0.02	...	5	29400	1(0)
K174	...	16 14 33.8	-61 03 56	325.13	-7.29	0.083	G	15.44 ± 0.04	...	3	...	5(0)
K175	R	16 14 36.3	-60 45 04	325.36	-7.06	0.087	G	15.11 ± 0.04	...	4	...	2(0) 10(16)
K176	R	16 14 37.5	-61 05 04	325.13	-7.30	0.083	G	14.64 ± 0.03	...	6	...	6(3) 5(3) 17(3) 18(3)
K177	R	16 14 38.6	-61 11 01	325.06	-7.38	0.079	G	16.09 ± 0.06	...	2	...	18(0)
K178	...	16 14 40.0	-60 49 46	325.31	-7.12	0.076	C	15.79 ± 0.06	...	3	...	2(0)
K179	R	16 14 40.7	-61 03 30	325.15	-7.29	0.083	G	15.82 ± 0.04	...	3	...	5(16)
K180	WKK6248	16 14 41.1	-60 35 39	325.48	-6.96	0.089	G	14.47 ± 0.03	17.7	7	...	26(0) 27(16)
K181	...	16 14 43.1	-61 16 40	325.00	-7.45	0.074	G	14.65 ± 0.04	...	4	...	37(2)
K182	...	16 14 43.2	-61 04 03	325.15	-7.30	0.083	C	15.64 ± 0.04	...	3	...	6(0)
K183	...	16 14 44.0	-61 09 50	325.08	-7.37	0.079	C	16.50 ± 0.08	...	2	...	18(0)
K184	...	16 14 44.1	-60 50 03	325.31	-7.13	0.076	C	16.14 ± 0.07	...	2	...	2(0)
K185	WKK6251	16 14 45.1	-60 55 36	325.25	-7.20	0.074	G	11.47 ± 0.01	15.9	24	5689	1(0)
K186	WKK6250	16 14 45.2	-61 01 50	325.18	-7.28	0.077	G	10.59 ± 0.00	15.7	28	6258	6(0)
K187	WKK6252	16 14 45.4	-60 51 41	325.29	-7.16	0.072	G	12.10 ± 0.01	16.8	13	5863	1(0) 2(0)
K188	R	16 14 46.5	-60 53 59	325.27	-7.18	0.072	G	16.00 ± 0.08	...	2	...	1(0)
K189	WKK6254	16 14 47.6	-61 11 43	325.06	-7.40	0.079	G	11.51 ± 0.00	15.4	27	4910	18(2) 37(0)
K190	...	16 14 48.8	-60 54 20	325.27	-7.19	0.072	G	15.68 ± 0.06	...	3	...	1(0)
K191	...	16 14 49.5	-60 37 26	325.47	-6.99	0.089	C	16.11 ± 0.04	...	3	...	10(0)

Table A.1 – Continued

K_s ID	Optical ID	RA (J2000) Dec		Gal l	Gal b	A_{K_s}	Class	K_s [mag]	B_J	D	Vel.	Field (Flag)
		[^{h} ^{m} ^{s}]	[$^\circ$ $'$ $''$]	[$^\circ$]	[$^\circ$]	[mag]		[mag]	[mag]	[$''$]	km s^{-1}	
(1)	(2)	(3a)	(3b)	(4a)	(4b)	(5)	(6)	(7) (8)	(9)	(10)	(11)	
K192	...	16 14 51.1	-60 57 42	325.23	-7.24	0.074	C	15.14 ± 0.04	...	3	...	1(0)
K193	...	16 14 52.2	-60 52 49	325.29	-7.18	0.072	G	15.48 ± 0.06	...	3	...	1(0)
K194	...	16 14 55.0	-60 59 50	325.21	-7.27	0.077	G	13.57 ± 0.02	...	5	...	6(3)
K195	...	16 14 56.9	-60 42 26	325.42	-7.06	0.087	C	15.90 ± 0.04	...	3	...	10(0)
K196	...	16 14 58.0	-60 41 21	325.43	-7.05	0.083	C	16.15 ± 0.07	...	2	...	10(0)
K197	WKK6263	16 14 58.9	-60 46 04	325.38	-7.11	0.087	G	13.95 ± 0.03	17.2	4	3260	2(0)
K198	WKK6264	16 14 59.6	-60 52 01	325.31	-7.18	0.072	G	13.57 ± 0.02	17.8	7	4940	1(2)
K199	WKK6265	16 14 60.0	-60 47 23	325.37	-7.12	0.087	G	13.42 ± 0.02	16.4	9	5611	2(2)
K200	R	16 15 00.2	-61 01 05	325.21	-7.29	0.077	G	13.61 ± 0.01	...	8	...	6(0)
K201	...	16 15 00.4	-60 37 53	325.48	-7.01	0.089	C	16.26 ± 0.07	...	2	...	10(0)
K202	...	16 15 00.5	-60 44 25	325.40	-7.09	0.087	G	16.18 ± 0.07	...	2	...	2(0) 10(0)
K203	WKK6267	16 15 01.1	-60 48 34	325.35	-7.14	0.087	G	14.38 ± 0.03	17.9	4	...	2(0)
K204	...	16 15 03.4	-61 03 58	325.18	-7.33	0.077	G	16.01 ± 0.07	...	3	...	6(0)
K205	WKK6269	16 15 03.8	-60 54 26	325.29	-7.21	0.072	G	8.56 ± 0.00	13.5	59	5441	1(2)
K206	...	16 15 07.2	-60 57 42	325.26	-7.26	0.072	C	16.04 ± 0.07	...	3	...	1(0)
K207	R	16 15 09.4	-60 59 29	325.24	-7.28	0.077	G	15.84 ± 0.06	...	2	...	6(0)
K208	WKK6275	16 15 09.9	-60 53 28	325.31	-7.21	0.072	G	10.65 ± 0.00	15.3	29	6861	1(2)
K209	R	16 15 10.5	-60 52 31	325.32	-7.20	0.072	G	13.81 ± 0.02	...	6	6423	1(0)
K210	WKK6277	16 15 11.4	-61 12 04	325.09	-7.44	0.079	G	14.38 ± 0.03	18.2	6	4602	18(16) 37(0)
K211	WKK6278	16 15 11.8	-60 31 52	325.56	-6.96	0.088	G	13.54 ± 0.02	17.2	10	4593	26(0)
K212	...	16 15 11.8	-60 52 01	325.33	-7.20	0.072	C	13.80 ± 0.01	...	6	...	1(3)
K213	...	16 15 12.9	-61 16 35	325.04	-7.49	0.074	C	15.90 ± 0.06	...	3	...	37(0)
K214	...	16 15 13.5	-60 38 23	325.49	-7.04	0.089	C	14.96 ± 0.02	...	4	...	10(0)
K215	...	16 15 14.2	-61 00 59	325.23	-7.31	0.077	C	16.50 ± 0.08	...	2	...	6(0)
K216	R	16 15 14.7	-60 37 59	325.50	-7.03	0.089	G	14.22 ± 0.01	...	5	...	10(0) 26(0)
K217	WKK6283	16 15 14.9	-60 35 31	325.53	-7.00	0.089	G	10.74 ± 0.00	15.2	26	6225	26(2)
K218	WKK6282	16 15 15.5	-60 56 16	325.28	-7.25	0.072	G	11.19 ± 0.00	15.9	16	4849	1(2)
K219	R	16 15 15.8	-60 37 51	325.50	-7.03	0.089	G	15.19 ± 0.04	...	4	...	10(0)
K220	...	16 15 16.0	-60 57 05	325.28	-7.26	0.072	C	15.97 ± 0.07	...	3	...	1(0)
K221	WKK6281	16 15 16.0	-61 07 58	325.15	-7.39	0.079	G	10.87 ± 0.00	15.5	37	4908	18(3)
K222	WKK6288	16 15 17.9	-60 45 06	325.42	-7.12	0.087	G	13.80 ± 0.02	17.7	8	...	2(0)
K223	...	16 15 18.0	-60 39 28	325.49	-7.06	0.098	G	14.84 ± 0.02	...	5	...	10(0)

Table A.1 – Continued

K_s ID	Optical ID	RA (J2000) Dec		Gal l	Gal b	A_{K_s}	Class	K_s [mag]	B_J	D	Vel.	Field (Flag)
		[^{h} ^{m} ^{s}]	[$^\circ$ $'$ $''$]	[$^\circ$]	[$^\circ$]	[mag]		[mag]	[mag]	[$''$]	km s^{-1}	
(1)	(2)	(3a)	(3b)	(4a)	(4b)	(5)	(6)	(7) (8)	(9)	(10)	(11)	
K224	...	16 15 19.3	-60 58 17	325.27	-7.28	0.072	C	15.85 ± 0.05	...	3	...	1(3)
K225	...	16 15 19.3	-60 45 14	325.42	-7.13	0.087	C	15.64 ± 0.06	...	2	...	2(0)
K226	WKK6289	16 15 19.9	-61 03 25	325.21	-7.34	0.077	G	12.71 ± 0.01	17.6	10	4447	6(2)
K227	...	16 15 21.9	-61 13 35	325.09	-7.47	0.074	C	15.48 ± 0.04	...	5	...	37(0)
K228	WKK6293	16 15 23.4	-60 42 48	325.45	-7.10	0.098	G	14.31 ± 0.02	18.3	8	...	10(0)
K229	WKK6291	16 15 23.5	-60 52 41	325.34	-7.22	0.072	G	14.05 ± 0.03	17.8	5	...	1(0) 1(0) 8(2)
K230	...	16 15 24.9	-60 57 44	325.28	-7.28	0.072	C	14.81 ± 0.02	...	4	...	6(0)
K231	WKK6294	16 15 25.2	-61 04 11	325.21	-7.36	0.077	G	12.08 ± 0.01	16.8	16	4547	6(0) 7(0) 18(0) 19(0)
K232	...	16 15 25.2	-60 31 31	325.59	-6.97	0.088	C	16.36 ± 0.07	...	2	...	47(0)
K233	WKK6295	16 15 25.9	-61 00 22	325.25	-7.32	0.072	G	13.17 ± 0.01	17.6	7	6101	6(2) 7(2)
K234	...	16 15 26.4	-61 06 08	325.19	-7.39	0.077	C	15.93 ± 0.05	...	3	...	19(0)
K235	WKK6297	16 15 27.1	-60 58 50	325.27	-7.30	0.072	G	11.79 ± 0.01	16.2	16	5023	6(0) 7(2)
K236	...	16 15 27.7	-61 12 25	325.11	-7.46	0.074	C	16.65 ± 0.10	...	2	...	38(0)
K237	WKK6299	16 15 28.9	-60 48 56	325.39	-7.18	0.078	G	11.53 ± 0.01	17.4	15	5211	2(0)
K238	WKK6300	16 15 29.3	-60 51 03	325.37	-7.21	0.078	G	12.98 ± 0.01	17.4	7	4586	1(0) 2(0) 8(0) 9(0)
K239	...	16 15 30.1	-60 45 42	325.43	-7.15	0.087	C	14.70 ± 0.03	...	4	...	9(0)
K240	...	16 15 30.5	-60 42 35	325.47	-7.11	0.098	C	15.87 ± 0.06	...	3	...	10(0)
K241	...	16 15 30.9	-60 45 12	325.44	-7.14	0.087	C	16.05 ± 0.06	...	3	...	9(0)
K242	...	16 15 30.9	-60 55 49	325.31	-7.27	0.072	C	16.02 ± 0.08	...	2	...	1(0)
K243	...	16 15 31.7	-60 56 54	325.30	-7.28	0.072	G	14.68 ± 0.04	...	4	...	1(0) 8(0)
K244	WKK6305	16 15 32.9	-60 39 55	325.50	-7.08	0.098	G	9.37 ± 0.00	14.4	38	4710	10(19) 25(2)
K245	...	16 15 33.7	-60 50 00	325.38	-7.20	0.078	C	14.76 ± 0.03	...	4	...	2(0)
K246	...	16 15 35.5	-60 48 52	325.40	-7.19	0.078	G	15.06 ± 0.04	...	3	...	2(16) 9(0)
K247	R	16 15 35.5	-61 12 17	325.13	-7.47	0.074	G	13.34 ± 0.02	...	8	...	37(19) 38(3)
K248	...	16 15 35.8	-60 43 41	325.46	-7.13	0.098	C	15.87 ± 0.06	...	3	...	25(0)
K249	R	16 15 36.7	-60 56 45	325.31	-7.29	0.072	G	13.96 ± 0.02	...	6	3365	8(0)
K250	...	16 15 37.7	-60 59 41	325.28	-7.32	0.072	C	16.36 ± 0.08	...	2	...	7(0)
K251	WKK6309	16 15 38.0	-60 41 59	325.49	-7.11	0.098	G	12.37 ± 0.01	16.4	10	6169	25(2)
K252	R	16 15 40.1	-60 32 18	325.60	-7.00	0.088	G	13.74 ± 0.01	...	6	...	47(0)
K253	...	16 15 40.4	-61 09 27	325.17	-7.45	0.077	C	15.40 ± 0.04	...	4	...	19(0)
K254	...	16 15 42.0	-61 13 54	325.12	-7.50	0.074	C	14.97 ± 0.03	...	4	...	38(0)
K255	...	16 15 42.4	-61 02 06	325.26	-7.36	0.073	C	16.58 ± 0.08	...	2	...	7(0)

Table A.1 – Continued

K_s ID	Optical ID	RA (J2000) Dec		Gal l	Gal b	A_{K_s}	Class	K_s [mag]	B_J	D	Vel.	Field (Flag)
		[^{h} ^{m} ^{s}]	[$^\circ$ $'$ $''$]	[$^\circ$]	[$^\circ$]	[mag]		[mag]	[mag]	[$''$]	km s^{-1}	
(1)	(2)	(3a)	(3b)	(4a)	(4b)	(5)	(6)	(7) (8)	(9)	(10)	(11)	
K256	...	16 15 42.5	-61 04 16	325.23	-7.39	0.077	C	16.41 ± 0.06	...	2	...	7(0)
K257	R	16 15 43.1	-61 02 38	325.25	-7.37	0.073	G	16.04 ± 0.07	...	2	...	7(0)
K258	...	16 15 43.1	-60 59 13	325.29	-7.33	0.072	C	16.68 ± 0.09	...	2	...	7(0)
K259	WKK6312	16 15 46.1	-60 55 08	325.34	-7.28	0.072	G	8.54 ± 0.00	13.1	58	3839	8(2)
K260	R	16 15 46.3	-61 08 25	325.19	-7.44	0.077	G	15.05 ± 0.04	...	6	...	19(0)
K261	WKK6313	16 15 46.6	-60 55 22	325.34	-7.29	0.072	G	11.86 ± 0.00	16.7	8	3319	8(3)
K262	R	16 15 47.2	-60 41 54	325.50	-7.13	0.098	G	14.04 ± 0.03	...	5	...	25(0)
K263	WKK6316	16 15 48.0	-60 42 39	325.49	-7.14	0.098	G	11.61 ± 0.01	16.1	18	4641	25(0)
K264	WKK6318	16 15 50.2	-60 48 11	325.43	-7.21	0.078	G	8.88 ± 0.00	13.2	57	3380	9(2)
K265	...	16 15 51.4	-60 45 40	325.46	-7.18	0.094	C	13.47 ± 0.01	...	7	...	9(0)
K266	...	16 15 52.7	-61 15 31	325.11	-7.53	0.074	C	15.22 ± 0.04	...	4	...	38(0)
K267	...	16 15 52.9	-60 48 09	325.43	-7.21	0.078	C	13.80 ± 0.02	...	6	...	9(3)
K268	WKK6319	16 15 53.0	-60 50 57	325.40	-7.24	0.078	G	10.42 ± 0.00	14.9	44	3877	8(18) 9(2)
K269	...	16 15 55.0	-61 11 33	325.16	-7.49	0.073	G	14.70 ± 0.03	...	5	...	19(0) 38(0)
K270	...	16 15 55.2	-61 10 25	325.18	-7.48	0.073	C	16.61 ± 0.07	...	2	...	19(0)
K271	R	16 15 55.9	-61 04 26	325.25	-7.41	0.077	G	15.43 ± 0.03	...	5	...	19(0)
K272	R	16 15 56.0	-60 37 19	325.57	-7.08	0.095	G	15.84 ± 0.06	...	3	...	25(0) 47(0)
K273	R	16 15 57.8	-60 41 54	325.52	-7.14	0.098	G	14.79 ± 0.04	...	3	...	25(0)
K274	...	16 15 58.9	-61 04 41	325.25	-7.41	0.077	C	16.73 ± 0.08	...	2	...	7(0)
K275	WKK6325	16 16 02.6	-60 57 51	325.34	-7.34	0.072	G	13.39 ± 0.01	17.5	10	...	7(0) 8(0)
K276	WKK6326	16 16 02.7	-60 39 13	325.55	-7.12	0.095	G	13.89 ± 0.03	17.9	5	5096	25(0)
K277	WKK6329	16 16 04.6	-60 30 53	325.65	-7.02	0.083	G	12.78 ± 0.01	17.3	10	4749	47(3)
K278	R	16 16 04.9	-60 47 47	325.46	-7.22	0.094	G	15.61 ± 0.06	...	4	...	9(0)
K279	...	16 16 05.2	-60 48 47	325.45	-7.23	0.078	C	16.20 ± 0.08	...	2	...	9(0)
K280	WKK6328	16 16 06.0	-60 53 10	325.39	-7.29	0.074	G	13.08 ± 0.01	17.5	11	5870	8(0)
K281	R	16 16 06.4	-61 10 30	325.19	-7.49	0.073	G	14.66 ± 0.02	...	7	...	19(0)
K282	...	16 16 06.4	-61 14 42	325.14	-7.54	0.074	C	15.88 ± 0.07	...	2	...	38(0)
K283	...	16 16 07.5	-61 04 18	325.27	-7.42	0.073	G	16.25 ± 0.07	...	3	...	7(0)
K284	WKK6360	16 16 08.7	-61 02 36	325.29	-7.40	0.073	G	11.24 ± 0.00	16.1	19	6324	7(3)
K285	...	16 16 09.3	-61 12 59	325.17	-7.53	0.073	C	15.98 ± 0.05	...	3	...	38(0)
K286	...	16 16 10.3	-60 39 39	325.56	-7.13	0.095	C	15.75 ± 0.05	...	3	...	25(0)
K287	WKK6336	16 16 11.6	-60 45 07	325.50	-7.20	0.094	G	13.34 ± 0.01	17.6	7	...	9(0)

Table A.1 – Continued

K_s ID	Optical ID	RA (J2000) [^{h} ^{m} ^{s}]	Dec [$^\circ$ $'$ $''$]	Gal l [$^\circ$]	Gal b [$^\circ$]	A_{K_s} [mag]	Class	K_s [mag] [mag]	B_J [mag]	D [$''$]	Vel. km s^{-1}	Field (Flag)
(1)	(2)	(3a)	(3b)	(4a)	(4b)	(5)	(6)	(7) (8)	(9)	(10)	(11)	
K288	R	16 16 11.9	-60 38 57	325.57	-7.13	0.095	G	15.09 ± 0.04	...	3	...	25(0)
K289	R	16 16 13.2	-60 51 28	325.43	-7.28	0.074	G	13.95 ± 0.02	...	5	...	8(0) 9(0)
K290	R	16 16 14.0	-60 51 25	325.43	-7.28	0.074	G	14.09 ± 0.02	...	6	...	8(0) 9(0)
K291	...	16 16 15.1	-60 53 03	325.41	-7.30	0.074	G	15.98 ± 0.06	...	4	...	8(0)
K292	...	16 16 15.4	-61 11 52	325.19	-7.52	0.073	C	16.09 ± 0.05	...	3	...	19(0)
K293	WKK6342	16 16 18.9	-60 57 23	325.36	-7.36	0.076	G	11.10 ± 0.00	16.3	15	4828	7(3) 8(3) 21(3) 22(19)
K294	...	16 16 19.4	-60 58 26	325.35	-7.37	0.076	C	13.95 ± 0.01	...	6	...	22(16)
K295	WKK6340	16 16 19.5	-61 17 46	325.13	-7.60	0.076	G	9.31 ± 0.00	14.1	52	6330	38(3)
K296	R	16 16 21.6	-60 46 58	325.49	-7.24	0.094	G	13.31 ± 0.02	...	7	...	9(0) 23(0)
K297	...	16 16 21.9	-61 03 13	325.30	-7.43	0.073	G	12.83 ± 0.01	...	8	...	7(3) 21(3)
K298	...	16 16 22.2	-60 58 11	325.36	-7.37	0.076	C	13.86 ± 0.02	...	6	...	8(0) 22(0)
K299	R	16 16 22.3	-61 17 31	325.13	-7.60	0.076	G	12.43 ± 0.01	...	13	...	38(3) 39(19)
K300	...	16 16 22.6	-60 37 04	325.61	-7.12	0.095	C	15.75 ± 0.07	...	2	...	25(0)
K301	WKK6349	16 16 23.1	-60 52 03	325.43	-7.30	0.074	G	13.02 ± 0.01	16.9	8	4591	8(3) 22(3)
K302	R	16 16 24.0	-60 47 03	325.49	-7.24	0.094	G	12.93 ± 0.01	...	7	...	9(0) 23(0)
K303	...	16 16 24.7	-60 40 34	325.57	-7.16	0.094	C	16.13 ± 0.08	...	2	...	25(0)
K304	...	16 16 26.0	-60 35 57	325.63	-7.11	0.095	C	14.98 ± 0.02	...	4	...	46(0) 47(0)
K305	WKK6351	16 16 27.0	-61 14 23	325.18	-7.57	0.073	G	14.72 ± 0.03	17.3	2	4451	38(0) 39(2)
K306	...	16 16 27.2	-61 17 11	325.14	-7.60	0.076	G	14.89 ± 0.04	...	4	...	38(0) 39(0)
K307	...	16 16 28.9	-60 50 18	325.46	-7.29	0.086	C	16.07 ± 0.07	...	2	...	9(0)
K308	R	16 16 31.9	-61 03 06	325.32	-7.44	0.073	G	15.13 ± 0.03	...	4	...	21(0)
K309	...	16 16 32.7	-61 10 15	325.23	-7.53	0.073	G	14.52 ± 0.03	...	5	...	19(16) 20(0)
K310	...	16 16 33.4	-61 04 27	325.30	-7.46	0.076	C	16.22 ± 0.06	...	2	...	21(0)
K311	...	16 16 35.3	-61 13 55	325.19	-7.58	0.073	C	15.97 ± 0.06	...	3	...	39(0)
K312	R	16 16 36.2	-60 50 20	325.47	-7.30	0.086	G	15.61 ± 0.06	...	2	...	23(0)
K313	WKK6359	16 16 36.7	-61 05 25	325.30	-7.48	0.076	G	13.68 ± 0.02	17.9	8	6257	20(2)
K314	WKK6360	16 16 37.0	-61 02 45	325.33	-7.44	0.073	G	10.14 ± 0.00	15.3	27	6258	21(0)
K315	...	16 16 38.5	-61 07 60	325.27	-7.51	0.076	G	13.11 ± 0.01	...	16	...	20(0)
K316	...	16 16 40.2	-61 09 40	325.25	-7.53	0.076	C	16.27 ± 0.05	...	3	...	20(0)
K317	WKK6364	16 16 40.6	-60 59 53	325.37	-7.42	0.076	G	12.40 ± 0.01	17.1	11	...	21(0)
K318	...	16 16 41.1	-60 52 13	325.46	-7.33	0.086	C	15.29 ± 0.04	...	3	...	22(0)
K319	R	16 16 42.6	-61 01 47	325.35	-7.44	0.073	G	14.38 ± 0.03	...	6	...	21(0)

Table A.1 – Continued

K_s ID	Optical ID	RA (J2000) Dec		Gal l	Gal b	A_{K_s}	Class	K_s [mag]	B_J	D	Vel.	Field (Flag)
		[^{h} ^{m} ^{s}]	[$^\circ$ $'$ $''$]	[$^\circ$]	[$^\circ$]	[mag]		[mag]	[mag]	[$''$]	km s^{-1}	
(1)	(2)	(3a)	(3b)	(4a)	(4b)	(5)	(6)	(7) (8)	(9)	(10)	(11)	
K320	...	16 16 42.8	-60 52 55	325.45	-7.34	0.086	C	14.92 ± 0.04	...	4	...	22(0)
K321	...	16 16 43.4	-61 06 12	325.30	-7.50	0.076	C	15.69 ± 0.04	...	3	...	20(0)
K322	R	16 16 46.8	-61 18 38	325.15	-7.65	0.073	G	14.75 ± 0.04	...	4	24499	39(0)
K323	...	16 16 47.0	-60 51 14	325.48	-7.32	0.086	G	15.13 ± 0.03	...	4	...	22(0)
K324	...	16 16 47.3	-60 54 02	325.44	-7.36	0.076	C	16.05 ± 0.07	...	3	...	22(0)
K325	WKK6370	16 16 49.6	-61 08 49	325.27	-7.53	0.076	G	9.91 ± 0.00	16.9	36	4702	20(2)
K326	...	16 16 51.6	-61 05 45	325.31	-7.50	0.076	C	15.96 ± 0.05	...	3	...	20(0)
K327	...	16 16 51.9	-60 55 09	325.44	-7.38	0.076	C	15.52 ± 0.04	...	3	...	22(0)
K328	R	16 16 52.0	-60 43 44	325.57	-7.24	0.094	G	14.44 ± 0.02	...	4	...	24(0)
K329	WKK6375	16 16 52.1	-60 49 25	325.51	-7.31	0.086	G	15.40 ± 0.04	17.4	2	5249	23(0)
K330	...	16 16 53.1	-61 12 41	325.23	-7.59	0.073	C	16.27 ± 0.08	...	2	...	39(0)
K331	R	16 16 55.5	-61 02 58	325.35	-7.47	0.082	G	13.98 ± 0.02	...	6	...	21(0)
K332	...	16 16 55.5	-61 02 26	325.36	-7.47	0.082	C	15.88 ± 0.04	...	3	...	21(0)
K333	R	16 16 55.7	-60 57 41	325.41	-7.41	0.076	G	14.46 ± 0.04	...	5	...	22(3)
K334	...	16 16 56.0	-60 43 44	325.58	-7.25	0.094	G	16.01 ± 0.06	...	3	...	24(0)
K335	...	16 16 57.0	-61 08 08	325.29	-7.54	0.076	G	14.49 ± 0.01	...	5	...	20(0)
K336	...	16 16 57.2	-60 56 33	325.43	-7.40	0.076	C	15.79 ± 0.07	...	2	...	22(0)
K337	WKK6380	16 16 57.7	-60 42 51	325.59	-7.24	0.094	G	13.38 ± 0.01	17.7	10	18800	24(0)
K338	...	16 16 58.3	-60 54 03	325.46	-7.37	0.084	C	15.07 ± 0.05	...	4	...	22(0)
K339	R	16 16 58.3	-60 41 29	325.61	-7.22	0.094	G	15.55 ± 0.05	...	2	...	24(0)
K340	...	16 16 59.1	-61 09 60	325.27	-7.56	0.076	C	14.95 ± 0.03	...	4	...	20(0)
K341	R	16 16 59.9	-61 10 08	325.27	-7.57	0.076	G	13.58 ± 0.01	...	7	29841	20(0)
K342	...	16 17 00.1	-61 15 17	325.21	-7.63	0.073	C	14.20 ± 0.01	...	6	...	39(0)
K343	WKK6383	16 17 00.4	-60 52 25	325.48	-7.36	0.084	G	10.80 ± 0.00	15.9	25	5431	22(2)
K344	...	16 17 01.2	-60 38 03	325.65	-7.19	0.092	C	15.92 ± 0.06	...	3	...	24(0)
K345	WKK6385	16 17 01.2	-60 41 36	325.61	-7.23	0.094	G	14.53 ± 0.03	17.2	4	7141	24(0)
K346	R	16 17 01.4	-61 09 18	325.29	-7.56	0.076	G	13.40 ± 0.01	...	7	...	20(0)
K347	R	16 17 02.1	-60 44 52	325.57	-7.27	0.093	G	15.05 ± 0.03	...	4	...	23(0) 24(16)
K348	R	16 17 02.6	-61 07 47	325.31	-7.54	0.076	G	14.49 ± 0.02	...	5	...	20(0)
K349	...	16 17 05.2	-60 52 08	325.49	-7.36	0.084	C	15.45 ± 0.03	...	3	...	22(0)
K350	R	16 17 06.1	-60 55 37	325.45	-7.40	0.084	G	15.69 ± 0.06	...	3	...	22(0)
K351	R	16 17 07.4	-60 52 29	325.49	-7.37	0.084	G	14.54 ± 0.02	...	5	...	22(0)

Table A.1 – Continued

K_s ID	Optical ID	RA (J2000) Dec		Gal l	Gal b	A_{K_s}	Class	K_s [mag]	B_J	D	Vel.	Field (Flag)
		[^{h} ^{m} ^{s}]	[$^\circ$ $'$ $''$]	[°]	[°]	[mag]		[mag]	[mag]	[$''$]	km s^{-1}	
(1)	(2)	(3a)	(3b)	(4a)	(4b)	(5)	(6)	(7) (8)	(9)	(10)	(11)	
K352	...	16 17 09.3	-61 07 01	325.32	-7.54	0.076	C	16.31 ± 0.07	...	3	...	20(0)
K353	...	16 17 11.7	-61 06 21	325.34	-7.54	0.076	G	15.55 ± 0.05	...	4	...	20(0)
K354	...	16 17 17.7	-60 43 58	325.61	-7.28	0.093	C	14.62 ± 0.03	...	6	...	24(0)
K355	...	16 17 18.6	-61 05 13	325.36	-7.53	0.082	C	15.18 ± 0.03	...	5	...	20(0)
K356	...	16 17 18.9	-60 37 54	325.68	-7.21	0.092	G	14.84 ± 0.02	...	4	...	24(0) 45(0) 46(0)
K357	R	16 17 20.0	-60 53 11	325.50	-7.39	0.084	G	13.57 ± 0.01	...	7	...	43(3)
K358	R	16 17 20.4	-60 51 53	325.52	-7.38	0.084	G	13.39 ± 0.02	...	9	3960	22(2) 43(2)
K359	WKK6402	16 17 22.1	-60 38 03	325.68	-7.22	0.092	G	10.58 ± 0.00	15.4	37	5826	24(2) 45(2) 46(18)
K360	WKK6406	16 17 25.0	-60 37 55	325.69	-7.22	0.092	G	14.45 ± 0.03	17.3	7	7349	24(0) 45(0) 46(16)
K361	R	16 17 25.6	-61 03 01	325.39	-7.52	0.082	G	16.31 ± 0.08	...	2	...	41(0)
K362	R	16 17 26.5	-61 16 29	325.24	-7.68	0.078	G	14.37 ± 0.02	...	5	18551	39(0)
K363	WKK6407	16 17 27.4	-61 02 59	325.40	-7.52	0.082	G	14.07 ± 0.03	18.1	7	3653	21(16) 41(0)
K364	R	16 17 29.6	-60 53 34	325.51	-7.41	0.084	G	13.78 ± 0.01	...	5	...	43(0)
K365	...	16 17 32.7	-60 53 43	325.52	-7.42	0.084	G	12.99 ± 0.01	...	8	...	42(2) 43(0)
K366	R	16 17 34.6	-60 42 02	325.66	-7.28	0.097	G	15.53 ± 0.05	...	4	...	44(0)
K367	...	16 17 37.1	-60 54 38	325.51	-7.43	0.084	C	14.35 ± 0.02	...	5	...	43(0)
K368	WKK6416	16 17 38.3	-61 08 36	325.35	-7.60	0.076	G	14.57 ± 0.04	18.0	5	...	40(0) 41(16)
K369	...	16 17 40.1	-60 41 56	325.66	-7.29	0.097	C	15.99 ± 0.05	...	3	...	44(0)
K370	WKK6419	16 17 43.7	-60 38 52	325.71	-7.26	0.097	G	14.08 ± 0.03	17.7	6	4453	45(0)
K371	...	16 17 45.5	-60 39 36	325.70	-7.27	0.097	G	15.88 ± 0.06	...	3	...	45(0)
K372	...	16 17 45.8	-60 56 06	325.51	-7.46	0.088	G	15.33 ± 0.04	...	3	...	42(0)
K373	...	16 17 48.4	-61 09 49	325.35	-7.63	0.076	C	15.29 ± 0.05	...	3	...	40(0)
K374	R	16 17 50.0	-61 10 04	325.35	-7.63	0.076	G	15.43 ± 0.05	...	2	...	40(0)
K375	...	16 17 53.6	-61 02 33	325.44	-7.55	0.085	C	15.51 ± 0.03	...	4	...	41(0)
K376	WKK6429	16 17 54.9	-61 12 59	325.32	-7.68	0.076	G	11.50 ± 0.01	16.4	16	4035	40(3)
K377	R	16 17 56.2	-60 55 38	325.53	-7.47	0.088	G	13.91 ± 0.02	...	7	...	42(0)
K378	R	16 17 56.2	-61 05 57	325.40	-7.59	0.085	G	14.09 ± 0.02	...	8	...	41(0)
K379	WKK6430	16 17 56.8	-61 08 00	325.38	-7.62	0.085	G	13.38 ± 0.01	17.3	8	...	40(0) 41(0)
K380	WKK6431	16 17 57.3	-60 55 23	325.53	-7.47	0.088	G	10.90 ± 0.00	15.7	20	3333	42(2)
K381	R	16 17 59.0	-60 55 05	325.54	-7.47	0.088	G	14.46 ± 0.03	...	4	...	42(0)
K382	R	16 17 59.0	-61 07 15	325.39	-7.61	0.085	G	15.02 ± 0.04	...	3	...	41(0)
K383	R	16 18 00.6	-60 41 19	325.70	-7.31	0.097	G	15.06 ± 0.04	...	4	...	44(0)

Table A.1 – Continued

K_s ID	Optical ID	RA (J2000) Dec		Gal l	Gal b	A_{K_s}	Class	K_s [mag]	B_J	D	Vel.	Field (Flag)
		[^{h} ^{m} ^{s}]	[$^\circ$ $'$ $''$]	[$^\circ$]	[$^\circ$]	[mag]		[mag]	[mag]	[$''$]	km s^{-1}	
(1)	(2)	(3a)	(3b)	(4a)	(4b)	(5)	(6)	(7) (8)	(9)	(10)	(11)	
K384	...	16 18 00.8	-60 37 30	325.75	-7.26	0.097	G	15.48 ± 0.05	...	3	...	45(0)
K385	...	16 18 01.3	-60 40 36	325.71	-7.30	0.097	C	15.33 ± 0.03	...	3	...	45(0)
K386	WKK6439	16 18 04.2	-60 41 42	325.70	-7.32	0.097	G	10.27 ± 0.00	15.3	31	3942	44(2)
K387	WKK6443	16 18 07.4	-60 56 48	325.53	-7.50	0.088	G	15.49 ± 0.05	18.1	2	...	42(0)
K388	...	16 18 08.1	-60 47 48	325.64	-7.40	0.093	C	16.09 ± 0.07	...	2	...	44(0)
K389	...	16 18 10.0	-61 02 28	325.47	-7.57	0.089	C	15.71 ± 0.06	...	3	...	41(0)
K390	...	16 18 11.1	-61 07 60	325.40	-7.64	0.085	C	16.07 ± 0.07	...	3	...	41(0)

Bibliography

Aaronson, M., Huchra, J., Mould, J. et al. 1982, ApJ 258, 64

Abell, G. O., Corwin, H.G. & Olowin, R.P. 1989, ApJS 70, 1

Andreon, S. & Pelló, R. 2000, A&A 353, 479

Andreon, S., Cuillandre, J.-C. & Pelló, R. 2000, in Constructing the Universe with Clusters of Galaxies, IAP 2000 meeting, eds. F. Durret and D. Gerbal

Andreon, S., Pelló, R., Davoust, E., Dominguez, R. & Poulain, P. 2000, A&AS 141, 113

Andreon, S. 2001, ApJ 547, 623

Andreon, S., Punzi, G. & Grado, A. 2005, MNRAS 360, 727

Arce, H.G. & Goodman, A.A. 1999, ApJ 512, L135

Barger, A.J., Aragon-Salamanca, A., Ellis, R.S., Couch, W.J., Smail, I. & Sharples, R.M. 1996, MNRAS 279, 1

Bertin, E. & Arnouts, S. 1996, A&AS 117, 393

Bertschinger, E. & Dekel, A. 1989, ApJ 336, 5

Binggeli, B., Sandage, A. & Tammann, G.A. 1988, ARA&A 26, 509

Böhringer, H., Neumann, D.M., Schindler, S. & Kraan-Korteweg, R.C. 1996, ApJ 467, 168

Burstein, D. & Heiles, C. 1982, AJ 87, 1165

Burstein, D. 2003, AJ 126, 1849

Burstein, D. 2005, in Nearby Large-Scale Structures and the Zone of Avoidance, ASP Conference Series, Vol. 329, eds. A.P. Fairall and P.A. Woudt, 111

Buta, R.J. & McCall, M. L. 1999, ApJS 124, 33

Cameron, L.M. 1990, A&A 233, 16

Cardelli, J.A., Clayton, G.C. & Mathis, J.S. 1989, ApJ 345, 245

Charlier, C.V.L. 1922, Arkiv för Mat. Astron. Fys. 16, 1

Chiboucas, K. & Mateo, M. 2006, AJ 132, 347

Choloniewski, J. & Valentijn, E.A. 2003, Acta Astronomica 53, 265

Cole, S., Norberg, P., Baugh, C.M. et al. 2001, MNRAS 326, 255

De Propris, R., Eisenhardt, P.R., Stanford, S.A. & Dickinsoon, M. 1998, ApJ 503, L45

De Propris, R. et al. 2002, MNRAS 329, 87

Dekel, A. 1994, ARA&A, 32, 371

Dicke, R.H., Peebles, P.J.E., Roll, P.G. & Wilkinson, D.T. 1965, ApJ 142, 414

Doi, M., Fukugita, M., Okamura, S. & Tarusawa, K. 1995, ApJS 97, 77

Dressler, A. & Faber, S. M. 1990, ApJ 354, 13

Dreyer, J.L.E. 1888, Mem. R.A.S. XLIX, Part 1, "A New General Catalogue of Nebulae and Clusters of Stars, being the catalogue of the late Sir John F.W. Herschel, revised, corrected and enlarged"

Dreyer, J.L.E. 1895, Mem. R.A.S. LI, "Index of Catalogue of Nebulae found in the Years 1888 to 1894, with Notes and Corrections"

Dutra, C.M., Ahumada, A.V., Clariá, J.J., Bica, E., Barbuy, B. 2003, A&A 408, 287

Ebeling, H., Mullis, C. R. & Tully, R. B. 2002, ApJ 580, 774

Epchtein, N. 1997, in 2nd Euroconference, The Impact of Large Scale Near Infrared Surveys, eds. F. Garzón, N. Epchtein, A. Omont, B. Burton and P. Persi, Dordrecht: Kluwer, 15

Epchtein, N., Batz, B. de, Capoani, L. et al. 1997, Messenger, 87, 27

Faber, S. M. & Burstein, D. 1988, in The Vatican Study Week on Large Scale Motions in the Universe, eds. G.V. Coyne and V.C. Rubin, Princeton: Princeton University Press, 115

Fairall, A.P. 1998, Large Scale Structures in the Universe, New York : Wiley

Ferguson, H.C. & Sandage, A. 1988, AJ 96, 1520

Gardner, J.P., Sharples, R.M., Frenk, C.S. & Carrasco, B.E. 1997, ApJ 480, L99

Garilli, B., Maccagni, D. & Andreon, S. 1999, A&A 342, 408

Gehrels, N. 1986, ApJ 303, 336

Geller M.J. & Huchra, J.P. 1989, Science, New Series, 246, 4932, 897

Glass, I.S. 1999, Handbook of Infrared Astronomy, Cambridge: Cambridge University Press

Glazebrook, K., Peacock, J.A., Miller, L. & Collins, C.A. 1995, MNRAS 275, 169

Henning, P.A., Staveley-Smith, L., Ekers, R.D. et al. 2000, AJ 119, 2686

Herschel, J. 1864, Philosophical Transactions

Holmberg, E. 1958, Medd. Lund Astron. Obs., Ser. 2, 136

Holmberg, E. 1969, Ark. Astron. 5, 305

Huang, J.-S., Cowie, L.L., Gardner, J.P., Hu, E.M., Songaila, A. & Wainscoat, R.J. 1997, ApJ 476, 12

Huang, J.-S., Glazebrook, K., Cowie, L.L. & Tinney, C. 2003, ApJ 584, 203

Hubble, E. 1929, Proceedings of the National Academy of Sciences of the United States of America, Volume 15, Issue 3, 168

Hubble, E., 1936a, ApJ 84, 158

Hubble, E. 1936b, ApJ 84, 270

Hubble, E. 1936c, The Realm of the Nebulae, New Haven, Conn: Yale University Press, 149

Hudson, M.J. & Lynden-Bell, D. 1991, MNRAS 252, 219

Jarrett, T. H. 2004, Publications of the Astronomical Society of Australia, Vol. 21, Issue 4, 396

Jarrett, T. H., Chester, T., Cutri, R., et al. 2000a, AJ 119, 2498

Jarrett, T. H., Chester, T., Cutri, R., et al. 2000b, AJ 120, 298

Jarrett, T. H., Chester, T., Cutri, R., et al. 2003, AJ 125, 525

Jerjen, H. & Tammann, G.A. 1997, A&A 321, 713

Joint *IRAS* Science Working Group 1988, IRAS Point Source Catalogue, Version 2, Washington: US Govt. Printing Office

Jones, D.H., Peterson, B.A., Colless, M. & Saunders, W. 2006, MNRAS 369, 25

Kauffmann, G., Colberg, J. M., Diaferio, A., White, S. D. M. 1999, MNRAS 303, 188

King, C.R. 1962, AJ 67, 471

Kochanek, C.S., Pahre, M.A., Falco, E.E., et al. 2001, ApJ 560, 566

Kogut, A., Lineweaver, C., Smoot, G.F., et al. 1993, ApJ 419, 1

Kolatt, T., Dekel, A., Lahav, O. 1995, MNRAS 275, 797

Kraan-Korteweg, R.C. 1981, A&A 104, 280

Kraan-Korteweg, R.C. 2000, A&AS 141, 123

Kraan-Korteweg R.C. & Tammann, G.A. 1979, Astron. Nachr. 300, 181

Kraan-Korteweg, R.C. & Huchtmeier, W. 1992, A&A 266, 150

Kraan-Korteweg, R.C. & Woudt, P.A. 1994, in Unveiling Large-Scale Structures behind the Milky Way, ASP Conference Series, Vol. 67, eds. C. Balkowski and R.C. Kraan-Korteweg, 89

Kraan-Korteweg, R.C., Cayatte, V., Balkowski, C., Fairall, A.P. & Henning, P.A. 1994, in Unveiling Large-Scale Structures behind the Milky Way, ASP Conference Series, Vol. 67, eds. Balkowski and Kraan-Korteweg, 99

Kraan-Korteweg, R.C., Woudt, P.A., Cayatte, V., et al. 1996, Nature 379, 519

Kraan-Korteweg, R.C. & Lahav, O. 2000, A&AR 10, 211

Kraan-Korteweg, R.C. & Jarrett, T.H. 2005, in Nearby Large-Scale Structures and the Zone of Avoidance, ASP Conference Series, Vol. 329, eds. A.P. Fairall and P.A. Woudt, 119

Kraan-Korteweg, R.C., Staveley-Smith, L., Donley, J., Koribalski, B. & Henning, P. A 2005, in Maps of the Cosmos, Proceedings of IAU Symposium No. 216, eds. M. Colless, L. Staveley-Smith and R. Stathakis, San Francisco: Astronomical Society of the Pacific, 203

Kron, R. G. 1980, ApJS 43, 305

Lahav, O., Yamada, T., Scharf, C.A., Kraan-Korteweg, R.C. 1993, MNRAS 262, 711

Lauberts, A. 1982, The ESO/Uppsala Survey of the ESO (B) Atlas, Garching: ESO

Lobo, C., Biviano, A., Durret, F. et al. 1997, A&A 317, 385

Loveday, J. 2000, MNRAS 312, 557

Lu, N. & Freudling, W. 1995, ApJ 449, 527

Mamon, G.A. 1998, in XIVth IAP Astrophysics Meeting, Wide Field Surveys in Cosmology, eds. S. Colombi, Y. Mellier and B. Raban, Gif-sur-Yvette: Editions Frontiéres, 323

Markus, K. 2006, MSc Thesis, University of Cape Town

Mathewson, D. S., Ford, V. L. & Buchhorn, M. 1992, ApJ, 389, L5

Mazure, A., Casoli, F., Durret, F. & Gerbal, D. (Eds.) 1998, Untangling Coma Berenices: A New Vision of an Old Cluster, Proceedings, Word Scientific Publishing Co Pty Ltd.

McCall, M. L. 2004, AJ 128, 2144

Mobasher, B., Sharples, R.M. & Ellis, R.S. 1993, MNRAS 263, 560

Mobasher, B. & Trentham, N. 1998, MNRAS 293, 315

Mobasher, B., Colless, M., Carter, D. et al. 2003, ApJ 587, 605

Nagashima, C., et al. 1999, in Star Formation, ed. T. Nakamoto, Nobeyama Radio Observatory, 397

Nagayama, T., Nagashima, C., Nakajima, Y., et al. 2003, SPIE, 4841, 459

Nagayama, T., Woudt, P.A., Nagashima, C., et al. 2004, MNRAS 354, 980

Nagayama, T., Woudt, P.A., Wakamatsu, K., et al. 2006, MNRAS 368, 534

Nilson, P. 1973, Uppsala General Catalog of Galaxies, Uppsala: University of Uppsala

Oegerle, W.R., Hoessel, J.G. & Ernst, R.M. 1986, AJ 91, 697

Paul, E.R. 1986, Journ. History of Astronomy 17, 50, 155

Peacock, J.A. 1999, Cosmological Physics, Cambridge: Cambridge University Press

Penzias, A.A. & Wilson, R.W. 1965, ApJ 142, 419

Persson, S.E., Murphy, D.C., Krzeminski, W., Roth, M. & Rieke, M.J. 1998, AJ 116, 2475

Proctor, R. 1878, The Universe of Stars, London: Longmans, Green and Co., 41

Radburn-Smith, D. J., Lucey, J. R., Woudt, P. A., Kraan-Korteweg, R. C. & Watson, F. G. 2006, MNRAS 369, 1131

Sandage, A., Binggeli, B. & Tammann, G.A. 1985, AJ 90, 1759

Sarazin, C.L. 1986, Rev. Mod. Phys. 58, 1

Saunders, W., Sutherland W.J., Maddox, S.J. et al. 2000, MNRAS 317, 55

Saunders, W., D'Mellow, K., Tully, B. et al. 2000, in Mapping the Hidden Universe: The Universe Behind the Milky Way - The Universe in HI, ASP Conference Series, Vol. 218, eds. R.C. Kraan-Korteweg, P.A. Henning and H. Andernach,

Scaramella, R., Baiesi-Pillastrini, G., Chincarini, G., Vettolani, G., & Zamorani, G. 1989, Nature 338, 562

Secker, J. & Harris, W.E. 1996, ApJ 469, 623

Shane, C.D. & Wirtanen C.A. 1967, Publ. Lick Obs. XXII, Pt. I

Schechter, P. 1976, ApJ 203, 297

Schlegel, D.J., Finkbeiner, D.P. & Davis, M. 1998, ApJ 500, 525

Schröder A., Kraan-Korteweg, R.C., Mamon, G.A. 2000, in Mapping the Hidden Universe: The Universe Behind the Milky Way - The Universe in HI, ASP Conference Series, Vol. 218, eds. R.C. Kraan-Korteweg, P.A. Henning and H. Andernach, 119

Schröder A., Kraan-Korteweg, R.C., Mamon, G.A., Woudt, P.A. 2005, in Nearby Large-Scale Structures and the Zone of Avoidance, ASP Conference Series, Vol. 329, eds. A.P. Fairall and P.A. Woudt, 167

Schröder A., Mamon, G., Kraan-Korteweg, R.C., Woudt, P.A. 2006, in press

Shapley H. 1961, in Galaxies, Cambridge: Harvard University Press, 159

Skrutskie, M.F., Cutri, R.M., Stiening, R. et al. 2006, The Two Micron All Sky Survey (2MASS), AJ 131, 1163

Smoot, G.F., Bennett, C. L., Kogut, A. et al. 1992, ApJ 396, L1L5

Somerville, R. & Primack, 1999

Stetson, P. B. 1987, Publications of the Astronomical Society of the Pacific 99, 191

Szokoly, G.P., Subbarao, M.U., Connolly, A.J & Mobasher, B. 1998, ApJ 492, 452

Tammann, G.A., Sandage, A. & Yahil, A. 1980, Phys. Ser. 21, 630

Tashiro, M., Kaneda, H., Makishima, K., Iyomoto, N. et al. 1998, ApJ 499, 713

Thompson, L.A. & Gregory, S.A. 1980, ApJ 242, 1

Trentham, N. & Mobasher, B. 1998, MNRAS 299, 488

Van der Hulst, 1957, "Light scattering by small particles", New York: Wiley

Valotto, C.A., Nicotra, M.A., Muriel, H. & Lambas, D.G. 1997, ApJ 479, 90

Vorontsov-Velyaminov, B. & Archipova, V. 1963-1974, Morphological Catalog of Galaxies, Parts 2 - 5, Moscow: Moscow University

Woudt, P.A. 1998, PhD Thesis, University of Cape Town

Woudt, P.A., Kraan-Korteweg, R.C. & Fairall, A.P. 1999, A&A 352, 39

Woudt, P.A. & Kraan-Korteweg, R.C. 2000, Mapping the Hidden Universe: The Universe Behind the Milky Way - The Universe in HI, ASP Conference Series, Vol. 218, eds. R.C. Kraan-Korteweg, P.A. Henning and H. Andernach, 193

Woudt, P.A., Kraan-Korteweg, R.C. & Fairall, A.P. 2000, Cosmic Flows 1999: Towards an Understanding of Large-Scale Structure, ASP Conference Series, Vol. 201, eds. S. Courteau, M.A. Strauss and J.A. Willick

Woudt, P.A. & Kraan-Korteweg, R.C. 2001, A catalogue of galaxies behind the Southern Milky Way II The Crux and Great Attractor Regions ($l \sim 289°$ to 338°), A&A 380, 441-459

Woudt, P. A., Kraan-Korteweg, R. C., Cayatte, V., Balkowski, C., Felenbok, P. 2004, A&A 415, 9

Woudt, P.A., Fairall, A.P., Kraan-Korteweg, R.C., et al. 2005, in Nearby Large-Scale Structures and the Zone of Avoidance, ASP Conference Series, Vol. 329, eds. A.P. Fairall and P.A. Woudt, 147

Zwicky, F. 1942, Phys. Rev. 61, 489

Zwicky, F. 1957, Morphological Astronomy, Berlin: Springer-Verlag, 220

Zwicky, F. 1964, ApJ 140, 1624